RHEOLOGICAL CHARACTERIZATION DURING METALLURGICAL SOLID-LIQUID PHASE CHANGES IN RESISTANCE SPOT WELDING AND BINDER JET PRINTING

by

Ruiji Sun

A Dissertation

Submitted to the Faculty of Purdue University

In Partial Fulfillment of the Requirements for the degree of

Doctor of Philosophy

Department of Engineering Technology

West Lafayette, Indiana

August 2021

THE PURDUE UNIVERSITY GRADUATE SCHOOL
STATEMENT OF COMMITTEE APPROVAL

Dr. Haiyan Zhang, Chair
School of Engineering Technology

Dr. Dongming Gan
School of Engineering Technology

Dr. Huachao Mao
School of Engineering Technology

Dr. Milan Rakita
School of Engineering Technology

Dr. Wangling Yu
Department of Engineering Technologies, Ivy Tech

Approved by:
Dr. Kathryne A. Newton

Dedicated to my parents and my husband.

ACKNOWLEDGMENTS

My advisor Dr. Haiyan H. Zhang has been most supportive to me and merit all appreciation from me. He has been a mentor, a life coach, and a friend through my journey as a student and a young adult trying to find her place in life. He has been most supportive through my research and career, motivating me when I faced obstacles and applaud me when I made progress. It has been a great honor to work with him and learn from his wisdom and guidance.

I am thankful for the guidance I received from Dr. Qingyou Han, Dr. Dongming Gan, Dr. Huachao Mao, Dr. Milan Rakita, Dr. Xiaoming Wang, and Dr. Wangling Yu. They have been offering me immense support and invaluable advisory, and I am forever grateful for their help and guidance.

Stellantis FCA team and GE Additive team have provided the research with immense help in sponsoring and assisting the project, both in technology and expertise. I am honored to collaborate with many great engineers from Stellantis FCA and GE additive teams.

I would like to thank Professor Nancy Denton, my coach, friend, and most importantly, my mentor to the art of education. She transformed me from a shy and self-conscious new graduate student into a confident and eloquent instructor through her patience, support, and experience. She is the inspiration for me to become a teacher by bestowing me the courage and confidence to explore the world of education.

My department administration team, my colleagues, and the lab engineers have given me so much help and support, including but not limited to Ms. Niedra McLeland, Ms. Aslee Messersmith, Ms. Debbie Hulsey, Ms. Felicia Anderson, Dr. Kathryn Newton, Dr. Kenneth Burbank, Dr. Yanfei Liu, Mr. Heming Liu, Mr. Michael Puetz, and Mr. Clayton Kibbey. Their support and guidance aided me in achieving my academic goals and finishing my Ph.D. study.

TABLE OF CONTENTS

LIST OF TABLES

LIST OF FIGURES

ABBREVIATIONS

RSW:	Resistance spot welding
BJP:	Binder jet printing
SD:	Standard deviation
DSR:	Dimensional shrinkage rate
CAD:	Computer-aided design
AC:	Alternating current
DC:	Direct current
FEA:	Finite element analysis
FEM:	Finite element method
CCT:	Continuous cooling transformation
R&D:	Research and development
AM:	Additive manufacturing

NOMENCLATURE

σ stress

γ strain

G the rigidity modulus

$\dot{\gamma}$ shear rate or velocity gradient

U shear velocity

d current thickness

η coefficient of viscosity

T absolute temperature

A constant of the liquid

B constant of the liquid

η_0 viscosity at the low shear rate

η_∞ the viscosity at the high shear rate

K parameter for dimensionless time

m constant for Cross model

n the power-law index

K_2 consistency

σ_y yield stress

η_p plastic viscosity.

N pairs of dendrites forming resistors and

R_k resistance of the kth pair of dendrite

Q_k amount of heat generated by the resistor

R_a surface roughness

D_l liquid diffusivity

D_s solid diffusivity

ΔL expanded length

L_f final lengths

L_0 original lengths

ΔT temperature change

α thermal expansion coefficient

T_i the temperature of the ith phase

α_i thermal diffusivity of the ith phase

k_i thermal conductivity of the ith phase

l liquid phase

s solid phase

x the distance from the surface of the workpiece

t irradiation time

T_m melting point

r density

L latent heat of fusion

T_0 initial temperature

$X(t)$ the distance from the substrate surface to the solid-liquid interface

η absorbed heat flux

θ_s relative solidus temperature

θ_l relative liquidus temperature

τ dimensionless time

ξ relative position

ξ^* relative interface position

Ste Stefan number

δ relative liquid percentage

θ_f dimensionless freezing point

Le Lewis number

k_0 segregation coefficient

m_l liquidus slope

C_0 nominal composition

T_0 hold temperature

T_∞ initial temperature

t_f solidification time

t_{weld} welding time

c_p specific heat

L_f melting heat

T_∞ superheat temperature

T_f solidification temperature of the pure solvent

t_{RSW} total RSW time

ABSTRACT

The dissertation offers a Multiphysics perspective in analyzing emerging metallurgical techniques. Heat transfer, structural deformation, and fluid flow associate with one another in phase-changing materials processing methods. To comprehensively analyze these aspects for an optimized final product, the authors have proposed a numerical mathematical model describing the thermal and geometric progression of the binary alloy casting process. The model is further executed in COMSOL Multiphysics, adapted in two metal manufacturing applications, resistance spot welding (RSW) and binder jet printing (BJP).

Resistance spot welding is a well-adapted metal sheeting joining technique with comparably limited modeling and simulating research. The heat transfer module and geometric deformation module are applied to the simulation of RSW to discuss the thermal gradient development of the welding zone. The model was further calculated and verified through a case study with Python.

BJP is a rapidly developing additive manufacturing method. The novel 3D printing technique brings challenges in post-processing geometric control and material selection limitations. Multiphysics simulation serves as an excellent tool in process parameters analysis and quality control. This dissertation focuses on the sintering process of BJP of binary alloy powders. Melting and solidification mathematical models were implemented in COMSOL, where the sintering shrinkage rate could be calculated. The shrinkage rate was further verified through experimental analysis of binder jet printed samples.

Microstructural analysis on sintered binder jet printed parts was performed to assess the validity of BJP to substitute the die casting method for manufacturing of valvebody. Sintering shrinkage and metallurgical analysis have been performed on the green and sintered BJP samples. After sintering, the final part achieved 98% density, and the integrity of the designed channels was preserved. The shrinkage analysis has indicated the effect of printing orientation and sintering orientation on the geometry and metallurgy of the final products. Microstructure analysis on the cross-sections of the sintered products also indicates the various defects induced from biner jet 3D printing.

The research aims to provide a systematic rheology analysis of the phase transformation process of binary alloys. The dissertation has connected the physical, mathematical modeling with

simulative modeling through the rheological evaluation of phase-changing manufacturing techniques. The connections were conclusively verified through empirical studies, including case assessment and experimentation. The research aims to offer universally applicable models that can be applied to phase-changing metal processing techniques.

INTRODUCTION

The Journal of COMSOL Inc provided permission for me to publish this article titled COMSOL Implementation of Binder Jet Printing Densification Model in Automatic Valve System in this dissertation. Permission letters are attached in Appendix I. The following statement is indorsed by all authors: research structure and idea: Sun, R.; experiment and model execution: Sun, R.and Liu, H.; examination and conclusion of data: Sun, R, and Zhang, H.; paper outline formulation: Sun, R.; The dissertation manuscript has received approval from all mentioned authors.

The Journal of Journal of Multidisciplinary Engineering Science and Technology (JMEST) provided permission for me to publish this article titled Mathematical Modeling of Resistance Spot Welding in this dissertation. Permission letters are attached in Appendix I. The following statement is indorsed by all authors: research structure and idea: Zhang, H. and Das, M.; experiment and model execution: Sun, R., and Han, Q.; examination and conclusion of data: Sun, R, and Zhang, H.; paper outline formulation: Sun, R. and Zhang, H.; The dissertation manuscript has received approval from all mentioned authors.

The study of phase transformation processes has always been essential to metallurgical engineering, beneficial to both theoretical and application progresses. With the fast-paced progress of automobile industries, both traditional and newly emerged technologies require more detailed physical and mathematical metallurgical models to better monitor production progress. As most metal defects occur during solid-liquid phase changes, casting industries rely heavily on the accuracy of phase characterizations during the melting and solidification processes. Rheology is an approach to study how the materials flow and deform. (Barnes, 1989) There are three different states in metal materials: solid, liquid, and semi-solid state. Each state has its own unique rheological properties under external stress, which leads to a rheology study on solid-state forming, liquid metal casting, and rheocasting. In the solid-liquid phase transition stage during casting and welding, heat transfer and fluid flow analysis are complex yet crucial to the success of products. Thus, rheological analysis needs to be performed to fully comprehend the interaction among solid, liquid, and mushy phases.

An Overview of Rheology

Rheology is an approach to study how the materials flow and deform. (Barnes et al., 1989) Before rheology comes of age, Hooke's law of solid and Newton's law of liquid were the two main governing principles that support the study of elasticity and viscosity. However, since World War

II, a vast amount of interest has been placed on the study of the rheological properties of different materials. As a result, rheology has grown to be an independent discipline that analyzes the mechanical behaviors of materials.

The constitutive equation for Hooke's law of solid is $\sigma = G\gamma$, σ being the stress, γ the strain and G is the rigidity modulus. It describes the elastic deformation of solid materials under stress. When stress is applied, the elastic strain is instantaneous. When the stress is removed, the material will return to its original length instantaneously, too. For Newton's law of liquid, the constitutive equation is $\sigma = \eta\dot{\gamma}$, σ being the stress, $\dot{\gamma} = U/d$ being the shear rate or velocity gradient, and η is the coefficient of viscosity. The viscosity of the fluid is derived from the equation of Newton's law of liquid.

However, as rheology progresses, it has been found out that elasticity and viscosity co-exist in all materials, and solid or liquid are just relative terms to describe the ratio of elasticity and viscosity for the material. (Fischer, 2019) Solid materials sometimes exhibit liquid-like behaviors, and liquid materials sometimes exhibit solid-like behaviors. Thus, the term 'viscoelastic' describes the in-between state of Hookean solids and Newtonian liquids. As said, for Newtonian liquid, η is a constant coefficient for a specific type of material. However, for non-Newtonian liquid, η is not a constant coefficient. The viscosity of the liquid is subjected to the effect of different variables such as shear rate, temperature, pressure, and time of shearing. (Hildebrand & Lamoreaux, 1976)

Temperature variance causes the change in viscosity. For Newtonian liquids, the viscosity decreases as temperature increases based on the Arrhenius relationship: $\eta = Ae^{-B/T}$, where T is the absolute temperature, A and B are constants of the liquid. (Barnes et al., 1989) Viscosity increases exponentially with the increase in isotropic pressure. In high-density, high-temperature situations, pressure plays an essential part in determining the viscosity of the liquid. (Fischer, 2019)

There is a series of behaviors corresponding to Newtonian liquids in the context of shear viscosity. (Coussot et al., 2017) First, Newtonian liquids only generate shear stress in simple shear flow, while all normal stresses are of the same value. Second, viscosity η is not a function of the shear rate $\dot{\gamma}$, which means that η is a coefficient for Newtonian liquids. Third, viscosity η does not change with time. However long the shear time is, the viscosity of Newtonian liquids stays the same. Fourth, η is a simple combination of different types of deformation, which means that the combined effect of deformations will have the same effect on viscosity as if the deformations are

added to the materials individually. For Non-Newtonian liquids, their behaviors for shear viscosity will negate at least one of the four behaviors above.

For most non-Newtonian liquids, as the shear rate increases, the viscosity will decrease. Such behavior is named shear thinning, also as temporary viscosity loss and pseudoelasticity. For the opposite behavior, when viscosity increases with the increase of shear rate, it is called shear thickening, also dilatancy.

Numerous models have been proposed to model the viscosity-shear rate flow curves. (Barnes et al., 1989) Cross proposed the following equation:

$$\frac{\eta - \eta_\infty}{\eta_0 - \eta_\infty} = \frac{1}{1 + (K\dot{\gamma})^m} \tag{1}$$

or

$$\frac{\eta_0 - \eta}{\eta - \eta_\infty} = (K\dot{\gamma})^m \tag{2}$$

where η_0 is the viscosity at the low shear rate, and η_∞ is the viscosity at the high shear rate. K is a parameter for dimensionless time, and m a constant.

Carreau proposed a similar model as following:

$$\frac{\eta - \eta_\infty}{\eta_0 - \eta_\infty} = \frac{1}{(1 + (K_1\dot{\gamma})^2)^{m_1/2}} \tag{3}$$

For the conditions where $\eta > \eta_0$ and $\eta < \eta_\infty$, it can be derived that:

$$\eta = K_2\dot{\gamma}^{n-1} \tag{4}$$

which is the Power-law Model, n being the power-law index and K_2 being the consistency.

For the conditions where $\eta < \eta_0$,

$$\eta = \eta_\infty + \frac{\eta_0}{(K\dot{\gamma})^m} \tag{5}$$

which can be derived as

$$\eta = \eta_\infty + K_2\dot{\gamma}^{n-1} \tag{6}$$

It is the Sisko Model. If n is set as 0, the model will be

$$\eta = \eta_\infty + \frac{K_2}{\dot{\gamma}} \tag{7}$$

After the redefinition of the parameters, the above equation will be

$$\sigma = \sigma_y + \eta_p \cdot \dot{\gamma} \tag{8}$$

It is the Bingham Model, which describes the behaviors of the Bingham plastic. σ_y is the yield stress and η_p is the plastic viscosity.

Bingham plastic has one of the unique behaviors among non-Newtonian liquids. While flowing, the liquid behaves like a Newtonian liquid, with shear stress change proportional to the shear rate change. However, Bingham plastic requires minimum stress to be applied before the actual flowing of the liquid. The shear stress needs to reach the yield stress level before the shear strain happens. For non-Newtonian liquids, the parameters for shear rate-viscosity equations change under different circumstances. For example, different shear rate ranges will lead to different yield stress for Bingham plastic. If the same Bingham plastic is under different shear rates, although the shear rate-shear stress curves all follow the basic Bingham plastic property, the actual yield stress values will change as the shear rate increases by a decade. For different kinds of non-Newtonian liquids, although they all follow the power-law equation, specific parameters for the power-law equation need to be set for a certain level of the shear rate range. However, as the shear rate increases to a higher level, the viscosity will eventually approach a constant value.

For shear-thickening liquids, which are rarer cases than shear-thinning, the viscosity will increase as the shear rate increases. However, most shear-thickening cases are associated with the shear-thinning process first, which means in most cases, as the shear rate increases, the viscosity will drop before actually increase. For the shear-thickening region, the curve-fitting on the power-law equation will have $n > 1$. Time usually will also affect non-Newtonian liquids. Shear stress and viscosity will change over time of shearing, and these changes can be reversible or irreversible. In the case of thixotropy, the viscosity will decrease over time when shear stress is applied to the liquid. After the stress is removed, the structure will gradually recover, and so will the viscosity. Oppositely, negative thixotropy or anti-thixotropy happens when viscosity decreases as shear stress is being applied. It is worth noting that thixotropy usually associates with shear-thinning liquids, while negative thixotropy usually associates with shear-thickening liquids. (Barnes et al., 1989)

For two-phase non-Newtonian liquids systems, the temperature is one of the parameters for viscosity. In the simplest cases, change in the two-phase system will have the superposed effect from each phase individually. However, in more complex cases, like dispersions, the temperature of the suspended phase can go beyond the melting point during the heating process, resulting in a marginal decrease of viscosity. For polymeric systems like lubricant oils, as the temperature rises,

the viscosity of the oil will decrease. However, the polymer coiled chains in the oil will open up in the meantime, leading to an overall increase in viscosity, remaining good lubrication in high-temperature conditions. (Coussot et al., 2017)

Viscometers are the means for measuring viscosity. For most industrial viscometers, calibration is an essential step for measuring Newtonian or Non-Newtonian liquids. For the calibration process, they are used to calibrate the viscometers. Most viscometers are calibrated with Newtonian liquids (usually oils) which have been calibrated with glass capillary viscometers. There are mainly three kinds of industrial viscometers. Firstly, the rotational devices, such as the Brookfield viscometer, measure the viscosity by applying the rotation and then measure the couple. The second kind is the flow-through constriction devices such as Ford cup arrangements. The third kind of device is designed using flow-around obstructions such as the Glen Cresto falling-ball instrument. (Barnes et al., 1989)

Rheology is a subject widely brought up and studied in the field of soft matter, such as gels, polymers, and some biological materials. However, in the 1970s, Spencer from MIT discovered that Sn-15%Pb alloys still maintain good fluidity at 40% solid phase fraction when stirred above the liquidus temperature. (Spencer et al., 1972) Since then, semi-solid metal alloys have gradually developed into an important branch of rheology study.

Resistance Spot Welding

Process Overview of Resistance Spot Welding

Resistance spot welding is a well-adapted manufacturing technique in the automotive industry. (Kimchi & Phillips, 2017) During Resistance spot welding, high currents pass through two pressed metal sheetings. The resistance at the interface leads to focused joule heating. A welding nugget is formed afterward, and two metal sheets are joined. (Zhou & Cai, 2013) RSW is a rapid processing method utilizing high pressure and focused current. As shown in Figure 1, the electrical resistance of the material to be welded leads to focused Joule heating at the interface, and eventually, a welding nugget is formed. The actual welding time is typical around 1/5 second when the welding piece thickness is around 1 mm. (Kimchi & Phillips, 2017) During the melting and solidification of the mild steel welding process, over 80% of the heat generated is taken away by water-cooled electrodes.

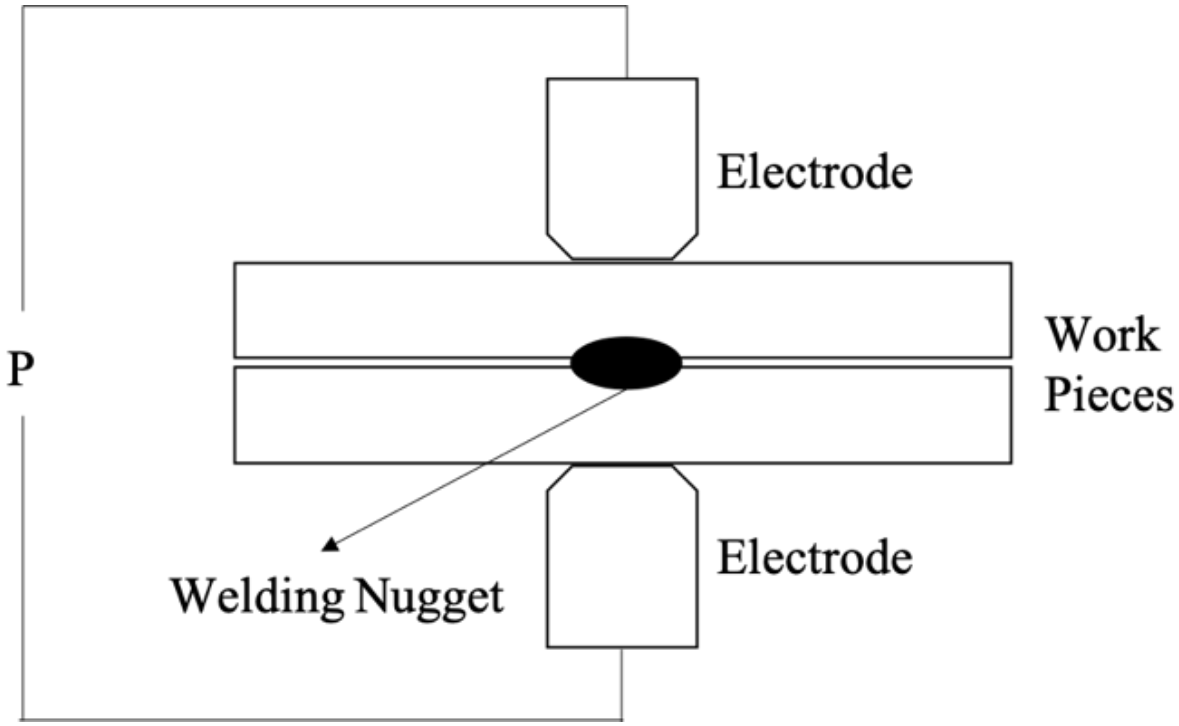

Figure 1 Resistance spot welding machine with the workpiece

Resistance spot welding is one of the oldest electrical welding techniques used for welding most known metals. (Zhou & Cai, 2014) The actual weld is made at the interface of the two workpieces. As shown in Figure 1, the regional electrical resistance of the metal sheets due to the surface roughness leads to concentrated heating at the interfaces being fastened. Resistance spot welder usually has two electrode tips of brass because of its low resistance. When current passes through the workpiece, it can generate a massive amount of heat in a short period and can heat the workpiece up to 1000℃. (Tan et al., 1976) A welding nugget is formed between the two workpieces, and the two metal pieces are welded during the process. Both AC and DC can be implemented on RSW. However, inherent losses can happen to 1 cycle sine wave AC because and result in lower efficiency than DC. Before the resistance spot welding process, the workpieces need to be filed to remove any coating or paint and make sure the welding surface is smooth.

There are typically three stages in the RSW process: (Kimchi & Phillips, 2017)

(1) Squeeze time:

Before applying the current, electrodes will press down both sides of the welding pieces to ensure proper alignment and contact. Squeezing of the electrodes on both sides of sheets is on in

all three steps. Applying the right amount of force from the electrodes is essential to maintain the pressure needed in nugget formation and maintain heat. Squeeze time is 99 cycles, i.e.,1.65 seconds (60 cycles = 1 sec)

(2) Weld time:

For thin sheets, a constant voltage is desirable. Weld time with the electric current ON is 12 – 15 cycles, i.e., 0.20 ~ 0.25 seconds.

For thick sheets, the pulse voltage is desirable. Weld time is eight cycles ON, ten cycles OFF, eight cycles ON. The total weld time is still 12 -15 cycles.

(3) Holding time:

After the welding nugget is formed and the current is off, electrodes will remain in place to hold the welding pieces for some time until the weld cools off to ensure complete solidification and maintain the proper shape of the nugget. Since electrodes are made of brass and have cooling water circulating inside, the heat dissipation is fast. Hold time is usually 2 ~ 5 cycles.

There are some factors that will influence the final welding product. (Barnes, 1989) Before the actual process, the welding electrode tips need to be appropriately aligned to ensure the current flow through the workpiece is in an hourglass shape. If the welding tips are not appropriately aligned, the current will be distorted, and the final weld piece may be bent or deformed. The weld tip force or squeeze pressure also needs to be correctly adjusted to maintain the proper amount of resistance between the workpieces and the electrode and workpiece. If the force is too low, the resistance will be too high. Overheating the workpiece surfaces can lead to excessive indentation, surface expulsion, brassing, and blow holes. If the force is too low, the resistance will decrease, causing the heat generated to be too low, and the final weld will be weak and substandard.

Weld tip size also needs to be considered before the actual process. Weld tips need to be coordinated with the size of the metal plates so that the central spot between the two electrode tips is on the contact surface of two workpieces. This ensures the center of the weld nugget locate at the contact surface, leading to a tight and sturdy structure.

Weld current and weld time are important factors affecting the final weld product. There are usually ten cycles of weld time. After the current flows, the first 4 to 5 cycles will heat the metal, and the tips will move closer. After the 6th cycle, the weld nugget will start forming, and in the subsequent five cycles, the nugget will begin to increase in size. The scale of the current needs to be properly adjusted based on the materials and size of the workpieces.

After the current is cut off, there will be a period of hold time where the electrode tips remain in contact with the welding area to absorb heat and hold the structure in place. There is cooling water pumping inside both tips to take out the heat from the welding area. The hold time is usually about 4-5 cycles. If the hold time is too short, the weld nugget may not have enough time to solidify and may spring apart as the electrodes are removed. If the hold time is too long, an excessive indentation may happen due to the weld nugget deformation. Cracking may also happen due to excessive cooling on the weld surface. (Miller Welds Handbook, 2012)

Modeling Review of Resistance Spot Welding

RSW is unique in that the welding happens in between and two metal sheets compared to other welding methods. The nugget development is not visible from human observation. Thus, numerous models have been developed in an attempt to control and optimize the welding process.

D.W. Dickinson proposed that there are six stages regarding dynamic resistance change during the RSW process. (D. Dickinson et al., 1980) The contacting surface and temperature change affect the resistance between the interface during the welding. The model was developed experimentally based on experimental data of RSW on steel sheets. The dynamic resistance change is divided into six stages during RSW. Firstly, the spacing between two work pieces and contamination on the work surfaces result in a vast resistance concentration. Therefore, when the current runs through the two metal plates, the surfaces will generate a vast amount of heat and eventually break down any contaminations between the two workpieces, reducing the resistance drastically. Second, as metal pieces keep heating up, the temperature begins to increase. This phenomenon leads to two opposite effects: Contacting surface area increases because metals are heating up and turning softer, lowering the resistance between two workpieces. However, higher temperature also leads to higher resistance. The two effects work together, causing the resistance in stage two to first decrease and then increase. In the next stage, while the metal pieces keep heating up, the two effects on resistance mentioned in stage two still co-exist. As the resistance increase from the temperature rise is dominant in this stage, the overall resistance is increasing. The end of stage three is marked by the forming of the molten nugget. In stage four, the metal starts to melt from the center, forming the kernel. As the volume of the kernel becomes bigger, the work piece will begin to deform and collapse, which contributes to lowering the resistance. The resistance, as a result, will first reach a peak value before eventually begin to decrease. In stage

five, the melting area expands, and the kernel keeps growing bigger. The liquid in the center starts to expand perpendicular to the clamping force of two electrodes. The mechanical collapse of the welding area causes the spacing between the electrodes to decrease, leading to lower resistance. If the clamping force is too big or if the current is too high, the work piece can eventually burn through, leading to expulsion. Expulsion will cause a sudden drop of resistance in the last stage, which is mostly undesirable and should be avoided by optimizing the welding technique.

RSW was empirically modeled as a lobe curve (Kim, 1988) where weld current and weld time are mutually correlated to produce the optimum welding nugget. Typically, weld time is within 1/5 second, while the welding current is between 8kA to15 kA. However, low current requires a longer weld time to reach an acceptable size weld nugget, while shorter weld time is needed for high weld current to avoid expulsion, where liquid weld nugget grows to the edge and eventually breaks out of the surface of the sheets. As the lobe curve was developed as an empirical measure, it could only be treated as references, while various situational parameters should also be considered.

Han conducted a heat transfer study. (Han et al., n.d., 1989) An axisymmetric heat transfer model was developed and solved with the FEA method. Temperature-dependent properties were utilized. The interface electrical contact resistance was assumed to vary with the applied electrode force, which means that the contact resistance is constant and evenly distributed during the process. Temperature measurements were performed experimentally, and the agreement between these heat curves and the simulated heat curves is good.

Cho developed a thermoelectric axisymmetric model, solved with the finite difference method. (Cho et al., n.d., 1988)Temperature-dependent properties for the metal sheets were used. Hardness has been modeled as a function of temperature. The hardness was further derived as parameters to electrical and thermal contact resistance. The density of electrical current at the contacting surfaces is evenly distributed. Thus, the interface heat generation is uniform in the radial direction. The model is validated by comparing the weld nugget diameters received with experimentally measured nuggets. The error of the model was 15-20%.

Zhang developed a commercial software, SORPAS, based on an axisymmetric, coupled thermal-electrical-mechanical-metallurgical model. (Zhang, 2003) The metallurgical model is not described in detail, but it calculates the phase transformation, i.e., solid phase to liquid phase. The material properties depend on temperature. The thermal model neglects the convection in the weld

pool. The electrical model is derived from the governing equation for the electric potential. The contact resistance is modeled using the Wanheim and Bay model.

Feulvarch et al. proposed a thermal-electrical-mechanic-metallurgical model to express the weld nugget growth. (Feulvarch et al., 2006) The thermal and electrical part is modified to be expressed in terms of enthalpy instead of temperature. The metallurgical contribution to the thermal analysis consists of phase-dependent thermal properties that are assembled to be the properties of the steel by a mixture rule. The microstructural evolution is calculated with a model based on a Continuous Cooling Transformation (CCT) diagram. The metallurgical coupling also affects mechanical calculations.

Most metal defects occur during the solid-liquid temperature range. RSW is a fast-melting and cooling process, and therefore it has a high potential to induce defects. In RSW, with liquid and solid co-existing inside a thin metal sheet, melting and solidification processes must be closely monitored to ensure the optimum welding nugget while introducing the least number of defects. In this dissertation, the melting and solidification processes are studied from physical, mathematical, and simulative aspects, with an emphasis on rheological analysis and thermal analysis of the binary alloys.

Binder Jet Printing

Process Overview of Binder Jet Printing

Binder jetting printing (BJP) is a rapidly emerging additive manufacturing method among metal powder engineering industries. The printhead selectively deposits binder onto metal powder bed based on the layer by layer CAD design during the binder jet printing process. After the roller spreads over a new layer of metal powder, the binder deposition process will be continued until the designed part has been built in the printing chamber. The green part then undergoes sintering and heat treatment processes to achieve the finished product. BJP was first established in 1993 and has been implemented and commercialized as one of the none-fusion powder bed additive manufacturing methods. (Mostafaei et al., 2021)

BJP has the following strengths: (1) The R&D cycle can be extensively reduced due to saving the expenditures related to molding, machining, and assembly processes; (2) intricate detailing can be realized with simple CAD layer designs; and (3) materials, energy, and labors can

be drastically minimized, making BJP both economically and environmentally friendly. (Wheat et al., 2018) When compared to other methods of additive manufacturing, binder jet printing still has its superiorities: (1) BJP generates fewer defects related to stress concentration or surface tension without layer's fusion during the prototyping stage; (2) BJP process can be practiced on a wide selection of materials; (3) The process is a relatively energy-conserving manufacturing method since it requires no laser or electron beam energy source. (Mostafaei et al., 2021)

To obtain a well-functioning binder jet printed mechanical part, mechanical properties, corrosion resistance, and dimension tolerance need to be considered during manufacturing. As the binder evaporates and metal powders partially melt in the sintering process, the fuse level of shrinkage can be affected by several parameters, including powder properties, powder compaction, binder level, and sintering condition. (Wang & Zhao, 2017) More compact, smaller metal particles with a lower level of liquid binder will lower the shrinkage rate and decrease the printing efficiency and green part integrity.

Modeling Review of Binder Jet Printing

As binder jetting manufacturing is rapidly developing, studies on sintering shrinkage analysis are emerging. However, most current research focuses on experimental analysis of a limited selection of alloys, while mathematical and simulative modeling research is sparse. (Rishmawi et al., 2018)

In the study conducted by Mostafaei, binder jetting green parts with powder alloy 625 were sintered under different temperatures to compare the results. (Mostafaei et al., 2016). The binder used mainly consists of ethylene glycol monobutyl. The alloy 625 powder was manufactured by vacuum-melted atomization under argon gas. The final powder diameters are ranged from 16 to 53 μm. During the curing process, the printed part was cured in a vacuum atmosphere at 175°C. Alumina powders were used as curing aid. After curing, the parts are sintered at 1200°C, 1240°C, 1280°C, 1290°C, 1300°C for four hours and then slow-cooled. The final microstructures of the sintered parts indicate that higher sintering temperature leads to a more condensed microstructure and less porosity. Porosity is one of the biggest concerns for powder metallurgy. It can induce stress concentration which will lead to cracking. However, higher temperature also leads to grain growth, which will have a negative impact on the strength of the material. Since the liquidus temperature of alloy 625 is 1283°C. 1280°C is the best temperature to achieve a relatively high

density (99.6% of the bulk density) while maintaining a solid structure from the green part for alloy 625. Dimensional shrinkage from the green part to sintered part is around 30%, which indicates a high level of anisotropy.

In the study of Wheat., etc., Grade 1 commercially pure titanium powder was used for binder jetting printing. (Wheat et al., 2018) The powders were manufactured through plasma atomization, which yielded particle parameters of 45 μm-150 μm and was categorized into different group studies. The printer is a modified 310Plus binder jetting printer acquired by 3D Systems with the standard ZB60 liquid binder. The study conducted both non-densifying sintering at 1000 °C as well as densifying sintering at 1400 °C. As part of the empirical study, it was found that courser metal powder will lead to a lower sintered density but also lower product quality. On the other hand, finer powder yields a large amount of shrinkage, which leads to difficulty in achieving and maintaining intricate and complicated designs for the final products.

In 2006, general motor patented deoxidizing and coating the aluminum particles with copper or other materials for additive manufacturing powder bed. (Jr et al., n.d. 2004) Oxide-free 6061 aluminum alloy was tested with coating metal such as Cu, Ni, Zn, or Sn. Aluminum powders were manufactured through gas-atomization or 'Alcoa Process', where high-pressure gas encroaches on molten metal to propel the articles upwardly into a circulating stream of cooling gas. Powder diameters are between 60 um and 140 um. Binder jetting layer thickness is 1 mm to 5 mm. Spherical powders will be produced through this process, which is beneficial as it enables smooth and evenly layer distribution during the binder jetting process. After aluminum powders have been manufactured, the particles will be deoxidized preferably before going through the coating process. With chemical vapor deposition on a recirculating, fast fluidized bed, a thin coating of Cu or Ni, Zn, and Sn (0.1% ~ 6% by weight of the particle) will be on each aluminum particle, providing a layer for safe transportation, storage as well as an alloying element. The as-printed part will be sinter at 610°C for about 15 minutes in an inert atmosphere with a sintering aid comprising 50% Mg. Cu will react with Al during the sintering process, initially form a liquid phase, and react and solidify to bond the article together. The inner core of each aluminum particle will stay solid during the sintering process to provide structural stability for the final product. Lastly, post-processing treatment needs to be performed to achieve the desired mechanical properties.

Anton Jansson, etc. have proposed a method for determining the scale factor on shrinkage of binder jetting manufacturing in 2016. (Jansson & Edholm, 2016)With data from approximately

100 steel components printed with different measurements, they delivered a functional scale factor to predict the shrinkage rate of the product to be made. The designed MatLab program generates the dimension of the green part based on the expected final product dimension. The study also dived into the possible variables affecting the shrinkage, e.g., direction, gravity, sintering, powder, length, and relative length. The scale factor is found to have a strong relationship with the direction and length of the component.

In this dissertation, the authors have proposed the analytical mathematical models on the phase transformation process of binary alloys, which provides a theoretical foundation to a diversity of metallurgical engineering problems, including RSW and BJP. COMSOL Multiphysics is further implemented to simulate welding nugget formation during RSW as well as shrinkage development of the BJP green part sintering process. Heat transfer and structural mechanics module has been applied to the model based on the proposed mathematical model.

RHEOLOGICAL CHARACTERIZATION

The Journal of COMSOL Inc provided permission for me to publish this article titled COMSOL Implementation of Binder Jet Printing Densification Model in Automatic Valve System in this dissertation. Permission letters are attached in Appendix I. The following statement is indorsed by all authors: research structure and idea: Sun, R.; experiment and model execution: Sun, R.and Liu, H.; examination and conclusion of data: Sun, R, and Zhang, H.; paper outline formulation: Sun, R.; The dissertation manuscript has received approval from all mentioned authors.

The Journal of Journal of Multidisciplinary Engineering Science and Technology (JMEST) provided permission for me to publish this article titled Mathematical Modeling of Resistance Spot Welding in this dissertation. Permission letters are attached in Appendix I. The following statement is indorsed by all authors: research structure and idea: Zhang, H. and Das, M.; experiment and model execution: Sun, R., and Han, Q.; examination and conclusion of data: Sun, R, and Zhang, H.; paper outline formulation: Sun, R. and Zhang, H.; The dissertation manuscript has received approval from all mentioned authors.

Physical Modeling

Physical Analysis of Resistance Spot Welding

During RSW, heat is generated between the two metal sheetings. Part of metal at the interface becomes liquidus contained by the solid exterior of the workpiece. The state of the area around the electrode tips consists of the solidus, liquidus, and mushy metal phases. Liquid metal flux leads to shear rates and shearing time variations, which lead to viscosity fluatation.(Hildebrand & Lamoreaux, 1976) Thus, final weld morphology has to take the rheological properties of the material into account.

The heat transfer and flow dynamics are complex during RSW as well. After the current is on, the heat starts to dissipate in an ellipsoid shape from the center of the welded area. The heat expansion can be interpreted as the combination of two traveling directions. First, heat expanding towards the diameter direction and into a larger ellipsoid. Second, heat also spreading further along the horizontal direction as the workpiece is being pressed down. As the temperature of the welding area varies, the viscosity will be different as well.

Before the surfaces of the work pieces melt down, the space between two surfaces can be seen as a resistor assembly made of surface dendrites, as seen in Figure 2. The surface roughness and contamination are heat concentration points during the resistance spot welding. Suppose there are N pairs of dendrites forming resistors and the kth pair of dendrite has its resistance R_k, which

generates Q_k amount of heat. The number of resistors is a function of the surface roughness R_a. Thus, it can be derived that:

$$\mathrm{N} = \mathrm{f}(R_a) \tag{9}$$

$$Q_t = \sum_{k=1}^{N} Q_k(R_k) \tag{10}$$

where Q_t is the heat being generated at the interface at the beginning of the RSW process.4

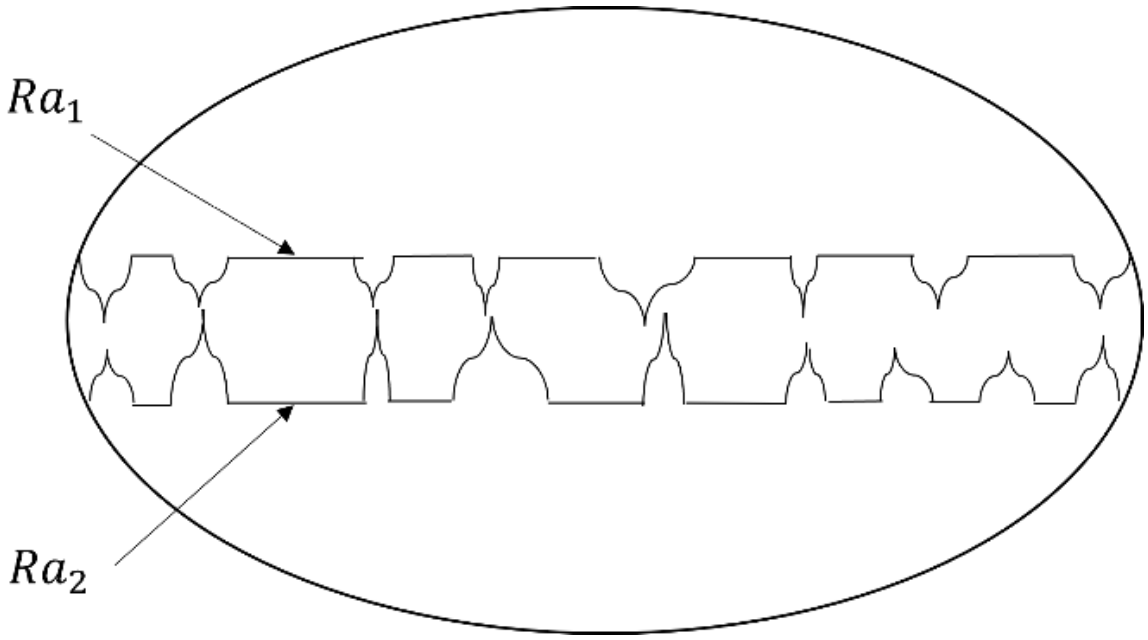

Figure 2 The schematic depiction of the enlarged welding surfaces

Before developing a mathematical model for the RSW process, it is imperative to study the rheological properties of liquid metals. Since the viscometer started to be implemented for measuring the viscosity of various matters, liquid metal has been categorized under Newtonian liquid, which means its viscosity remains the same value under different shear stresses. (Hildebrand & Lamoreaux, 1976)Various pieces of literature have discussed the viscosity of liquid metals. However, until very recently, liquid metals had always been under the assumption that it follows the principles of Newtonian liquid. However, according to Sun (C. Sun et al., 2007), Way,

(Way et al., 2007) and Jeyakuma, (Jeyakumar et al., 2011), it has been revealed that there are shear-thinning liquid metal systems, which means that not all liquid metals are Newtonian liquids.

There are two mechanisms collaboratively affecting the viscosity of liquid metals. First, when the liquid metal temperature rises, the collision between atoms accelerates, which will increase viscosity. Second, the spacing between atoms will grow larger as temperature rises, lowering the gravitational force between them, resulting in a decrease in viscosity. As in $F = G\frac{m_1 m_2}{d}$, when the spacing d decreases, the gravitational force F increases. For liquid metals, spacing change-induced viscosity drop will have a more significant effect than collision acceleration viscosity rise. Thus, the superposed effect results in a decrease of viscosity as temperature rises, which is in line with Arrhenius's relationship $\eta = Ae^{-B/T}$.

In the RSW process, the volume of liquid metal increases as temperature rises due to thermal expansion. In the ideal situation, the expansion of the workpiece in every direction should have an equal thermal expansion coefficient. However, the areas requiring the RSW process are mainly along the edges, where the inhomogeneity of phases concentrates. The heterogeneity and narrow boundary conditions sometimes lead to uneven thermal expansion. For a standard automobile RSW workpiece, the thickness of the workpiece stays constant. Thus, the z-direction (clamping direction of the electrodes) will have a constant boundary condition. However, if the welding spot is located along the edge, at the corner, or the end of a thin metal strip, there may be situations where thermal expansion does not follow the equation due to limited space for the expanding of heat. In this extreme situation, the results of thermal expansion will need empirical study and the assistance of experiments.

Resistance spot welding is a process involving solid metals transforming to semi-solid and liquid states. Three aspects of the rheological study can be introduced during the RSW process: solid-liquid metal rheology, casting rheology, and plastic processing rheology.

During the resistance spot welding process, as the welding interfaces heat up and begin to melt, the semi-solid metal inside the welding area exhibits unique rheological properties in the process. (D. Dickinson et al., 1980)The entire workpiece cannot be regarded as a simple Hookean solid or Newtonian liquid. (Modigell et al., 2006)Between the solid exterior and the liquid core, solid metal crystal clusters of metal float around liquid metal in different shapes such as spheres, spikes, and dendrites. Under the clamping force of RSW electrodes, the unique morphology of a solid metal exterior containing a semi-solid layer and a liquid core exhibits rheological properties

such as shear thinning and thixotropy. Meanwhile, as diffusivity of most solid and liquid metals differs profoundly ($D_l \sim 10^{-5} cm^3/s$, $D_s \sim 10^{-8} cm^3/s$), solute inside liquid state diffuses much faster. The solute concentration gradient between liquid and solid metal during the RSW process can lead to an uneven phase distribution. With the proper model, these properties can be taken into account at refining the simulation of the final welding product.

In RSW, as heating processes, the asperities in the contact areas of two work pieces soften and eventually melt down. (D. Dickinson et al., 1980) In the meantime, the clamping force of the electrodes will plastically deform the molten welding area. The plastic deformation not only causes the resistivity between the workpieces to drop, but it will also influence the microstructure of the welding nugget. As the deformation process happens in a sandwich structure containing a solid metal exterior with a semi-solid layer and a liquid core, it cannot be regarded as a simple solid-state deformation. Thus, final weld morphology has to take the rheological properties of the material into account.

For resistance spot welding, thermal expansion and collapsing of the welding area contribute to the final modeling of the RSW process and workpiece configuration variations. The model can be divided into three parts. First, the heat generated from the electrical current will heat up the work piece, resulting in an initial thermal expansion of the solid metal. The heat will also be conducted to the area surrounding it. The thermal expansion equation for solidus metal is as follows:

$$\Delta L = L_f - L_0 = \alpha \Delta T L_0 \tag{11}$$

where ΔL is the expanded length, L_f and L_0 being the final and original lengths, ΔT the temperature change and α the thermal expansion coefficient.

Secondly, as temperature approaching the melting point of the metal, phase change will begin, a part of the heat generated will be absorbed for phase changing. (Reid et al., 1987) Once the metal has completed the phase change and becomes liquid state, the thermal expansion mechanism changes from interatomic interactions to an increase in the free volume holes. (C. Sun et al., 2007)As temperature rises, there will be initiation and growth of free volume holes in the liquid. Due to higher mobility of the atoms, higher thermal power will result in larger frequency

and amplitude of atom. The change will lead to a higher thermal expansion coefficient and consequently a faster expansion rate of the welded area.

Finally, while the volume of the metal is growing, the shape of the kernel is also altering. The phase change will result in a change of mechanical structure. As the kernel grows, the shape will change from a sphere to an ellipsoid due to mechanical collapse, resulting in a smaller distance between two electrodes.

Thus, simulation of the welding area is of great importance and convenience. It provides real-time visual proof of the weld development without destructing the weld pieces or compromising overly welded parts. However, there has been limited research on modeling the resistance spot welding process. While previous researches have been performed to analyze the process, most of them are conducted from an experiment-observing point of view, and a sophisticated mathematical model for the welding process is lacking. (Jeyakumar et al., 2011) This dissertation proposed to analyze the melting and solidification processes of resistance spot welding and develop an analytical mathematical model to describe the thermal and dimensional evolution.

Physical Analysis of Binder Jet Printing

The Binder Jetting process has a lot to do with powder metallurgy. Thus, the process is a porous structure of metal powder (green body) that is sintered to obtain a close to fully dense body. The shrinkage is not homogenous, which means that the shrinkage is different in each direction and possibly dependent on other variables.

Compared to other additive manufacturing methods, such as selective laser sintering and electron beam melting, the binder jet printed part has a less potential risk of thermal-induced residual stress. The novel configuration allows for a more integrated electro-hydraulic valve system redesign. Replacing the die casting method, this fast manufacturing cycle is time and material-saving. The biggest challenge for binder jet printing is the sintering shrinkage of the green body. As shown in Figure 3, due to evaporation of the binder as well as partial melting and re-solidification of metal powders, the final product could end up with porosity and a high level of anisotropy.

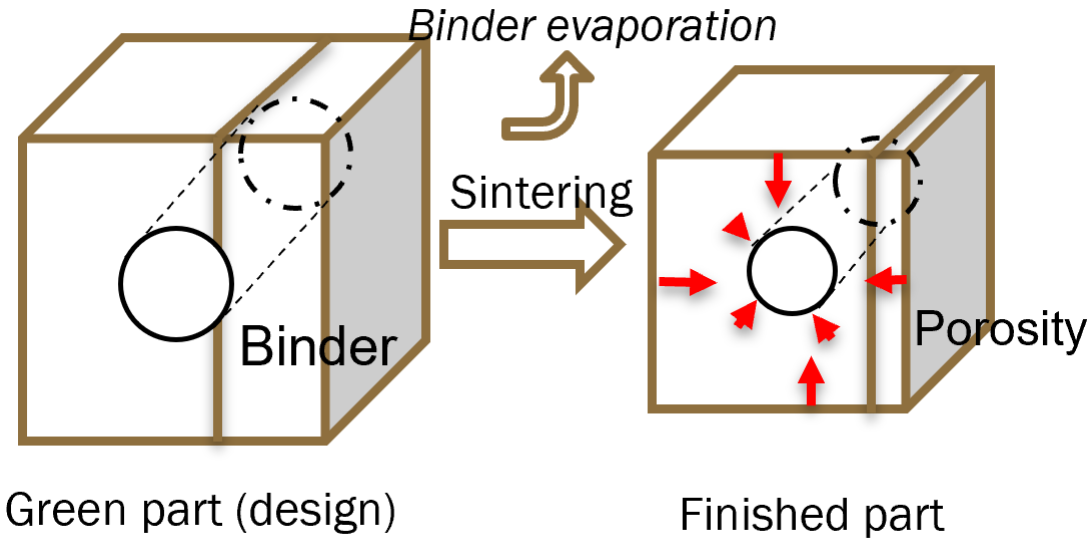

Figure 3 Depiction of sintering shrinkage due to binder evaporation and melting

During the sintering stage, the green part with a high percentage of a binder mixed in will first start with surface transport, binder evaporation, surficial necking. After the binder has been evaporated, local diffusion will propagate with the metal powder clusters. In the meantime, larger necking and closing of pores will begin to form, leading to the potential formation of porosity. At the end stage of sintering, bulk diffusion and agglomeration will occur in the green part, resulting in a much more compact final part.

Most BJP shrinkage analysis has been performed empirically without a systematic study on the densification thermal transition process. Thus, more systematic modeling is in need for analyzing the sintering of binder jet printed parts. Particularly, the phase transformation process needs to be thermally and mathematically expressed with metal properties, binder properties, and sintering conditions to be implemented and optimized in simulation platforms.

Currently, in the steel production industry, the binder jet printing process has a great potential to produce steel components with significant mechanical behaviors. Various examples have shown that steel products with desirable ability can be obtained with this method. But some significant challenges still need to be considered.

As discussed in the previous chapter, during the sintering stage, the level of shrinkage can be affected by several parameters, including powder properties, powder compaction, binder level, and sintering condition. (Toyserkani et al., 2004) More compact, smaller metal particles with a

lower level of liquid binder will lead to a lower shrinkage rate, but in consequence, will also decrease the printing efficiency and green part integrity. As the additive manufacturing process is an emerging technique for mass manufacturing, building standard procedures are still under constant modification. Without a standard of procedures and machine accuracy, it is challenging to consolidate the data. Recent researches still focus on specific material or manufacturing methods. As the AM community grows, the development of standard procedures is inevitable to help the whole community analyze the data more effectively. During production, the prediction of optimal printing parameters needs to be precise to ensure product quality and efficiency. It is not agile work to iterate by external and internal evaluation to find optimal printing parameters every time. If printing parameters can be predicted based on data analyses at the design process, the final part can be expected with better dimensional accuracy and surface quality with excellent efficiency. For industrial manufacturing, high-speed fabricating is an inevitable factor in producing. However, some processes, especially drying time and printing method, greatly enlarge the manufacturing time in the current technology. Fabrication speed is significantly associated with part quality in all techniques. Increasing this speed with a keeping or even increasing in quality will be the challenge in the future of the BJP process. (Sheydaeian, 2017).

There are three stages of sintering. In the initial stage, particles begin to melt on the exterior, and surface diffusion occurs while the liquid binder evaporates. At the end of the initial stage, density can reach 60% of bulk density. In the intermediate stage, metal particles continue to melt and form larger necking among each other. Closed pores begin to form while the end density can reach 92%. In the final stage, most particles have melted together. Bulk diffusion begins while closed pores agglomerate into porosity in the final product. However, the addition of sintering aid such as copper can significantly relieve the final porosity as copper has a lower melting temperature. During the sintering process, molten sintering aid can flow into the forming pores to prevent the further formation of porosity in the final stage.

Binder jetting manufacturing is still a developing technique. Studies on shrinkage analysis are limited, especially for BJP of aluminum powder. The product from the BJP process is a porous structure of metal powder (green body), which is sintered to obtain a close to fully dense body. During the sintering, the green body shrinks due to partial melting and re-solidification. The current challenges in binder jet printing result in a demand for accurate modeling during the sintering stage to better monitor the final product dimension. (Dini et al., 2020)

Analytical Mathematical Modeling

Assumptions

In the study of micro-scale welding and casting, a one-dimensional heat conduction process can be assumed to take place on a semi-infinite slab. As shown in Figure 4, nugget formation during RSW is depicted. In Figure 5, molten and solid regions are demonstrated during the sintering of the binder jet printed green part. X arrow represents the direction of heat flux. This study will be focused on a closed system situation and design control laws according to the model describing this condition depicted in Figure 4 and Figure 5. Metal sheets and metal powders will be a metal alloy with specific solubility, and processing parameters are within the required range.

The assumptions of the model are:

(1) There is no fluid flow and no internal heat generation in solid and liquid phases, only conduction.

(2) The solid and liquid phases are separated by a flat interface. Its location is noted as $\xi^*(t)$.

(3) Local equilibrium at the interface. Both liquidus and solidus lines are linear.

(4) Mushy zone in-between liquid and solid phases is of negligible thickness.

(5) Thermal properties in solid and liquid are equal.

(6) The melting and solidification growth is only in the X-direction until the full size is formed. Conduction only occurs in the X-direction.

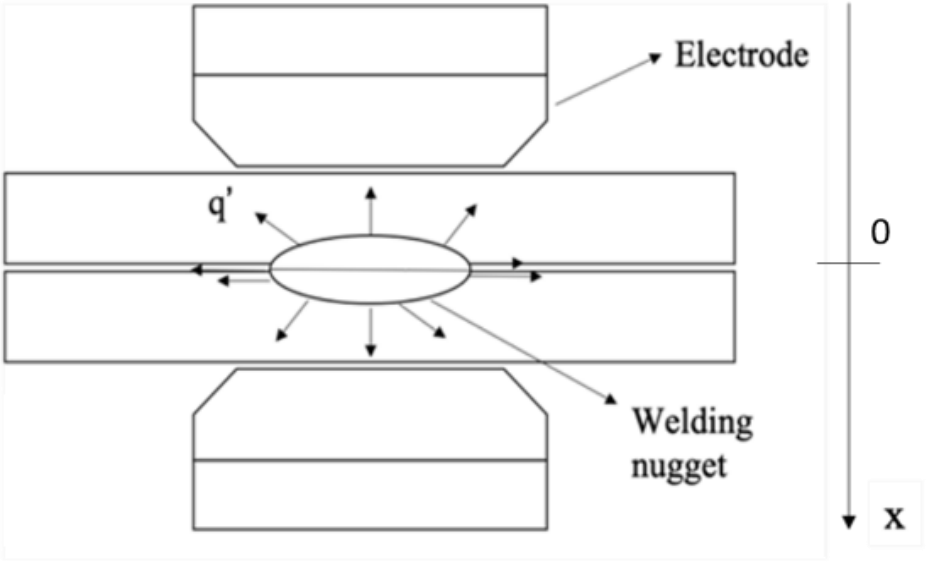

Figure 4 Depiction of resistance spot welding model

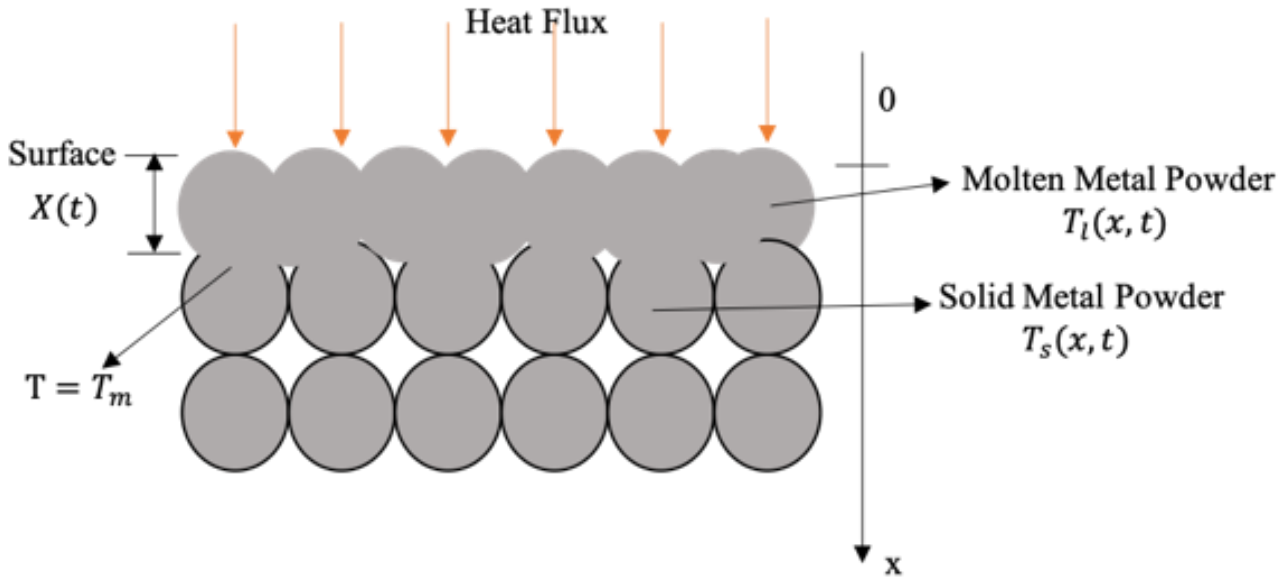

Figure 5 Binder jet printed green part under sintering

Heat Transfer Model during Melting

Model schematic is depicted in Figure 4 and Figure 5. The heat flux is spreading in the direction of the X-axis. The metal sheets and metal powder layers are in the YZ plane. The temperature of the interface can be calculated from the melting temperature of the binary phase alloy based on the composition. Governing Equations are as following: (Xie et al., 1997)

$$\frac{\partial^2 T_l(x,t)}{\partial x^2} - \frac{1}{\alpha_l}\frac{\partial T_l(x,t)}{\partial t} = 0 \quad at \quad 0 \le x \le X(t) \tag{12}$$

$$\frac{\partial^2 T_s(x,t)}{\partial x^2} - \frac{1}{\alpha_s}\frac{\partial T_s(x,t)}{\partial t} = 0 \quad at \quad X(t) \le x \le \infty \tag{13}$$

$$T_l(x,t) = T_s(x,t) = T_m, \qquad x = X(t) \tag{14}$$

$$k_l\frac{\partial T_l(x,t)}{\partial x} = k_s\frac{\partial T_s(x,t)}{\partial x} - \rho L\frac{dX(t)}{dt}, \quad x = X(t) \tag{15}$$

$$-k_l\frac{\partial T_l(x,t)}{\partial x} = \eta, \; x = 0 \tag{16}$$

$$T_s(x,t) = T_0, \qquad x \to \infty \tag{17}$$

$$T_s(x,t) = T_0, \qquad t = 0 \tag{18}$$

$$X(t) = 0, \qquad t = 0 \tag{19}$$

where T_i is the temperature; α_i is the thermal diffusivity and k_i is the thermal conductivity of the ith phase. If $i = l$, the equation represents the liquid phase. If $i = s$, it represents a solid phase. x represents the distance from the surface to the solid-liquid interface. t represents the heating time. T_m is the melting point of the alloy. r is the density. L is the latent heat of fusion. T_0 is the initial temperature. η is the absorbed heat flux.

The analytical solution of the governing equations is:

$$T_l(x,t) = T_m - \frac{\eta}{k_l}[x - X(t)] + \frac{\eta}{2\alpha_l k_l\left[1 + \frac{X(t)}{\alpha_l}\frac{dX(t)}{dt}\right]} \times \frac{dX(t)}{dt}[x^2 - X^2(t)], \qquad 0 \le x \le X(t) \tag{20}$$

$$T_s(x,t) = T_m - (T_m - T_0)\left\{1 - \exp\left[-\frac{1}{\alpha_s}\frac{dX(t)}{dt}\big(x - X(t)\big)\right]\right\}$$
$$X(t) \le x \le \infty \tag{21}$$

$$X(t) = \left[-\frac{b_0}{2} + \left(\frac{b_0^2}{4} + \frac{a_0^3}{27}\right)^{\frac{1}{2}}\right]^{\frac{1}{3}} + \left[-\frac{b_0}{2} - \left(\frac{b_0^2}{4} + \frac{a_0^3}{27}\right)^{\frac{1}{2}}\right]^{\frac{1}{3}} - \frac{a_l m_s}{16\eta}, \tag{22}$$

where

$$a_0 = \frac{3{a_l}^2{m_s}^2}{256\eta^2}\left(\frac{192\eta^2 t}{a_l{m_s}^2} + 31\right), \tag{23a}$$

$$b_0 = -\frac{a_l}{8\eta}\left[\frac{{a_l}^2{m_s}^3}{256\eta^2}\left(\frac{288\eta^2 t}{a_l{m_s}^2} + 47\right) + \frac{t(18\eta^2 t + 3\alpha_l{m_s}^2)}{m_s}\right] \tag{23b}$$

$$m_s = \rho[c_p(T_m - T_0) + L] \tag{23c}$$

Heat Transfer Model During Solidification

The solidification process is a planar front solidification of binary alloy with a semi-infinite mold. (Dantzig & Rappaz, 2016) The governing equation of the planar front solidification of the alloy is as follows:

$$\frac{d\theta_s}{d\tau} = \frac{d^2\theta_s}{d\xi^2} \quad at \quad 0 \le \xi \le \xi^*(\tau) \tag{24}$$

$$\frac{d\theta_l}{d\tau} = \frac{d^2\theta_l}{d\xi^2} \quad at \quad \xi^* \le \xi \le 1 \tag{25}$$

where θ_s is the relative solidus temperature, θ_l is the relative liquidus temperature, τ is the dimensionless time, ξ is the relative position, and ξ^* is the relative interface position (as defined in Eq. (26)-(30)).

$$\theta_s = \frac{T_s - T_0}{T_\infty - T_0} \tag{26}$$

$$\theta_l = \frac{T_l - T_0}{T_\infty - T_0} \tag{27}$$

$$\tau = \frac{\alpha t}{L^2} \tag{28}$$

$$\xi = \frac{x}{L} \tag{29}$$

$$\xi^* = \frac{x^*}{L} \tag{30}$$

The boundary conditions and initial conditions are as following:

$$\theta_s = 0 \quad at \quad \xi = 0 \tag{31}$$

$$\theta_s = \theta^* \quad at \quad \xi = \xi^*(\tau) \tag{32}$$

$$\frac{1}{Ste}\ \frac{d\xi^*}{d\tau} = \frac{d\theta_s}{d\xi} - \frac{d\theta_l}{d\xi}\ \ at\ \ \xi = \xi^*(\tau) \tag{33}$$

$$\theta_l = 1 \quad at \quad \xi = 1 \tag{34}$$

$$\theta_l = 1 \quad at \quad \tau = 1 \tag{35}$$

$$\xi^* = 1 - \delta \quad at \quad \tau = 0 \tag{36}$$

$$Ste = \frac{c_p(T_\infty - T_0)}{L_f} \tag{37}$$

where Ste is Stefan number defined in Eq. (37), and δ is the relative liquid percentage. In the case of RSW, δ should be between 0-70% of sheet thickness in order to avoid expulsion.

The established model calculates solidification time and creates a transient temperature profile of the subject. A binary alloy 1-D planar heat transfer model is implemented. (Dantzig & Rappaz, 2016)

From the first part of the model, the user may specify the relative liquid percentage δ. The solid-liquid interface position does not, therefore, begin at $x = 0$ during solidification. Governing equations are adapted to satisfy the initial and side conditions.

The analytical solution for Eq. (24) and (25) with the boundary conditions (Eq. (31)-(37)) is as follows:

$$\theta_s = \frac{\theta^*}{\mathrm{erf}(\phi)}\,\mathrm{erf}\left(\frac{\xi}{2\sqrt{\tau} + \frac{(1-\delta)}{\phi}}\right) \tag{38}$$

$$\theta_l = 1 - \frac{1-\theta^*}{\mathrm{erfc}(\phi)}\mathrm{erfc}\left(\frac{\xi}{2\sqrt{\tau}+\frac{(1-\delta)}{\phi}}\right) \tag{39}$$

$$\xi^* = 2\phi\sqrt{\tau} + (1-\delta) \tag{40}$$

$$\theta^* = \mathrm{erf}(\phi)\left(1+\frac{\sqrt{\pi}}{Ste}\phi\exp(\phi^2)\,\mathrm{erfc}(\phi)\right) \tag{41}$$

$$\mathrm{erf}(x) = \frac{2}{\sqrt{\pi}}\int_0^x e^{-t^2}dt \tag{42}$$

where $\mathrm{erfc}(x) = 1 - \mathrm{erf}(x)$ and ϕ can be derived from Eq. (46).

$$\left\{\theta_f - \mathrm{erf}(\phi)\left(1+\frac{\sqrt{\pi}}{Ste}\phi\exp(\phi^2)\,\mathrm{erfc}(\phi)\right)\right\}$$
$$\times\left\{1-\sqrt{\pi Le}(1-k_0)\phi\exp(\phi^2 Le)\,\mathrm{erfc}\left(\phi\sqrt{Le}\right)\right\} = \frac{m_l C_0}{T_0 - T_\infty} \tag{43}$$

where θ_f is the dimensionless freezing point, Le is Lewis number, k_0 is the segregation coefficient, m_l is the liquidus slope, C_0 is the nominal composition, T_0 is hold temperature, and T_∞ the initial temperature. $\xi^* = 1$ when the solidification process ends and solidification time t_f can be calculated from it. Thus, solidification processes can be analytically calculated based on the above solution.

Python Modeling of the Solidification Process of Resistance Spot Welding

The model consists of two parts, the first addresses the welding time t_{weld}. The thickness of the welding nugget is modeled as a function of time. (R. Sun et al., 2019) Welding time in RSW is defined as the time when the welding electrodes have current running through them. The welding time may be calculated by specifying the nugget thickness and solving for time.

$$\xi(t_{weld}) = \lambda\sqrt{\alpha t_{weld}} \tag{44}$$

$$\alpha = \frac{\mathrm{k}}{\rho \mathrm{c_p}} \tag{45}$$

where λ is the solution of

$$\lambda \exp(\lambda^2)\,\mathrm{erf}(\lambda) = \frac{c_p\left(T_\infty - T_f\right)}{L_f\sqrt{\pi}} \tag{46}$$

In Equation (44), $\xi(t_{weld})$ is the nugget size under the welding time of t_{weld} and α is the thermal diffusivity. In Equation (46), $\mathrm{erf}(x)$ is the error function, c_p is the specific heat, L_f is the melting heat, T_∞ is the superheat temperature, and T_f is the solidification temperature of the pure solvent.

The solidification mathematical model was translated to Python with two final outputs, the total RSW time and the transient temperature profile. The flow chart is shown in Figure 6. Multiple inputs are required to run the simulation. Material inputs are as follows: C_0, m_l, c_{ps}, L_f, k_s, ρ_{solid}, T_f, k_0, and Le. Conditional inputs are T_∞ and T_0. Geometric inputs are L and δ.

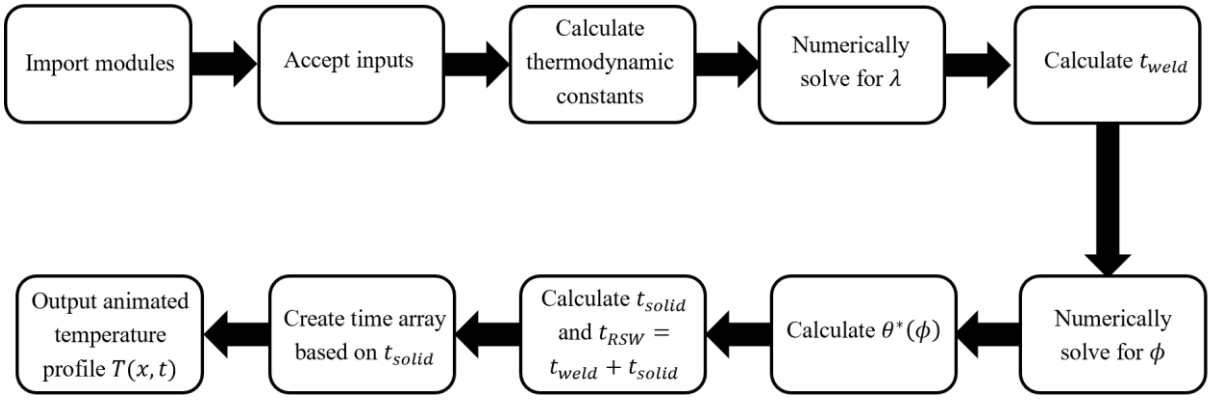

Figure 6 Python flow chart for solidification modeling during RSW

Once inputs are given, the program will calculate the thermodynamic constants α and Ste. The constant, λ, in Equation (46) is solved numerically. t_{weld} is calculated by substituting $\delta * (L)$ for $\xi(t_{weld})$ in Equation (44) and solving for t_{weld}.

The simulation begins the second part by numerically solving for constant ϕ and calculating solidification time, t_f. Total RSW time is defined in Equation (47). An array of 1000 times from 0 to t_f is created.

$$t_{RSW} = t_{weld} + t_f \tag{47}$$

For each value of time in the time array, a temperature profile through the sheet thickness is calculated as a piecewise function. All Python codes are included in Appendix II.

An animation script was used to animate the plot. (Vanderplas, 2013) One particular example for RSW has been calculated and the result temperature profile progress is shown below. The case use for calculation is resistance sport welding of two 2 mm thick mild steel sheetings. Material inputs are as follows: $C_0 = 0.05\, mass\%$, $m_l = -81.1$ K/mass%, m_s=-478 K/mass%, $c_{ps} = 820\, J/(kgK)$, $L_f = 276000\, J/kg$, k_s, $\rho_{solid} = 7000\, kg/m^3$, $T_f = 1538$ ℃,$\alpha = 54\, W/(mK)$, $k_0 = 0.17$, and $Le = 300\, \alpha/DI$. Conditional inputs are $T_\infty = 2000$ ℃ and $T_0 = 100$ ℃ . Geometric inputs are $L = 0.002\, mm$ and $\delta = 0.7$.

Based on the Python result, calculated welding time is : t_{weld} =0.40774 s. Calculated solidification time is $t_f =$ 0.1106 s. As a result , the total RSW time is $t_{RSW} = t_{weld} + t_f$ =0.51842 s. The case study is shown through the plot at $0\ s < t < t_f$ is shown in Figure 7 and plot at $t \approx t_f$ is shown in Figure 8. The animation of the transient temperature profile is displayed in Figure 9.

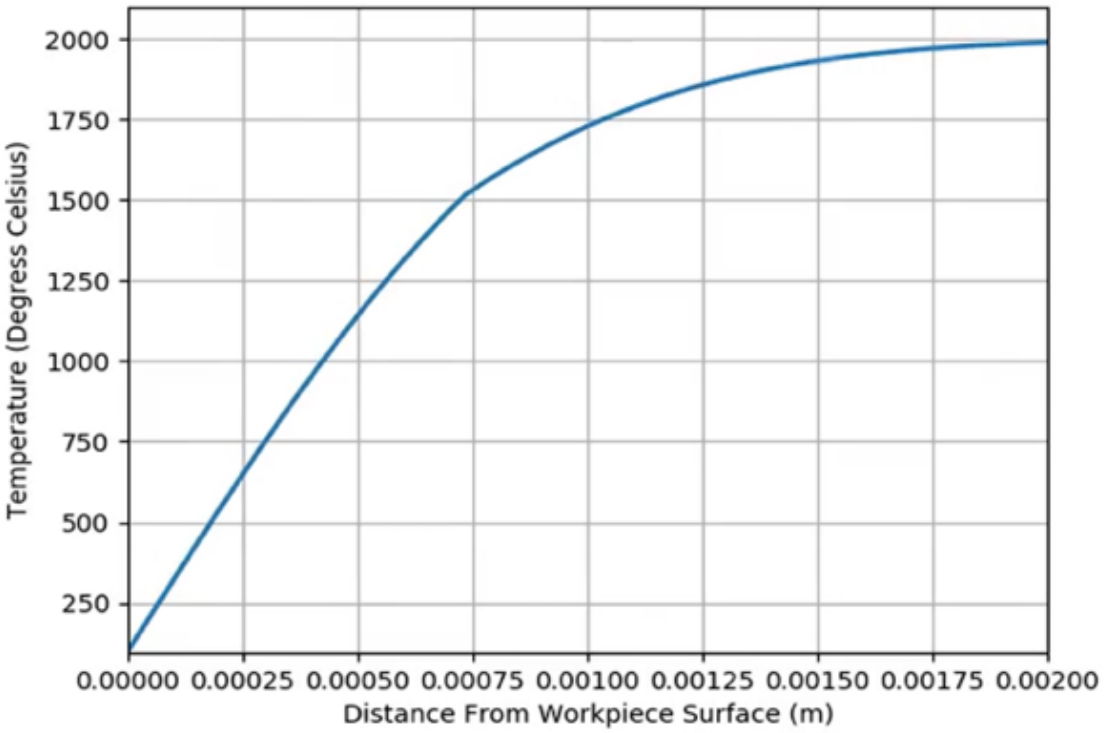

Figure 7 Transient temperature profiles at t≈0

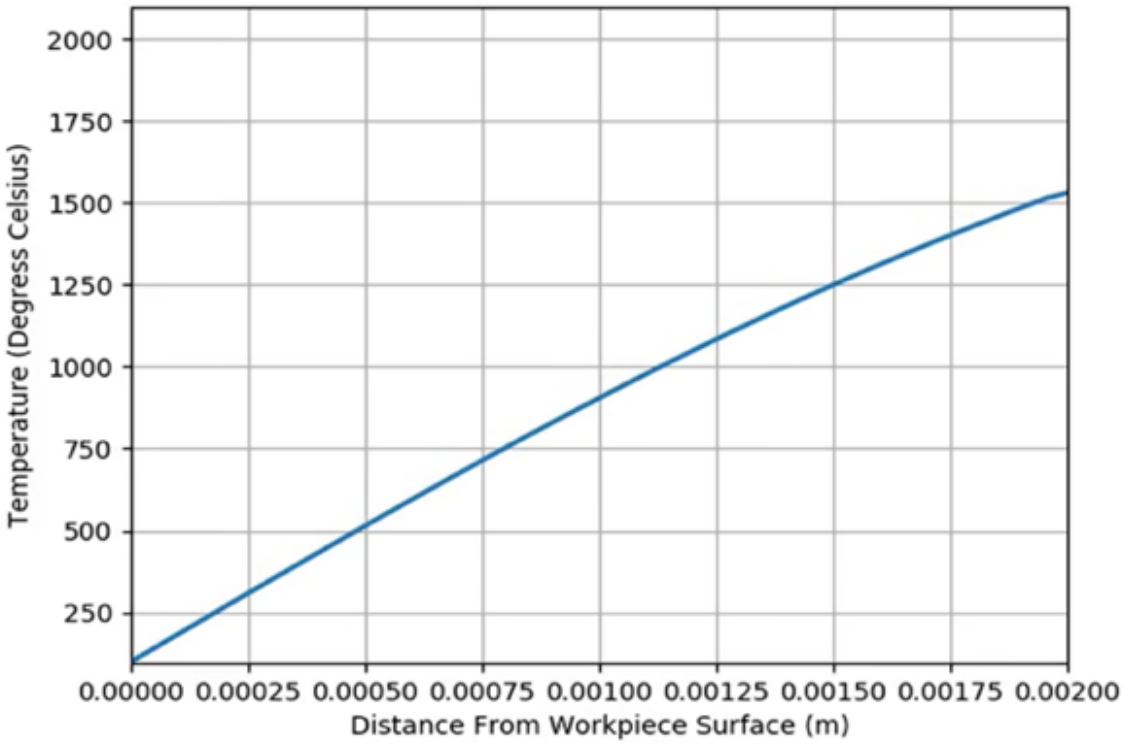

Figure 8 Transient temperature profiles at $t \approx t_f$

Figure 9 Animation of the transient temperature profile of the welded cross section during solidofication of RSW

SIMULATIVE MODELING WITH COMSOL MULTIPHYSICS

The Journal of COMSOL Inc provided permission for me to publish this article titled COMSOL Implementation of Binder Jet Printing Densification Model in Automatic Valve System in this dissertation. Permission letters are attached in Appendix I. The following statement are indorsed by all authors: research structure and idea: Sun, R.; experiment and model execution: Sun, R.and Liu, H.; examination and conclusion of data: Sun, R, and Zhang, H.; paper outline formulation: Sun, R.; The dissertation manuscript has received approval from all mentioned authors.

The Journal of Journal of Multidisciplinary Engineering Science and Technology (JMEST) provided permission for me to publish this article titled Mathematical Modeling of Resistance Spot Welding in this dissertation. Permission letters are attached in Appendix I. The following statement is indorsed by all authors: research structure and idea: Zhang, H. and Das, M.; experiment and model execution: Sun, R., and Han, Q.; examination and conclusion of data: Sun, R, and Zhang, H.; paper outline formulation: Sun, R. and Zhang, H.; The dissertation manuscript has received approval from all mentioned authors.

Simulation analysis and engineering modeling both originated from mathematical modeling. As one of the most acknowledged simulative software, COMSOL Multiphysics is integrated with MATLAB and has powerful mathematical computing abilities. (E. J. F. Dickinson et al., 2014) COMSOL Multiphysics is rooted in fundamental mathematical, physical theories, which offers a high level of adaptions regarding different models, especially where partial differential questions solver is needed. Unlike simulation software that encapsulates functions, such as ANSYS, COMSOL offers users secondary development and modification abilities. (Mayboudi, 2019) COMSOL Multiphysics software utilizes the finite element method (FEM) to discretize complex mathematical functions into many simple functions. (E. J. F. Dickinson et al., 2014) Like other FEM simulation software, COMSOL modeling comprises five essential components: model set up, materials specification, physics, boundary conditions definition, computation, and post-processing.

Simulation study of melting and solidification processes has always been essential to metallurgical engineering, beneficial to both theoretical and application progress. In particular, welding and casting industries rely heavily on the accuracy of melting and solidification characterizations. With the fast-paced progress of automobile industries, both traditional and newly emerged technologies require more detailed physical and mathematical metallurgical models to better monitor production progress. At the same time, the academic world is also in need of compatible theoretical and simulative modeling in line with technological progress. In this

chapter, simulation modeling two metallurgical manufacturing techniques will be studied: resistance spot welding (RSW) and binder jet printing (BJP).

COMSOL Multiphysics Modeling of Resistance Spot Welding

Resistance spot welding is highly utilized in body-in-white manufacturing. Conventional methods for testing the welding quality include destructive tests such as the peel test, which involves pulling the welded coupons apart and measure the nugget diameters. (Way et al., 2007) The other way to ensure the weld quality is to real-time monitoring the resistance between the welded area, as the resistance of it changes dynamically in different stages of the welding process. Sometimes it is also considered reasonable to generate a small amount of expulsion between the workpieces in order to ensure a tight and solid weld. However, all these methods compromise either unsatisfying weld products or uncertainty to the consistency of the weld quality. Simulation in the RSW process predicts the integrity of welding nuggets and reducing the number of destructive tests. It provides real-time visual proof of the weld development without destructing the weld pieces or compromising overly welded parts.

A geometric meshed model has been developed, as shown in Figure 10. Developed mathematical modeling is applied to COMSOL Multiphysics to simulate the thermal transfer and geometric development of the Resistance spot welding process. In Figure 11 and Figure 12, two steel sheets have been welded with superheated peak temperature to 2000℃ before being cooled down to 25℃ with water-cooled electrodes. As resistance spot welding is a rapid process, the entire simulation timelapse for temperature gradient and isothermal contour development is 2 seconds. The temperature gradient evolution demonstrates the heat transfer progress.

From Figure 11(a) to 11(d), the welding nugget temperature profile decreases as the welding process halts and the solidification of the welding nuggets progresses. However, thermal diffusion from the center of the welded area propagates, leading to a larger heat-affected zone over time. The hear-affected zone evolution over time is depicted from Figure 12(a) to 12(d). Thus, after the RSW process, the temperature in the welding nugget decreases not just through the water-cooled welding tips, also through the heat conduction of the surrounding metal sheets, leading to adjacent heat-affected zones. As a result, the yield strength, toughness, and corrosion resistance can be negatively affected by the grain growth propagation in the heat-affected zones.

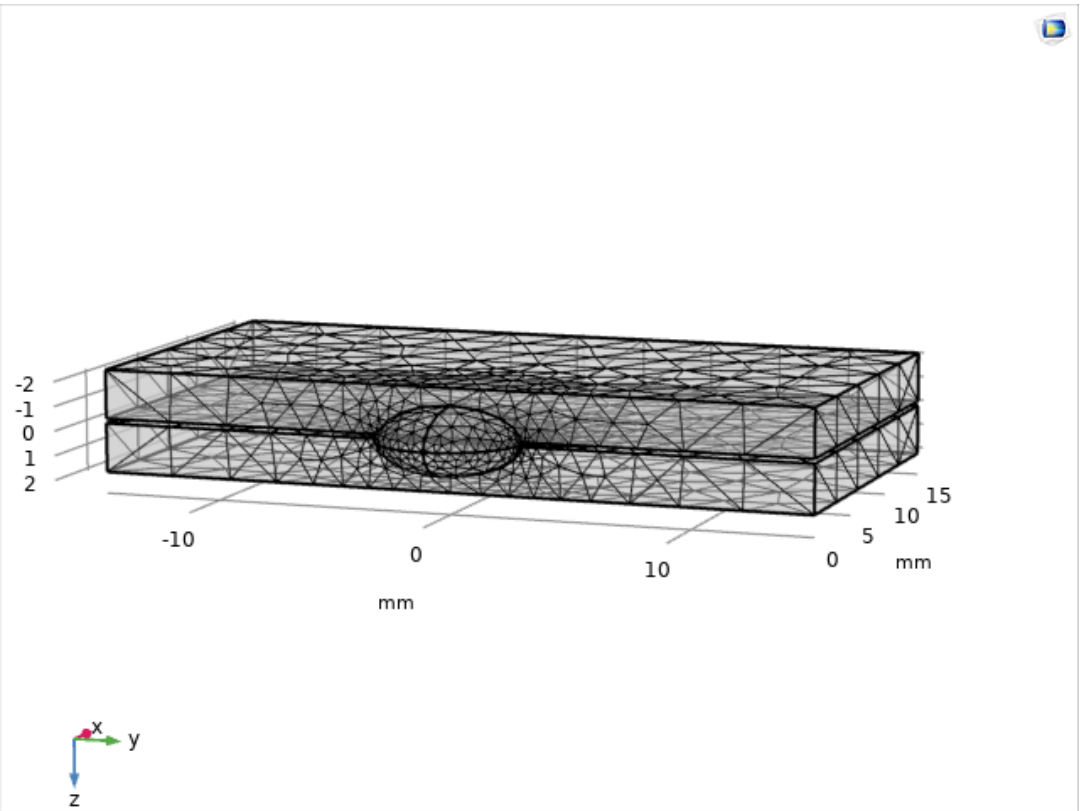

Figure 10 Meshed model of the RSW sheetings for COMSOL simulation

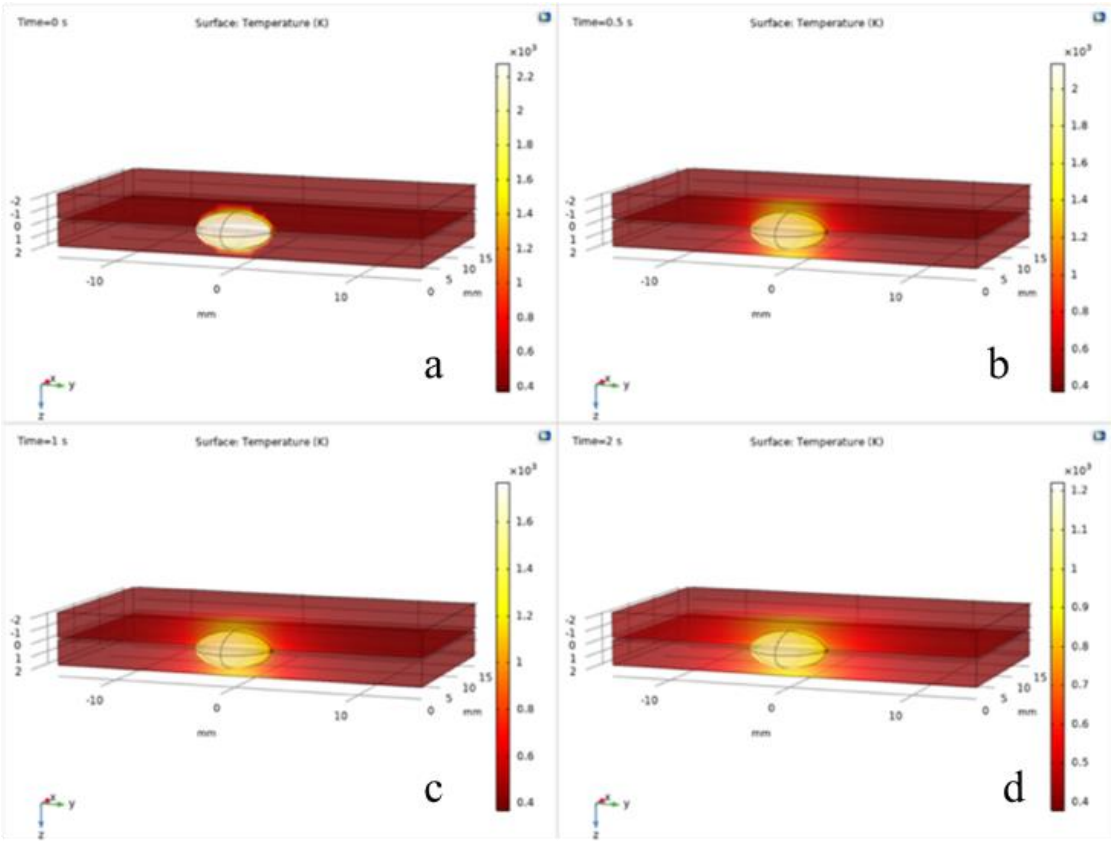

Figure 11 Temperature gradient of 0s (a), 0.5s (b), 1s (c), 2s (d) during RSW process

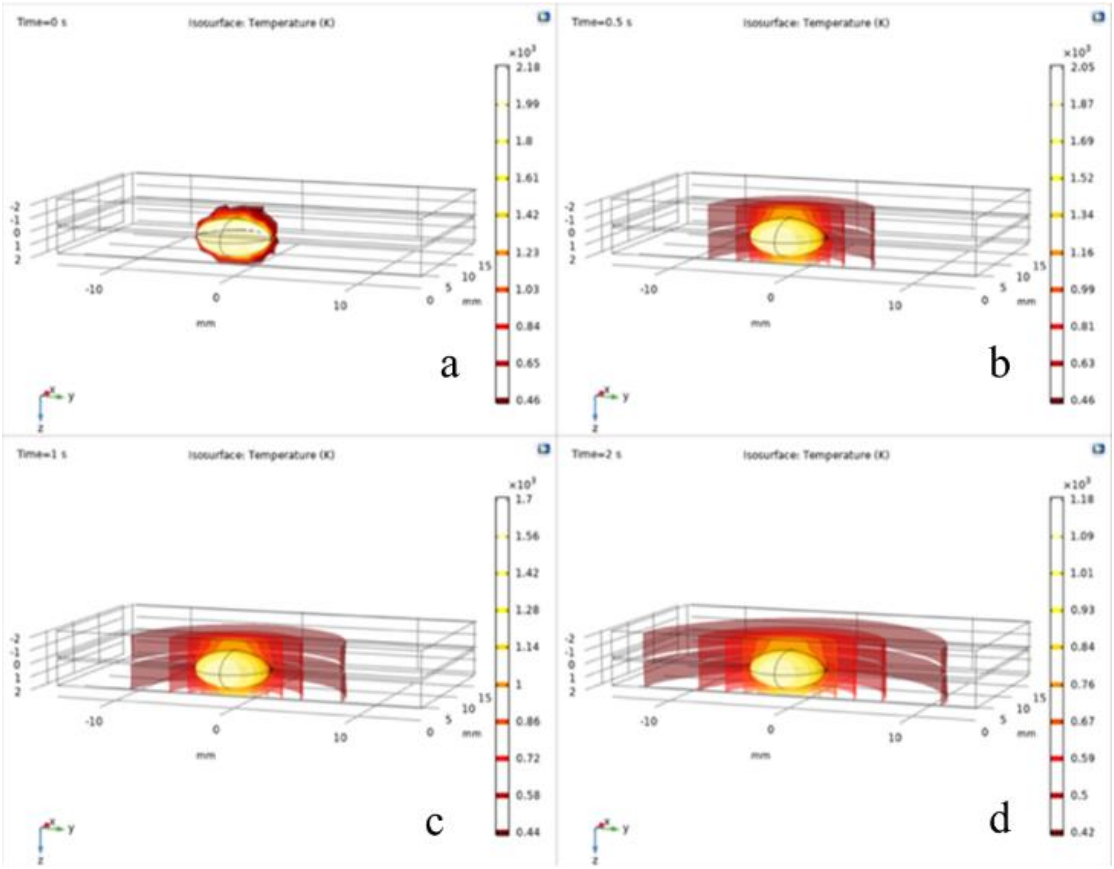

Figure 12 Isothermal contour of 0s (a), 0.5s (b), 1s (c), 2s (d) during RSW process

COMSOL Multiphysics Modeling of Binder Jet Printing

To simulate the sintering process of binder jet printed green part, heat transfer, fluid flow, and structural deformation modules have been utilized in COMSOL Multiphysics software. A380 aluminum alloy was selected as the material for the valve body 3D model. Heat capacity, thermal conductivity, and latent heat have been defined afterward to accommodate the numerical model. Heat Transfer and Fluid Flow modules were then utilized to simulate the sintering furnace condition based on the proposed melting and solidification mathematical models. General inward heat flux has been defined as emissivity flux based on the grade of the sintering furnace in the research lab to replicate the actual sintering tests. Volumetric shrinkage has been simulated through deformed geometry physics. By implementing a previous solution operator, the temperature solution at the previous time step was stored to determine whether volumetric shrinkage would occur. (Freels et al., 2007)

In order to monitor the temperature and geometric evolution of each channel more closely and efficiently during the sintering process, as shown in Figures 13 and 14, a simplified valve body with the approximate dimensions and fewer channels has been designed to replace the fully integrated model as a reference. An extra fine swept mesh with triangular face meshing method was generated, and a time-dependent study has been computed within a 2 hours range.

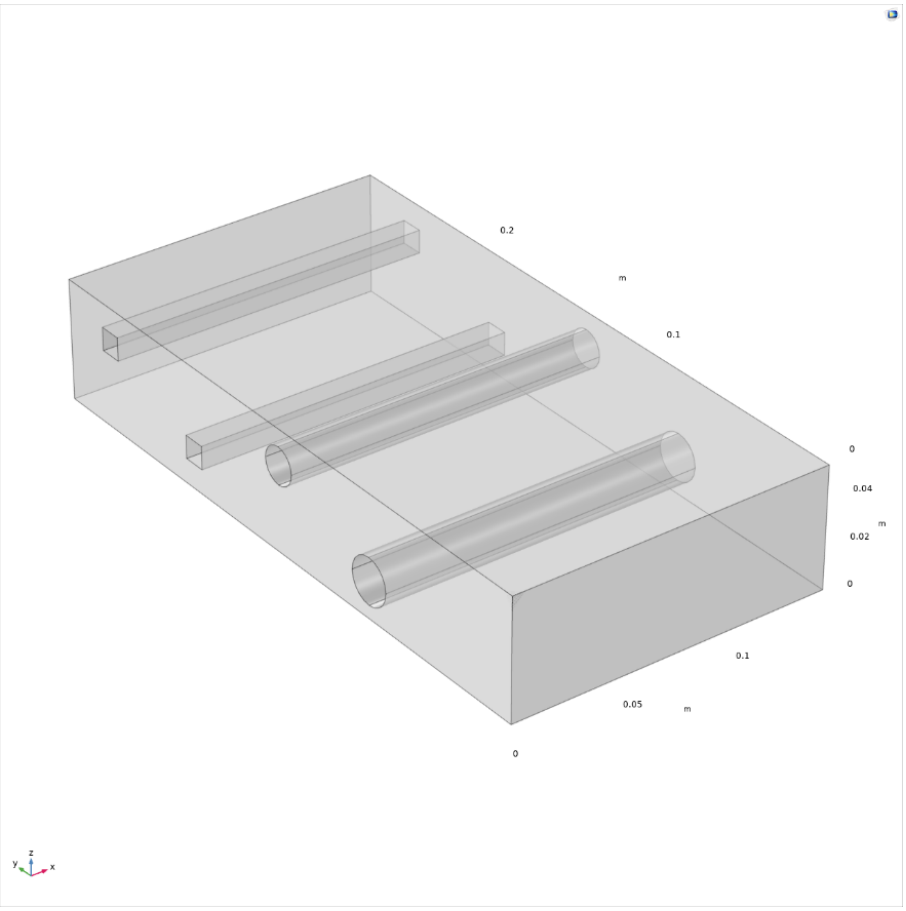

Figure 13 Geometric BJP green part model with channel cavities

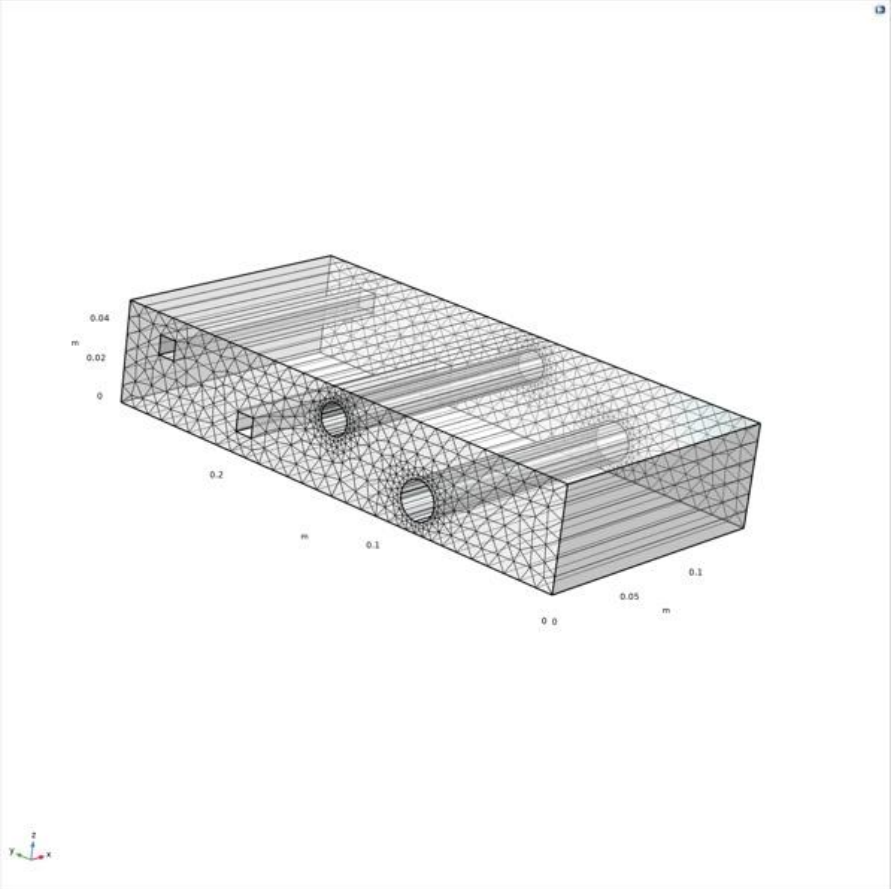

Figure 14 BJP green part model with channel cavities in extra fine swept mesh

Temperature gradient analysis were then performed as a time-dependent study. In the situation where the 313*161*60 mm A380 aluminum green part with two cylindrical channels and two rectangular channels is sintered in a 100W furnace for 0, 30, 100, 120 minutes, the simulation result is shown in Figure 15 as the surface temperature gradient. After sintering, the end dimensions of the BJP block are 272*140*52 mm. It can be calculated that the dimensional shrinkage rate is 13.3%.

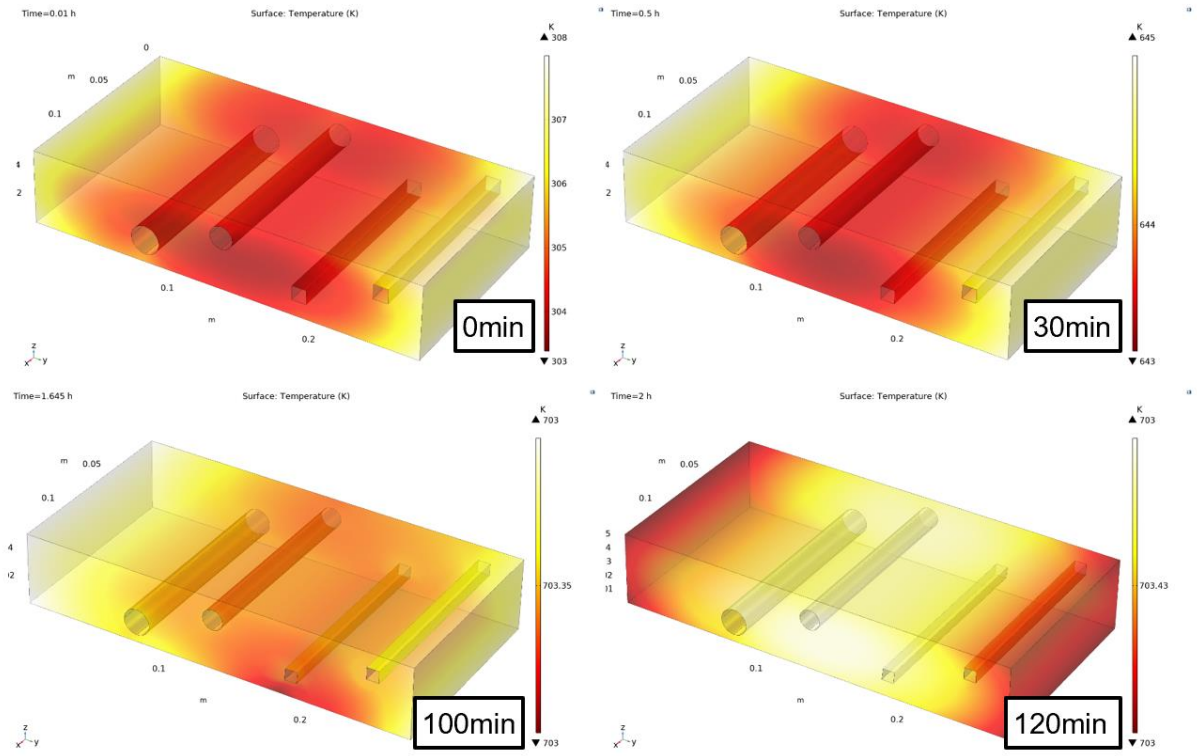

Figure 15 Temperature gradient of the designed BJP model after being sintered for (a) 0 min, (b) 30 min, (c) 100 min, and (d) 120 min.

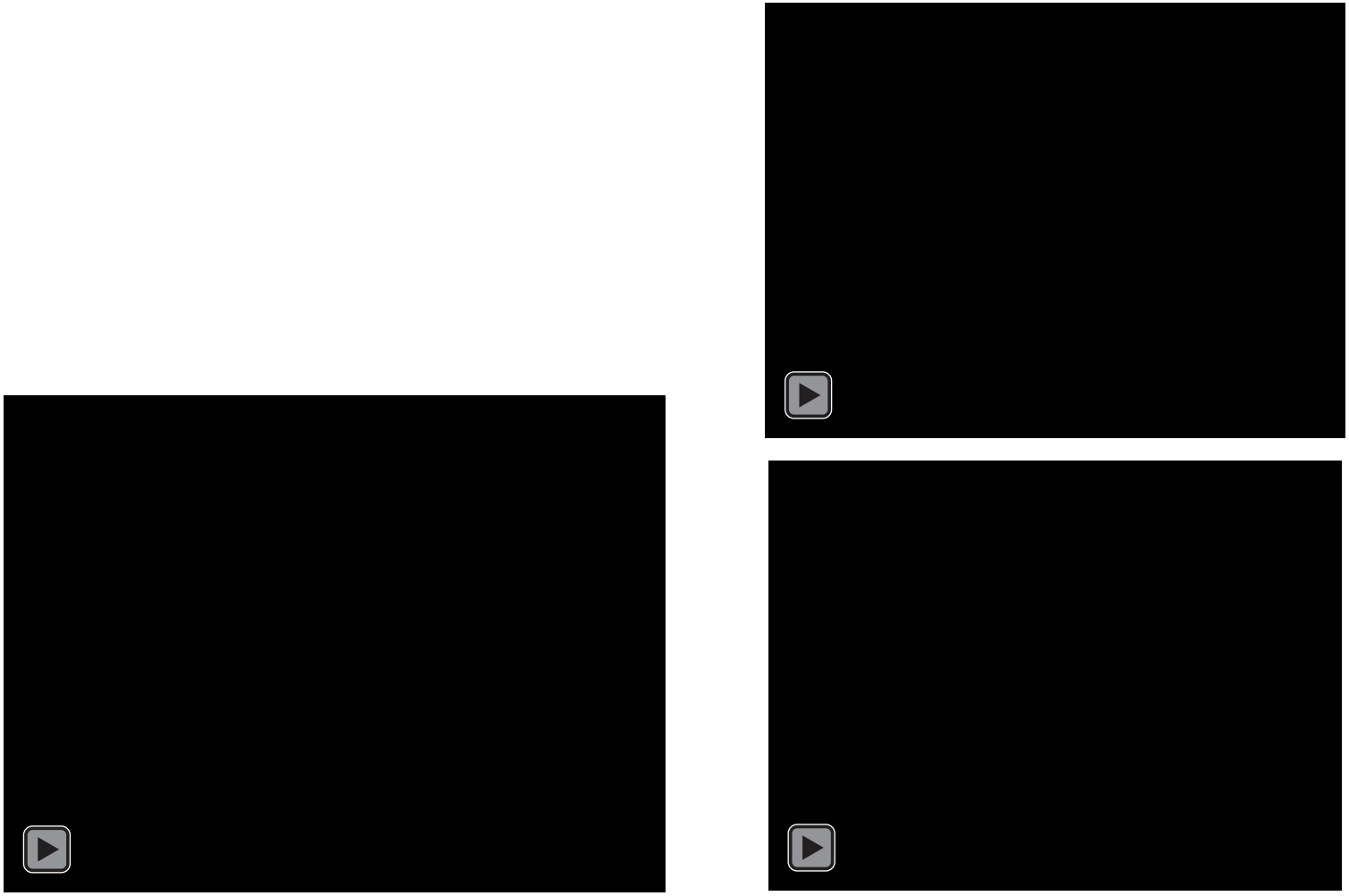

Figure 16 Animation depiction of the sintering process of the designed part with close up of the cylindrical and rectangular channels

Shrinkage simulation of more complex features is also necessary to assess the practicability of 3D printing aluminum alloy powder green part. As seen in the animation Figure 16, after 100 minutes of sintering at 700°F, compared to the cylindrical channel, the geometric shrinkage of the rectangular channel is unevenly distributed mainly around the edge as well as the surface near the cavity. The inconsistent densification of rectangular cavities during the melting process will likely lead to the deformed final product. Thus, implementing a cylindrical channel over the rectangular channel and designing more reinforcement around the cavity edges are recommended during the printing stage.

Utilizing the point graph from the 1D plot group, the temperature and the geometric evolution of a random point (Figure 17) during the sintering process were analyzed as shown in Figure 18 and Figure 19. In Figure 18, a positive quadratic relation between temperature and time correlates with the mathematical model of the melting process. The negative quadratic relation can be seen from Figure 19, where the dimension of the valve body shrinks at a higher rate as time passes and temperature increases, confirming the proposed model. From this analysis, geometric evolutions of valve body channels could be back-traced based on the plot data to obtain the green part volumetric design for binder jet printing.

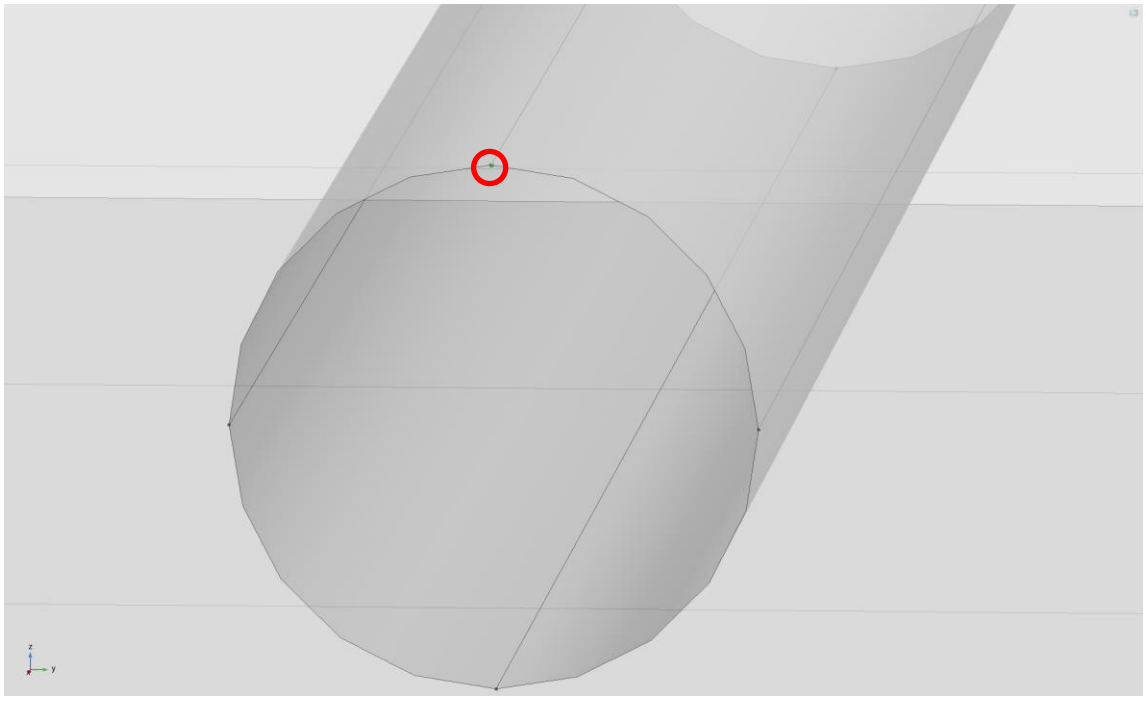

Figure 17 The point for analyzing the temperature and geometric evolution.

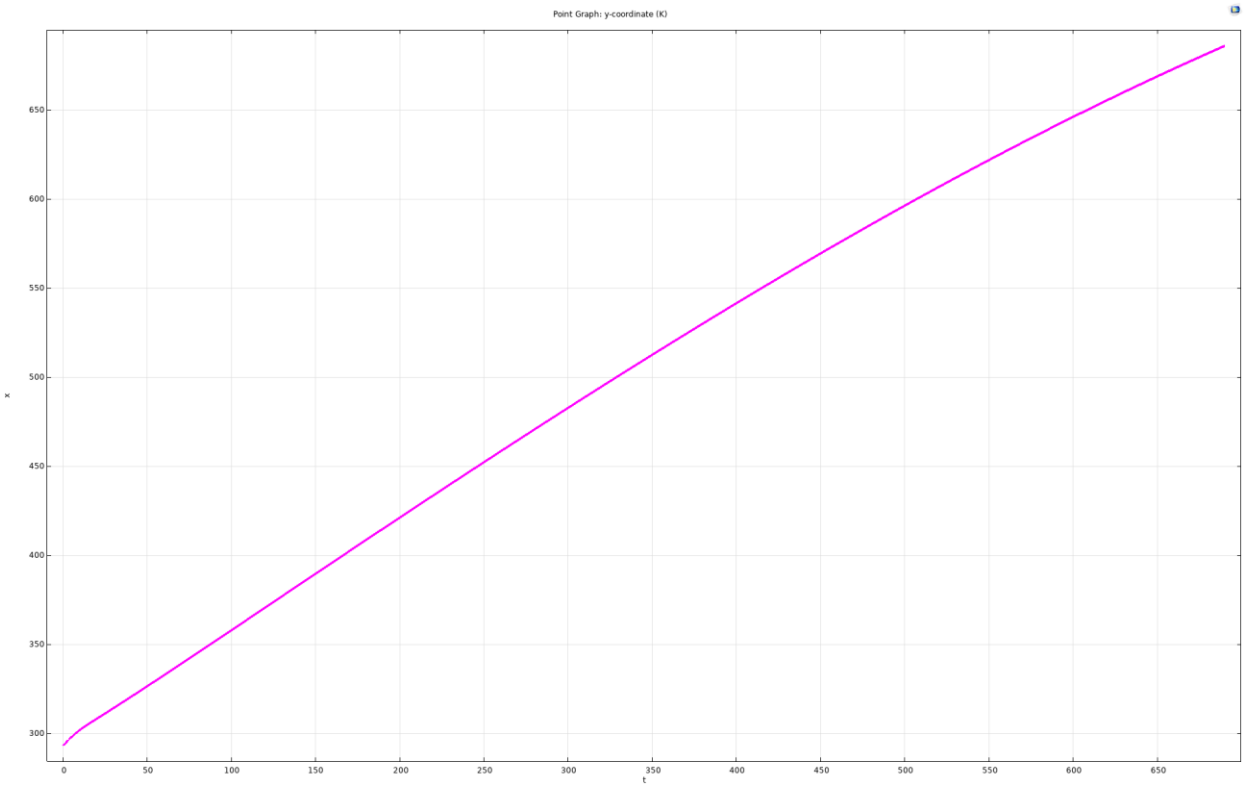

Figure 18 The 1D plot of temperature vs. time during sintering

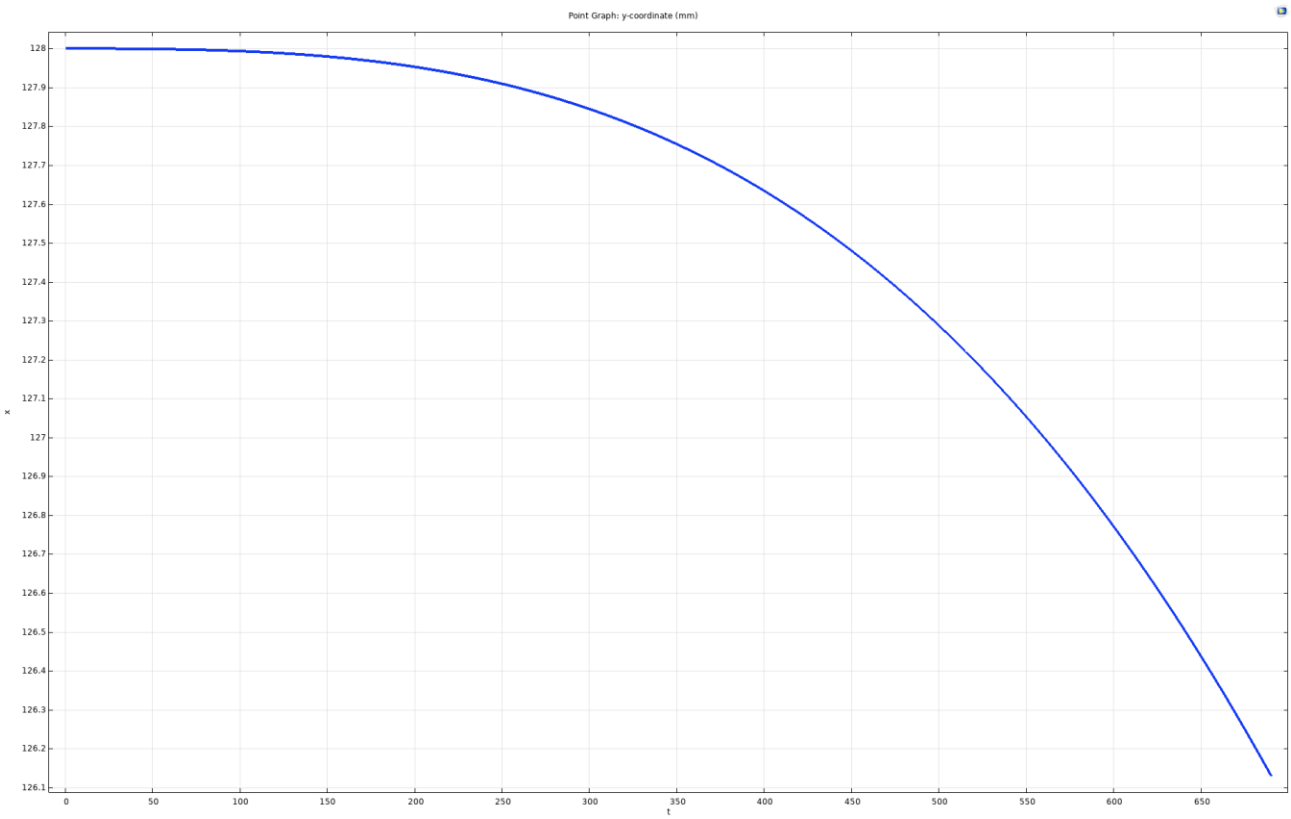

Figure 19 The 1D plot of y-coordinate vs. time during sintering

EXPERIMENTATION ANALYSIS OF BINDER JET PRINTING MANUFACTURING

The Journal of COMSOL Inc provided permission for me to publish this article titled COMSOL Implementation of Binder Jet Printing Densification Model in Automatic Valve System in this dissertation. Permission letters are attached in Appendix I. The following statement is endorsed by all authors: research structure and idea: Sun, R.; experiment and model execution: Sun, R.and Liu, H.; examination and conclusion of data: Sun, R, and Zhang, H.; paper outline formulation: Sun, R.; The dissertation manuscript has received approval from all mentioned authors.

The Journal of Journal of Multidisciplinary Engineering Science and Technology (JMEST) provided permission for me to publish this article titled Mathematical Modeling of Resistance Spot Welding in this dissertation. Permission letters are attached in Appendix I. The following statement is indorsed by all authors: research structure and idea: Zhang, H. and Das, M.; experiment and model execution: Sun, R., and Han, Q.; examination and conclusion of data: Sun, R, and Zhang, H.; paper outline formulation: Sun, R. and Zhang, H.; The dissertation manuscript has received approval from all mentioned authors.

Experimentation analysis has been performed where binder jet printed samples were evaluated based on printing density, sintering density, dimensional evolution during densification, and microstructure of the final products.

Binder Jet Samples Preparation

Sample Designing

The Binder jet printing process has been proposed in this research as an alternative to producing automobile valvebody in a more efficient and eco-friendly manner. Thus, samples block with channeling and bores have been designed to represent the valvebody and provide insight for future retrofit design. Designed samples for binder jet green parts are depicted in Figures 20 to 22. All dimensions are in millimeters. Figure 20 is the CAD drawing of sample #1 part, where one cylindrical channel is embedded in a solid block. Figure 21 is the CAD drawing of the sample #2 part, where two cylindrical channels are embedded in a solid block in parallel, with a minimum distance of 5 mm in-between. Figure 22 is the CAD drawing of the sample #3 part, where one cylindrical and one tubular channel are embedded in a solid block in parallel, with a minimum distance of 5 mm in between as well.

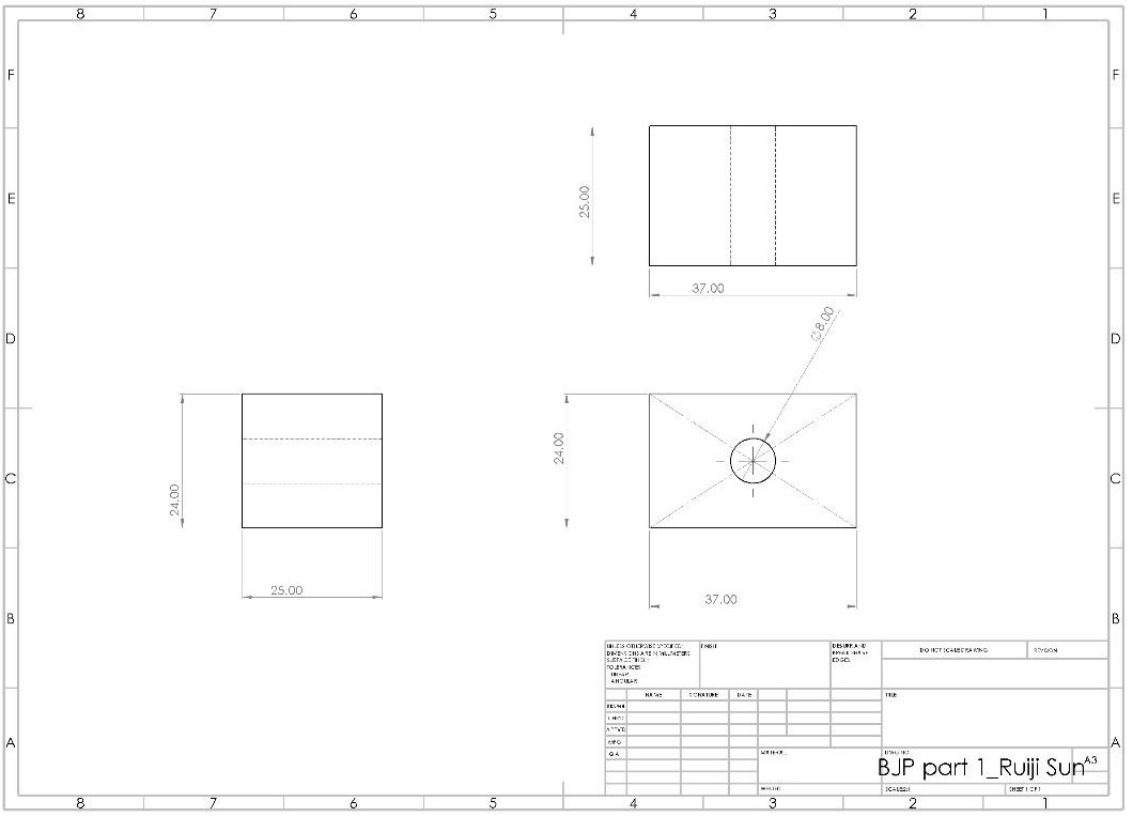

Figure 20 BJP green sample #1 CAD design

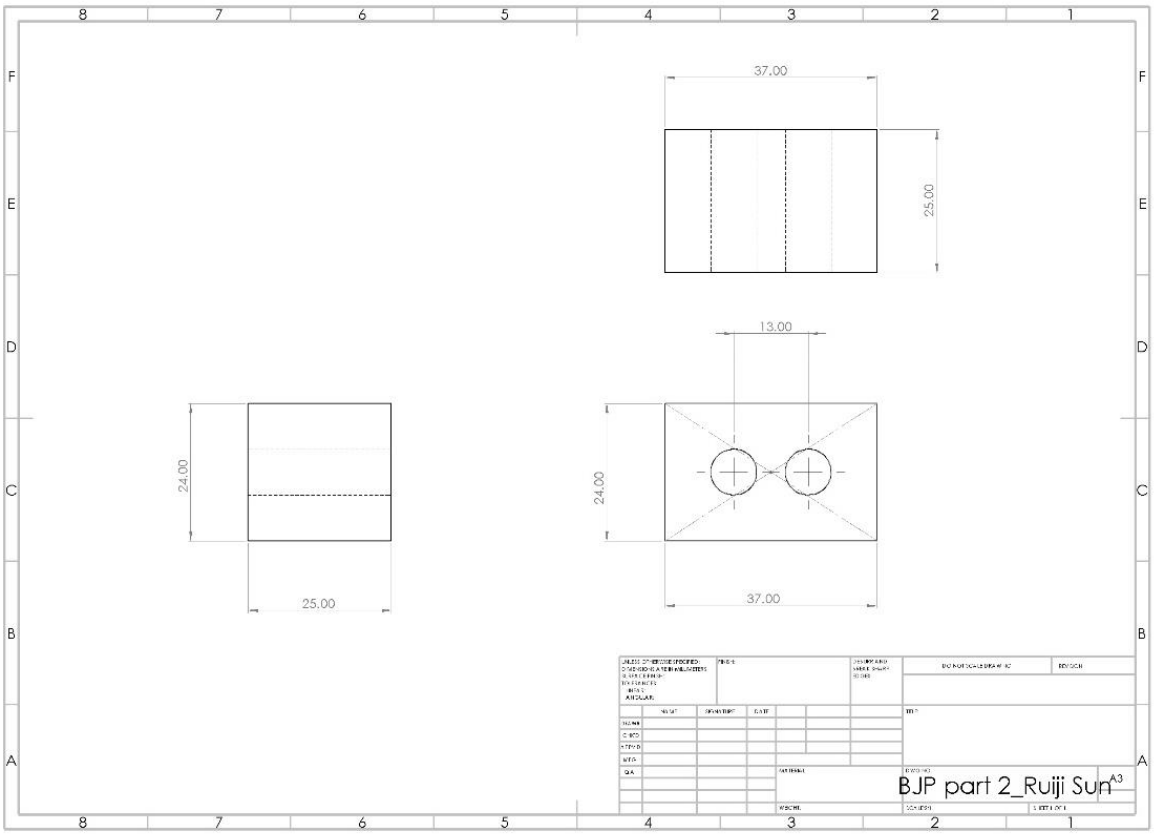

Figure 21 BJP green sample #2 CAD design

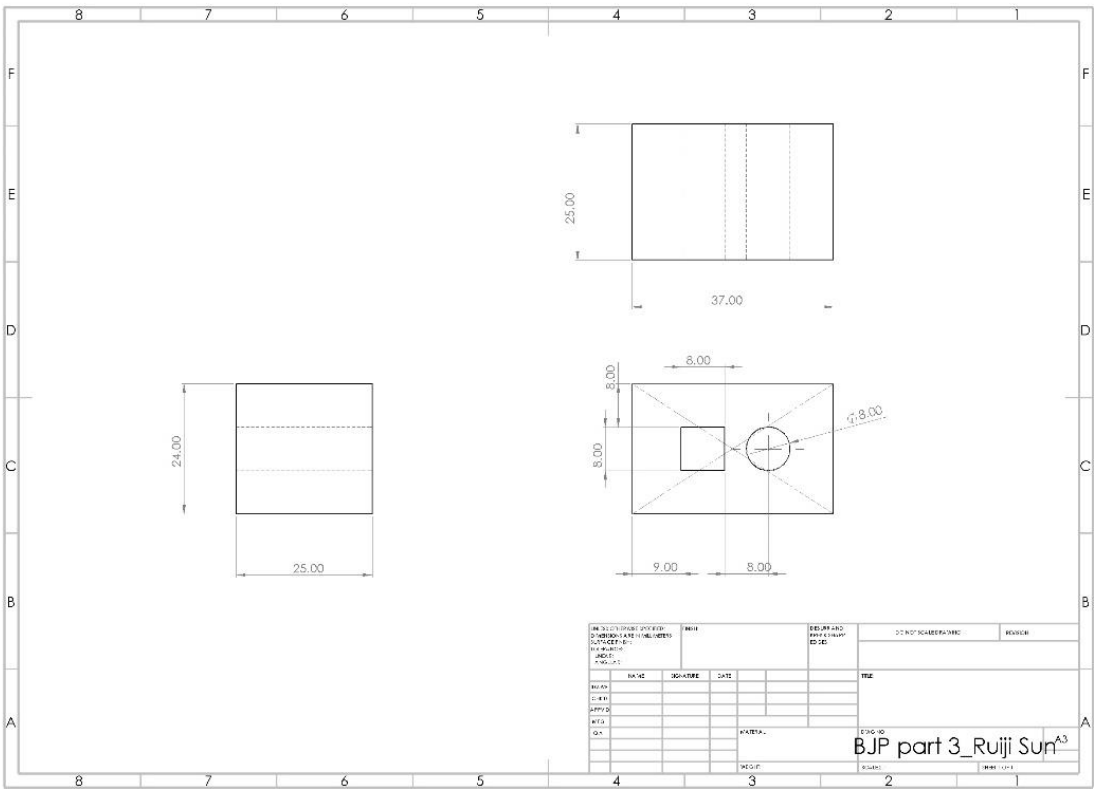

Figure 22 BJP green sample #3 CAD design

Sample Printing and Preparing

All designed samples are printed with binder jet printers in GE Additive facility based on the CAD designs. The printed samples then undergo a curing and sintering process in the same facility before being analyzed. Both the printing orientation and sinter orientation are in the z-axis of the through/shaped holes. Printing powder materials is 17-4 Stainless Steel. Material composition is depicted in Table 1. (*Stainless Steel - Grade 17-4 (UNS S17400)*, n.d.)

Table 1 Chemical composition of 17-4 stainless steel

Element	Fe	Cr	Ni	Cu	Mn	Si	Ta	Nb	Nb+Ta	C	P	S
Content %	73	15.0-17.5	3-5	3-5	1	1	0.45	0.45	0.15-0.45	0.07	0.04	0.03

The green density of the printed samples is 58%. After sintering, the final density is 98.5%. The sintered parts were then prepared for analysis without going through post-processing treatments of PH solution and age cycle.

To prepare for metallographic analysis, sintered samples were cut across with band saw in X, Y and Z-axis. The cross-section surfaces were then sanded with 60#, 180#, 400#, 600#, 800# sandpapers before being polished with 1% aluminum oxide polishing compound and then 0.1% aluminum oxide polishing compound. The polished part is then cleaned with water and ethanol solution before being air-dried. The polished surfaces are etched with the etchant solution that contained 30 ml of 67.2 vol% nitric acid and 3 ml of 37% hydrochloric acid. As shown in Figure 23, the observed sample is cut in the direction of the channel. The cross-section exposes the printing layers and the wall of the channels for a thorough inspection of the printing and sintering result. The etched samples were observed under ZEISS Axioscope 7 digital microscope. Dimensional measurements were performed prior to cutting the samples.

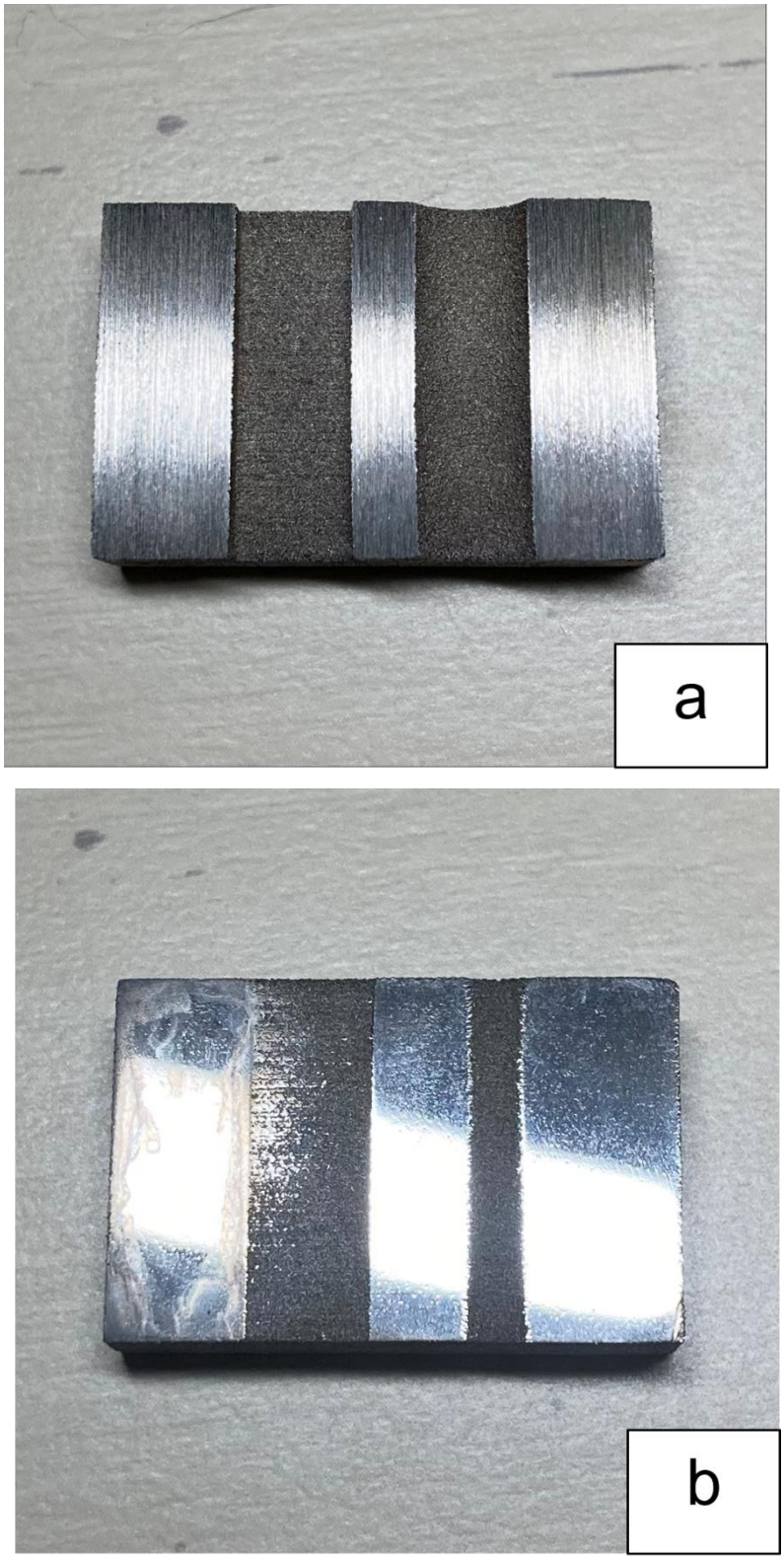

Figure 23 Cross-section photos of sintered part #3: (a) after cutting and sanding with #60 sandpaper; (b) after polishing and etching

Binder Jet Printed Samples Analysis Result

Geometric Analysis of Green and Sintered BJP Samples

One of the challenges in binder jet printing manufacturing lies in the erratic densification process, where dimensions of the green part change drastically depending on the sintering parameters, printing parameters, and metal powder properties. Thus, one of the critical studies for the BJP process is geometric analysis. As shown in Figure 24 and Figure 25, in this study, thirty-nine samples were analyzed in the geometric study of shrinkage rate. Among the samples, eighteen samples are green, and twenty-one samples are sintered. Eighteen green samples consist of six sample #1s, six sample #2s, and six sample #3s. Twenty-one sintered samples consist of seven sample #1s, seven sample #2s, and seven sample #3s.

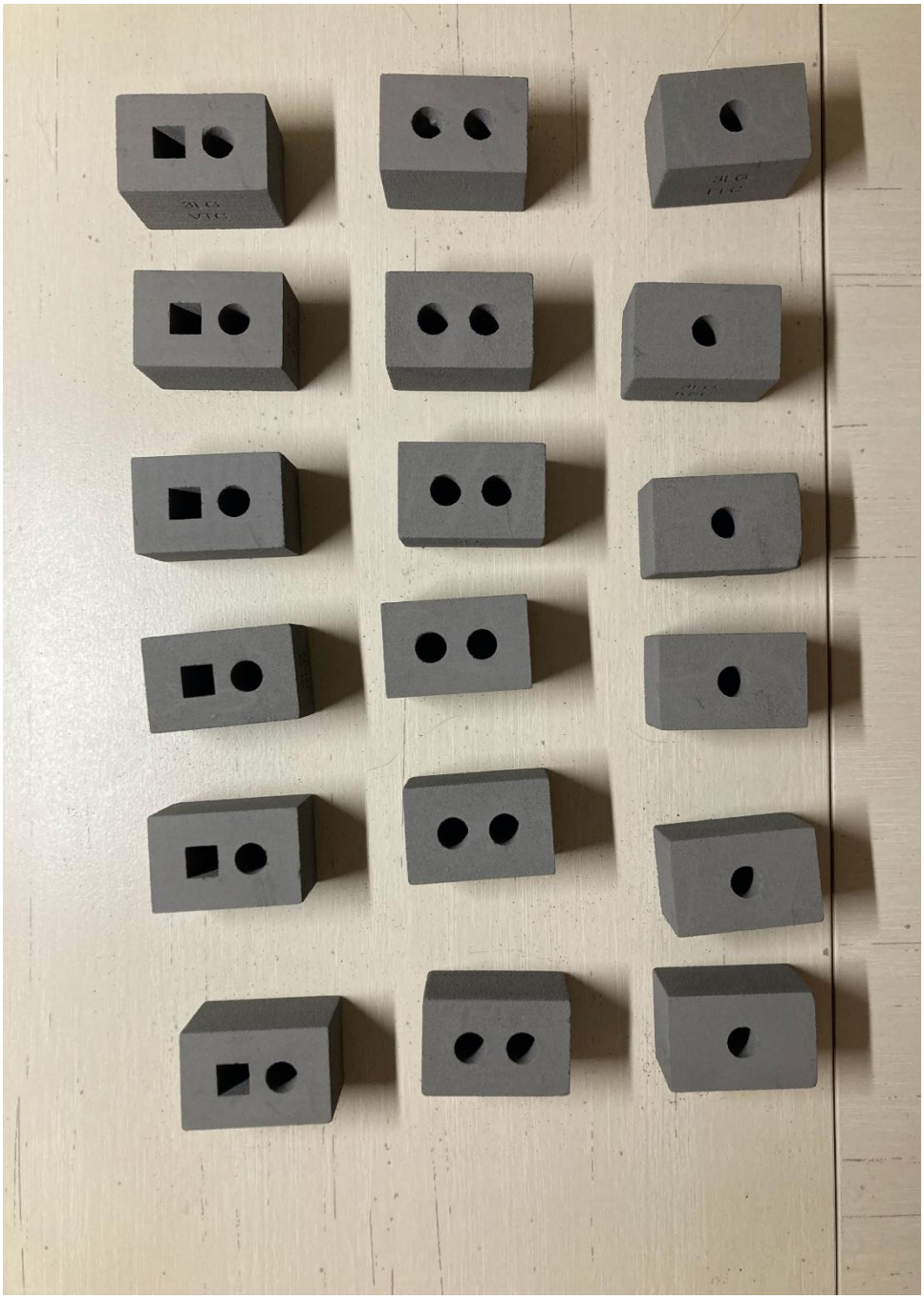

Figure 24 Binder jet printed green samples after curing

Figure 25 Binder jet printed samples after sintering

All samples shown in Figures 24 and 25 have gone through measurement in the designated dimensions to calculate the dimensional shrinkage rate during sintering. As explained previously, during sintering, binder evaporation and metal powder fusion lead to drastic densification of the green part. As seen from Figures 26 to 29, all dimensions shrink down after the sintering process is completed. The geometric between the green and sintered samples can be visibly distinguished.

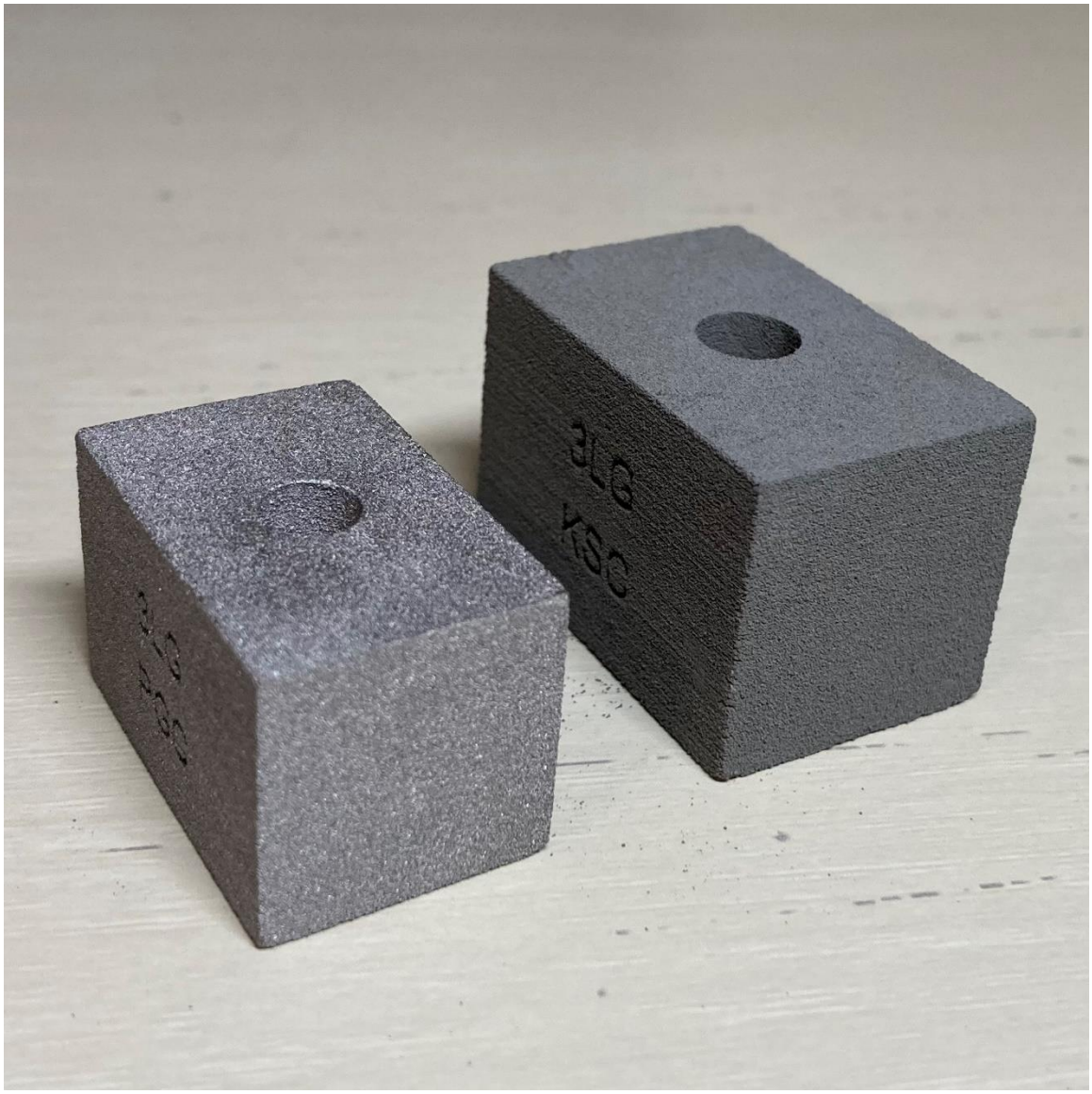

Figure 26 Green (right) and sintered (left) samples of part #1

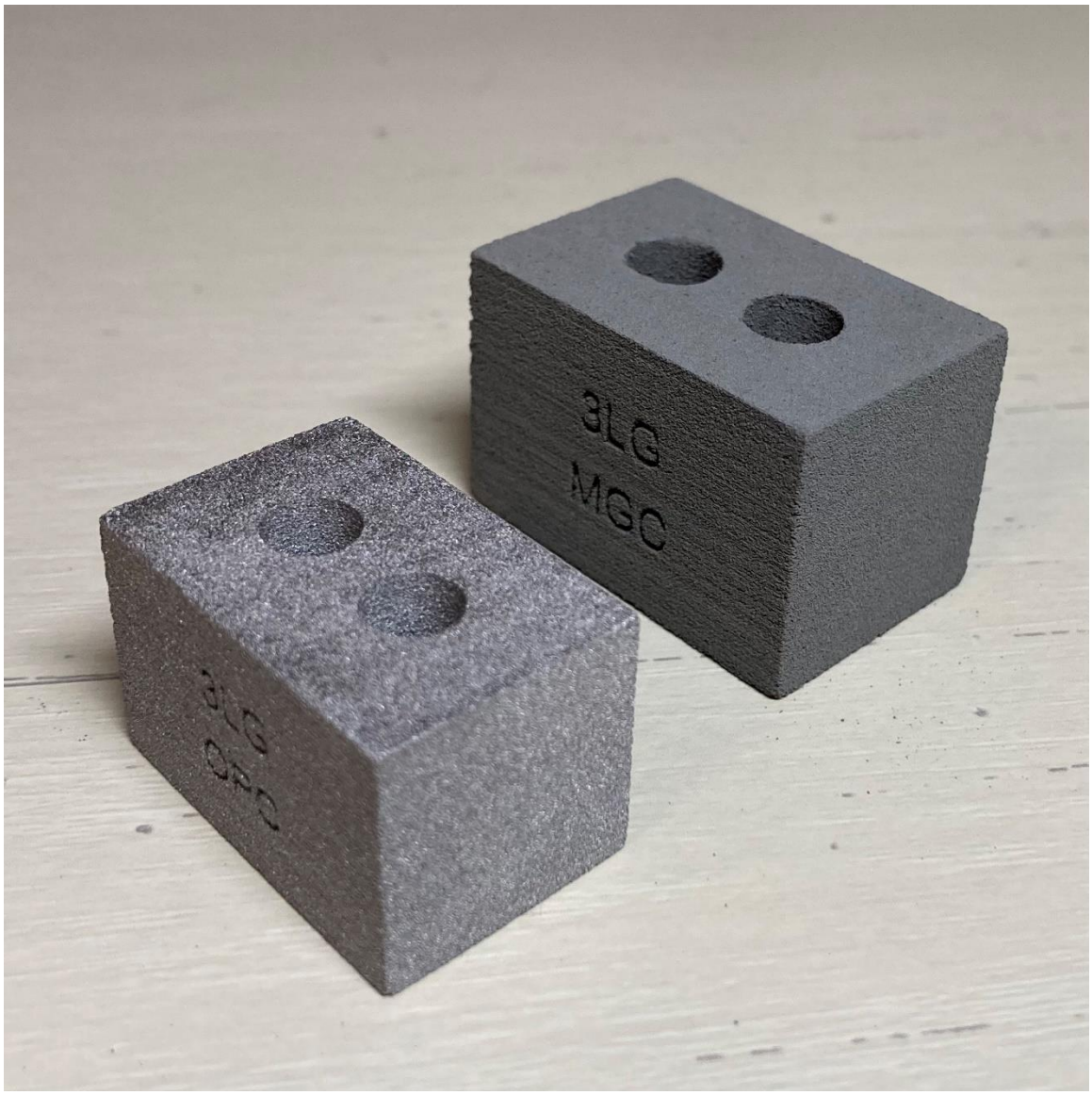

Figure 27 Green (right) and sintered (left) samples of part #2

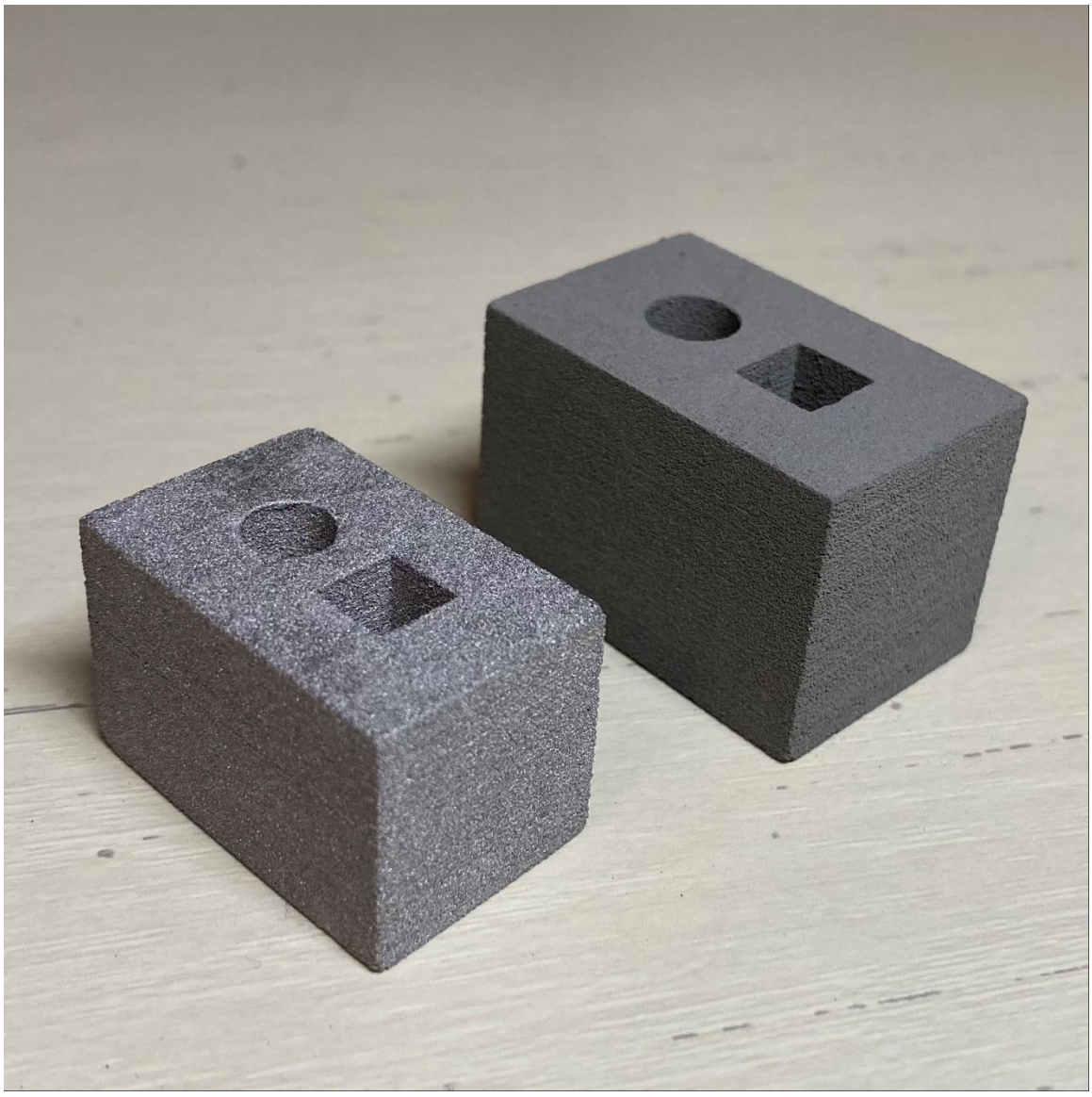

Figure 28 Green (right) and sintered (left) samples of part #3

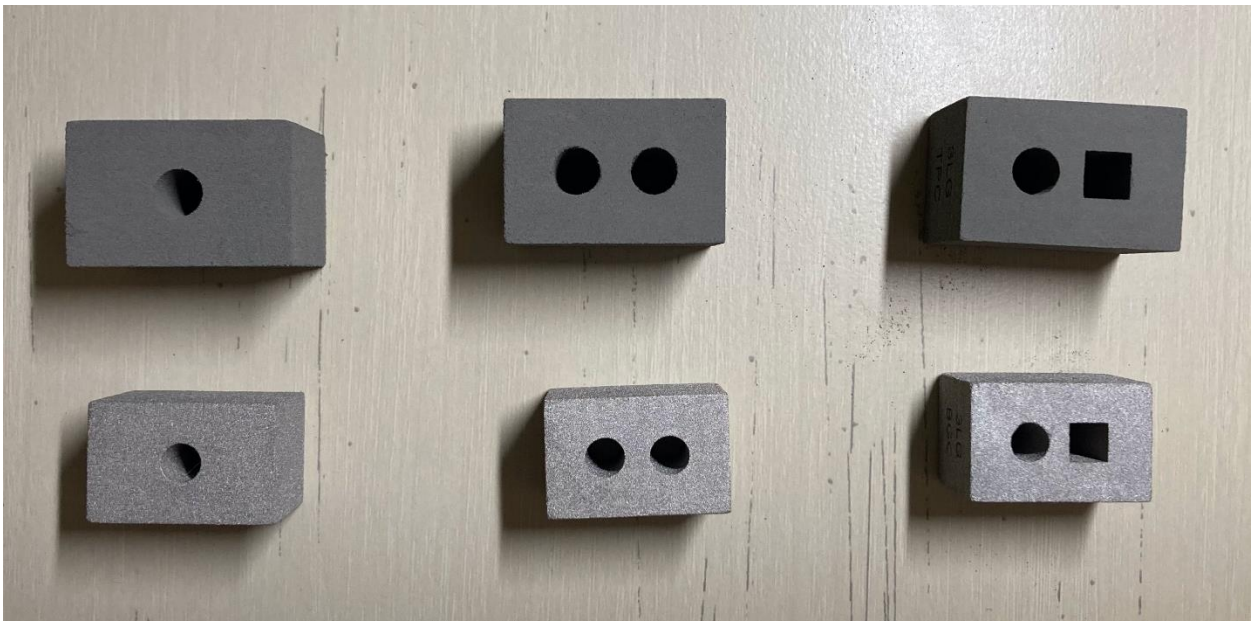

Figure 29 Green and sintered samples top view: green (top left) and sintered (bottom left) samples of part #1; green (top middle) and sintered (bottom middle) samples of part #2; green (top right) and sintered (bottom right) samples of part #3.

All sintered samples are analyzed without post-processing and surface treatment. As seen, the binder jet printed part has a distinctive rough surface finish. Compare to die casting, BJP requires post-machining if a high glossy surface finish is required or angle tolerance is low.

In order to analyze the geometric evolution difference among different features of the sample, all products from Figure 24 and Figure 25 were analyzed. Based on Figures 30 to 32, each dimension that needs measuring has been given a symbol. Measurement of each dimension on the same type of samples was recorded and averaged. Standard deviation and printing error have also been calculated to analyze the consistency and printing quality of the technique. Statistical analysis was performed on each axis of the sample block and the dimensions of the channels. Dimensional change of part #1, part #2, and part #3 between green and sintered samples are shown in Table 2 to 4, where SD stands for standard deviation and shrinkage rate is calculated based on Equation 48:

$$Dimensional\ shrinkage\ rate = \frac{(green\ mean - sintered\ mean)}{green\ mean} \times 100\% \qquad (48)$$

The dimension shrinkage rates of the x, y, z-axis, and channel diameter of all three designs were then analyzed in Figure 33, where the contrast between the axis and part design can be visually assessed.

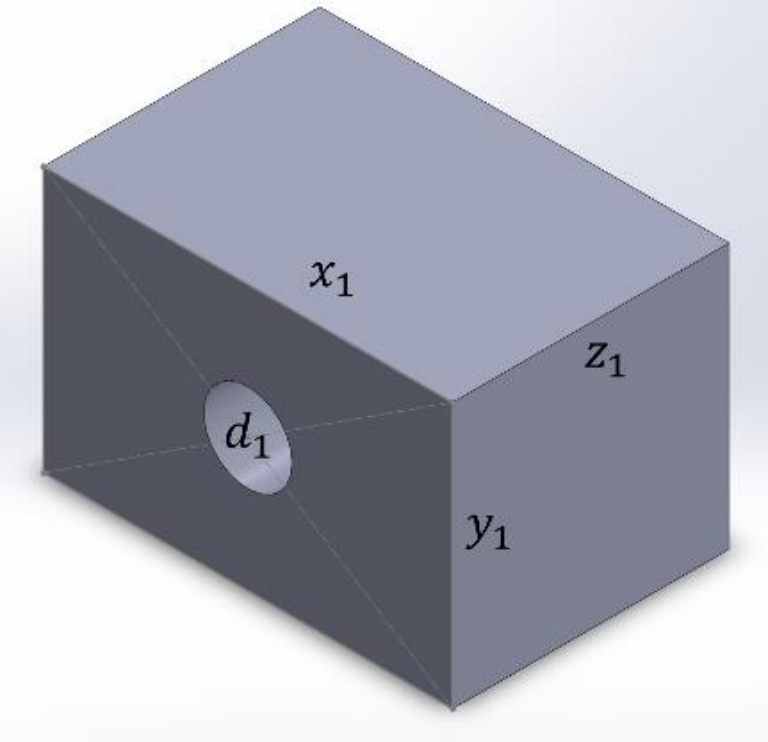

Figure 30 Geometric feature representation for sample design #1

Table 2 Dimensional analysis of BJP sample #1

		Green sample			Sintered samples				
	Designed Value (mm)	Green mean (mm)	Printing error	Green SD	Sintered mean (mm)	Sintered SD	Dimensional shrinkage rate (DSR)	Mean of SDR	SD of DSR
x1	37.00	37.18	0.49%	0.028	31.76	0.142	14.58%	16.20%	0.017
y1	24.00	24.14	0.58%	0.021	20.63	0.114	14.53%		
z1	25.00	24.95	-0.19%	0.090	20.55	0.067	17.66%		
d1	8.00	7.77	-2.92%	0.034	6.37	0.112	18.04%		

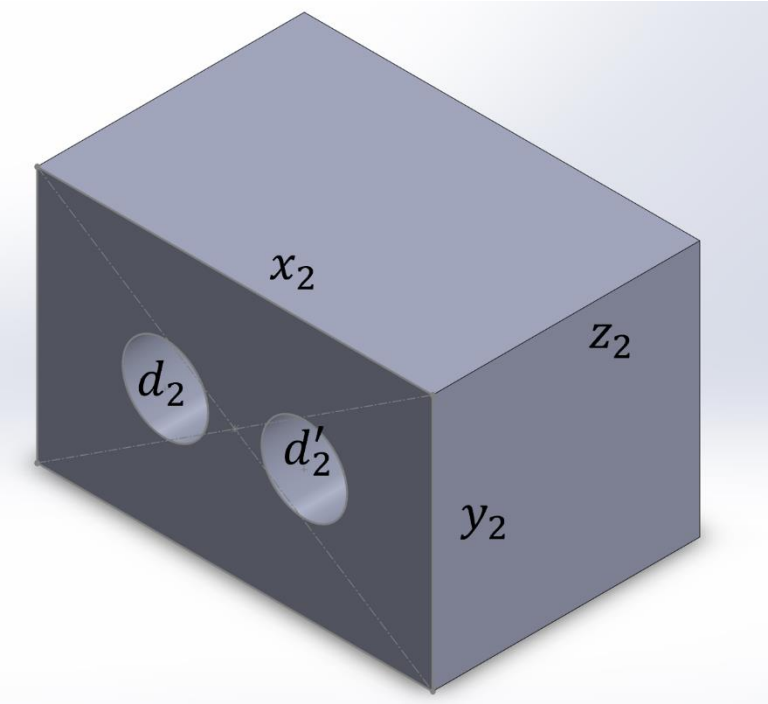

Figure 31 Geometric feature representation for sample design #2

Table 3 Dimensional analysis of BJP part #2

		Green sample			Sintered samples				
	Designed value (mm)	Green mean (mm)	Printing error	Green SD	Sintered mean (mm)	Sintered SD	Dimensional Shrinkage rate (DSR)	Mean of SDR	SD of DSR
x2	37.00	37.19	0.52%	0.057	31.71	0.140	14.74%	16.65%	0.015
y2	24.00	24.18	0.76%	0.035	20.54	0.037	15.06%		
z2	25.00	24.92	-0.32%	0.089	20.49	0.079	17.78%		
d2	8.00	7.69	-3.85%	0.100	6.37	0.133	17.22%		
d2'	8.00	7.71	-3.67%	0.080	6.28	0.084	18.46%		

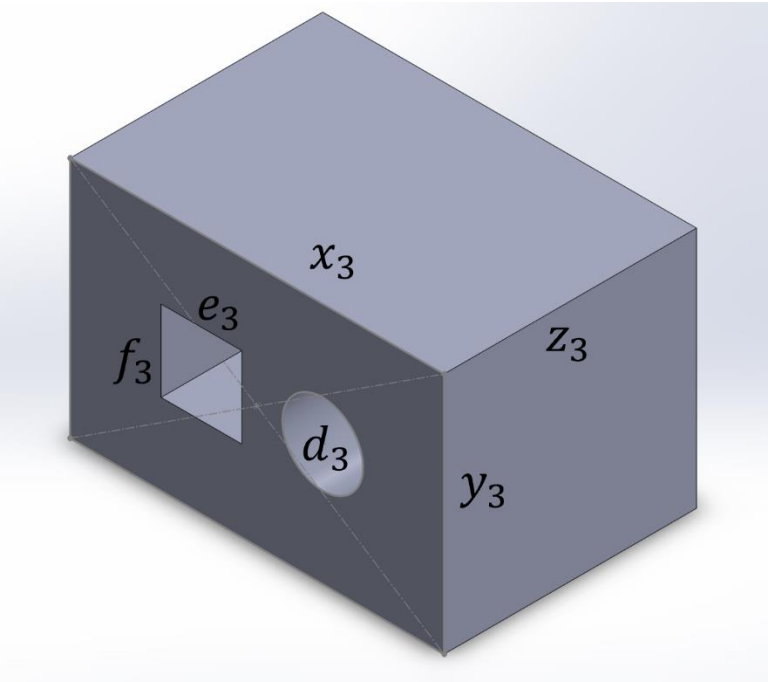

Figure 32 Geometric feature representation for sample design #3

Table 4 Dimensional analysis of BJP part #3

		Green samples			Sintered samples				
	Designed value (mm)	Green mean (mm)	Printing error	Green SD	Sintered mean (mm)	Sintered SD	Dimensional shrinkage rate (DSR)	Mean of SDR	SD of DSR
x3	37.00	37.20	0.53%	0.055	31.61	0.122	15.02%	16.52%	0.013
y3	24.00	24.25	1.02%	0.081	20.48	0.096	15.53%		
z3	25.00	24.83	-0.69%	0.092	20.46	0.094	17.60%		
d3	8.00	7.55	-5.63%	0.129	6.41	0.115	15.14%		
e3	8.00	7.87	-1.67%	0.054	6.44	0.119	18.14%		
f3	8.00	7.87	-1.60%	0.027	6.48	0.115	17.72%		

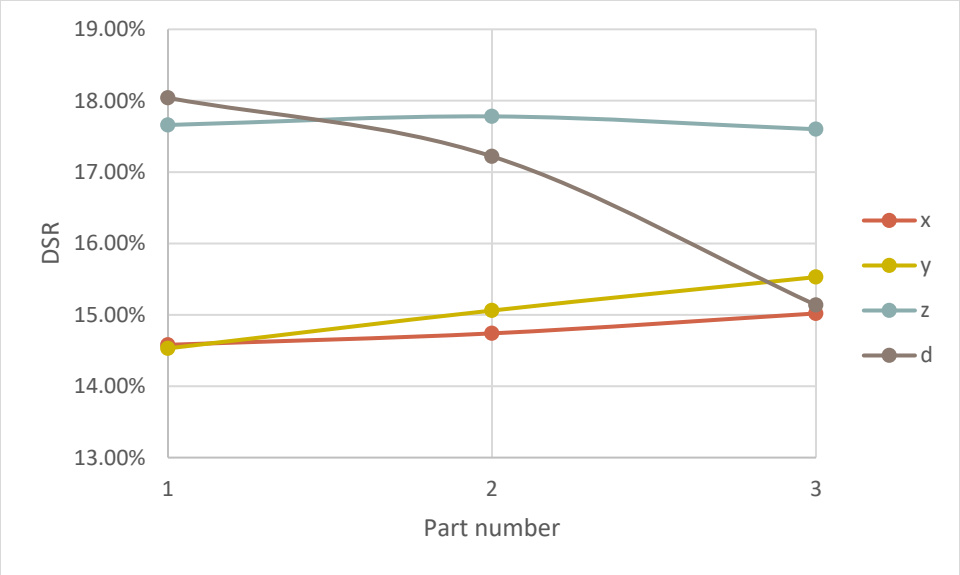

Figure 33 Scattered plot of shrinkage rates of x, y, z, d dimensions of part #1, part #2, and part #3

From the above statistical analysis of shrinkage rate, the total dimensional shrinkage rate is 16.46%, which is a close approximation of the COMSOL simulation. Binder jet printing tolerance is relatively low, so are the green part dimensions standard deviation, which ensures good repeatability between productions. In contrast, sintered samples yield mostly higher standard deviations in all dimensions, which indicates a higher tolerance in the prediction of sintered dimensions.

As indicated in Figure 33, the dimensional shrinkage rate varies drastically among different orientations. X and Y axis, which are perpendicular to the building and sintering direction, have similar and relatively lower shrinkage rates. Comparably, Z-axis yields a much higher shrinkage rate for all three sample designs.

Several reasons are causing a higher z-axis shrinkage. During the printing stage, controlling error for binder nozzles can lead to uneven and excess binder distribution, causing parting or seperation of the building layers, leading to higher shrinkage of the z-axis during sintering the binder begins to evaporate. Gravity will also affect inducing a higher densification rate during sintering. As the parts are printed and sintered through holes direction, the gravity of the higher layers will create higher stress to lower layers during sintering. Thus, the gravitational force can lead to a higher densification rate in the z-axis.

However, as the printing and sintering direction are both in the z-axis, it is uncertain whether excess binder deposition or gravitation is the leading cause for the higher z-axis densification rate. More discussion on the issue will be needed in order to conclude.

Metallurgical Analysis of Green and Sintered BJP samples

As shown in Figures 34 and 35, one of the significant features for 3D printed samples is the inconsistency between bottom printing layers and top printing layers. Due to the nature of technology, the printing topography greatly affects the final product quality, both cosmetically and metallurgically, on both micro and macro scales. As the bottom layer of the part is under constant pressure, the bottom surface of the green part has a higher risk of crumble. After sintering, it can be seen from Figure 35 that the bottom layer has more blunt edges and angles than the top surface. On the micro-scale, constant pressure and stress on the bottom section of the printed part also lead to a high potential of stress-induced defects.

Another defect commonly seen on binder jet printed samples are the peeling and cracking of surface layers. During the printing process, uneven distribution of the binder can lead to failure of fusion during the sintering stage. As shown in Figure 36, a small section at the top edge of the cylindrical channel is missing. A similar defect is common around complex printing features and sharp angles.

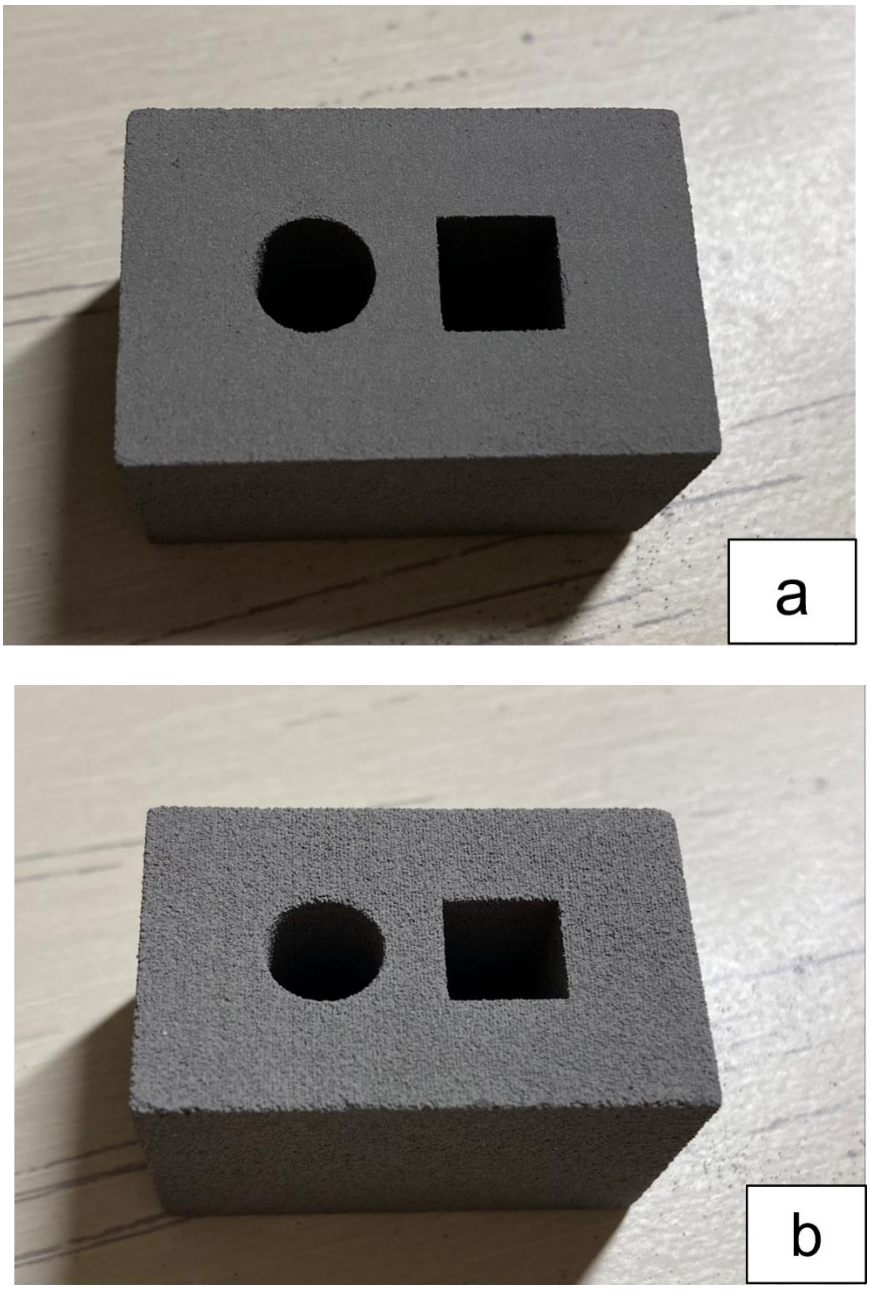

Figure 34 (a) top surface of the green sample #3; (b) bottom surface of the green sample #3

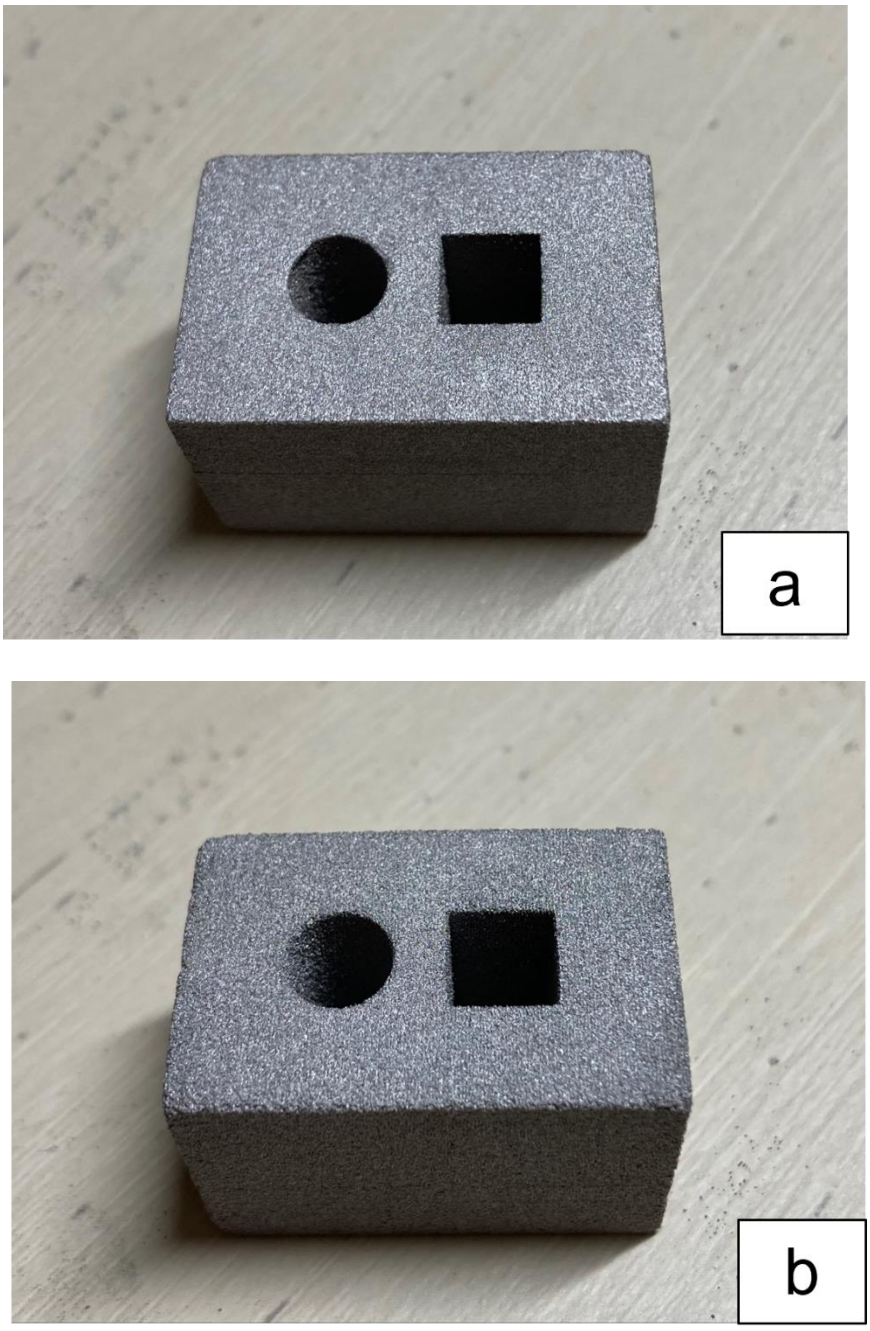

Figure 35 (a) top surface of the sintered sample #3; (b) bottom surface of the sintered sample #3

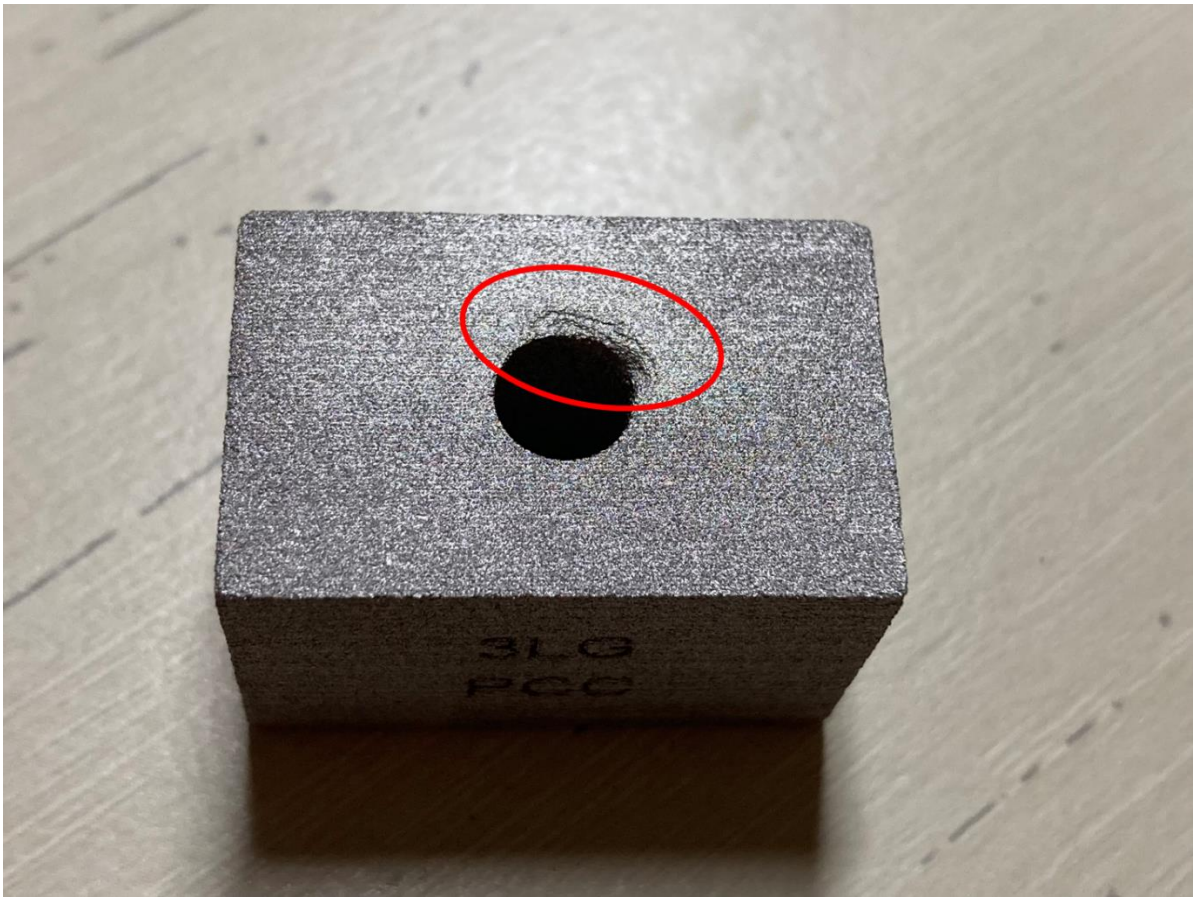

Figure 36 Peeling top layers of the sintered sample #1

Prepared 17-4 SS samples were examined under ZEISS Axioscope 7 digital microscope to analyze the metallurgical microstructure of the binder jet printed samples. As seen in Figures 37 to 42, micrographic pictures are taken to for analysis on the microstructure of the 17-4 stainless steel sintered samples.

Figure 37 is the 3.15X micrograph of the unetched sample. Throughout the sample surface, porosity can be clearly seen, which is likely formed during the printing or sintering processes. During printing, powder segregation can occur as a result of uneven binder ejection or print head shifting. Separated clusters or layers will group during the sintering stage, creating distortion and increasing the chance of peeling or erosion. In another scenario, porosity and uneven grain growth can occur because of irregular heat distribution during sintering. As the binder evaporates unevenly, metal powder of different layers failed to fuse and form a homogenous structure, leading to voids

among clusters of grains, resulting in agglomeration, which leads to anisotropic properties in the final product.

Figure 38 are etched sintered samples in 31.5X magnification. As seen, the majority of the grains are around $50\mu m$ and distributed homogenously throughout the sample. Porosities, which are the black dots on the micrographs, have an average size of over $20\mu m$. There is no specific pattern in the distribution of the porosity, which indicates the consistent printing and binder distribution pattern.

Figure 39 depicted the transparent phase distribution and precipitation feature of the sample. The bright base is the Martensite matrix. Around the Martensite matrix, δ Ferrite is dispersed evenly. Inside the bright matrix, small particle inclusions of less than $5\mu m$ are distributed, including the precipitation of Si and Cu composition. However, most precipitation sizes are top large to contribute to the hardening effect.

Figure 40 (a) is the low magnification picture of the cross-section of the bottom layers of the sample, while Figure 40 (b) demonstrates the cross-section of the top layer. In comparison, it can be seen that precipitation on top layers grows to a much larger size than the bottom, while the grain sizes remain relatively similar. Uneven distribution of sintering temperature and solute in the matrix can both lead to an overgrowth of precipitations. Larger precipitations have a lower chance of obstructing dislocations in the grain, which lowers the strength of the materials. It is also worth noting that top layers have a slightly higher concentration of porosity, which could be caused by air pores floating to the top during the sintering stage.

Figure 41 and Figure 42 are demonstrations of another feature of the microstructure. As seen in red circles in Figure 41 and Figure 42, grain twining can be observed. Both Figures are taken at the bottom layers of the samples, where a high-stress concentration from gravity can occur and induce the twinning phenomenon. During sintering, fast conduction of the bottom layer with the sintering furnace leads to volatile rheological behaviors of the mushy zone, leading to a higher chance of twinning. Thus unique structure occurs as a result of atom displacement. For stainless steel, martensite transformation can induce twining as well, leading to a higher hardness.

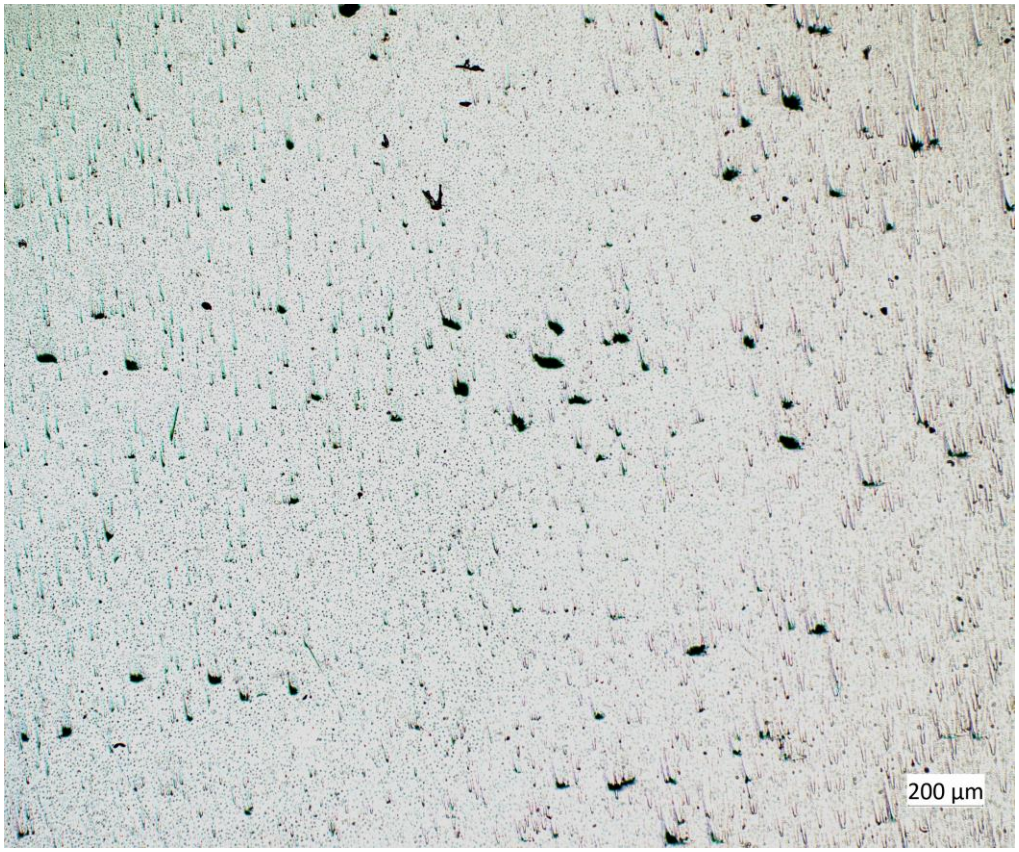

Figure 37 Metallographic pictures of unetched sintered binder jet sample, demonstrating porosity (3.15X)

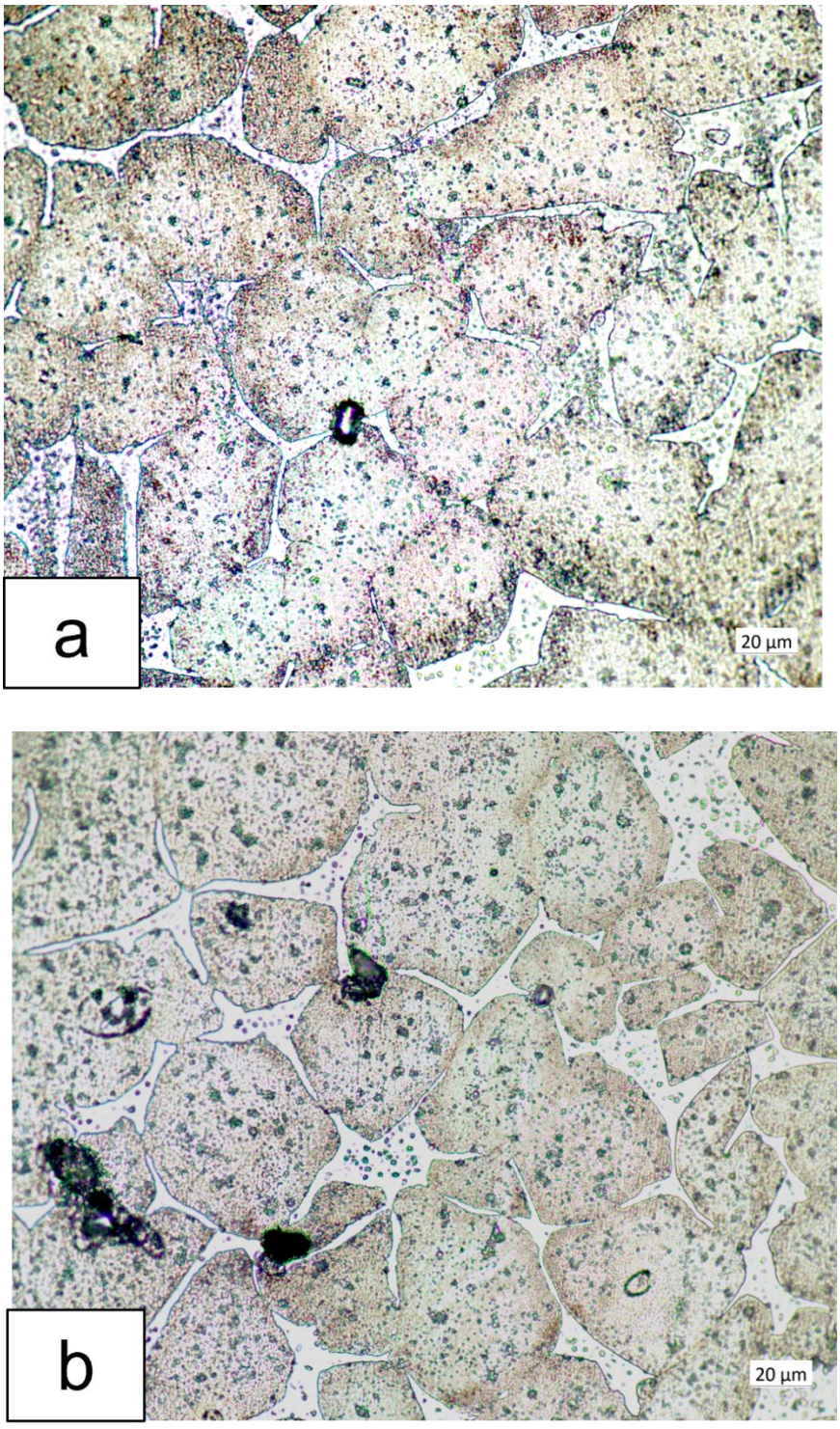

Figure 38 Metallographic pictures of etched sintered binder jet sample (31.5X), demonstrating porosities among grains

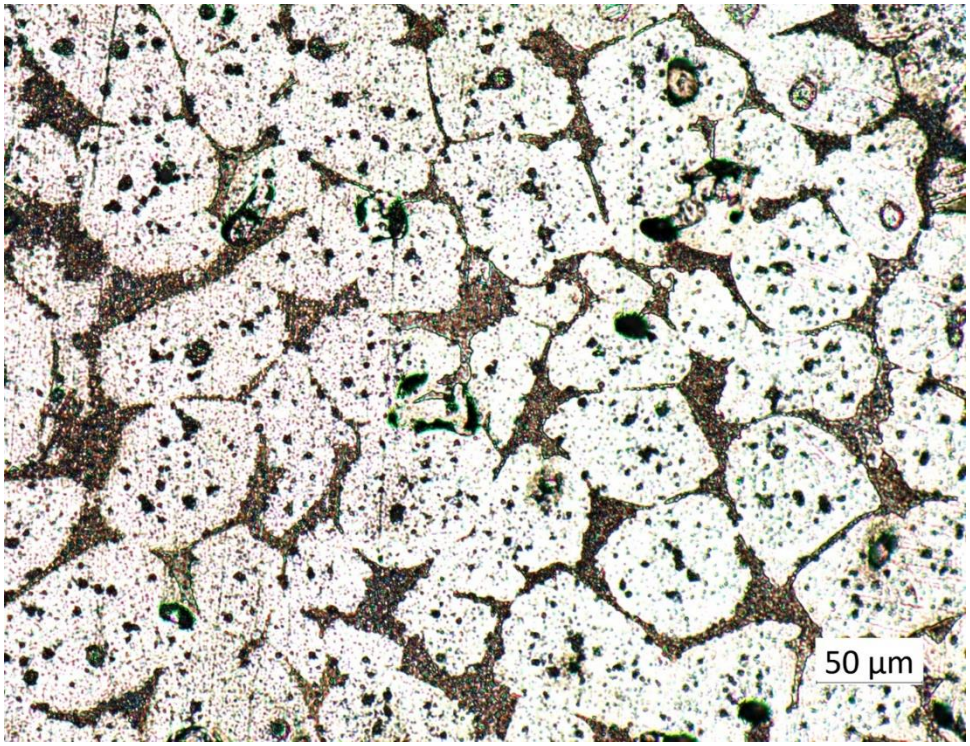

Figure 39 Metallographic pictures of etched sintered binder jet sample (12.6X), demonstrating phase distribution

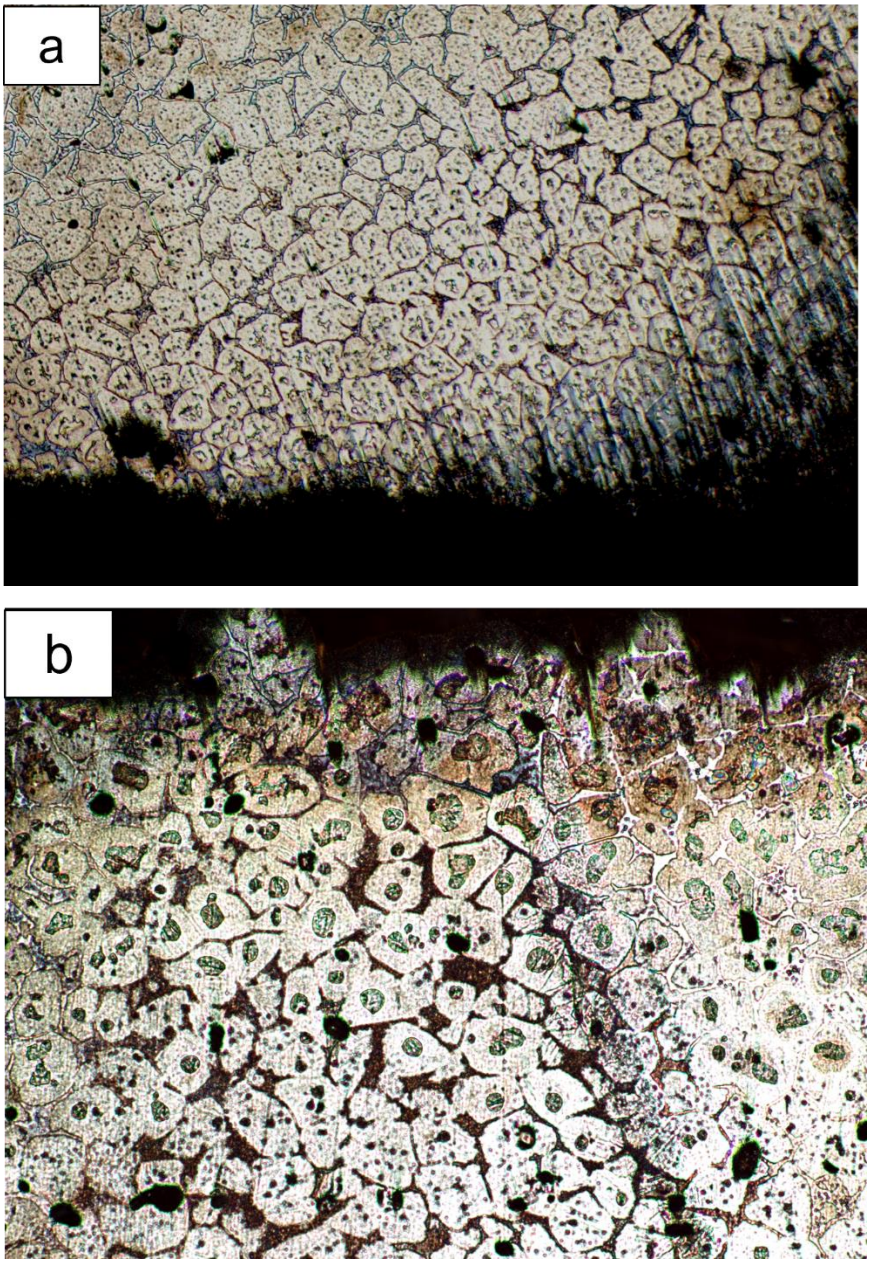

Figure 40 (a) Cross-section of the bottom printing layer of the etched BJP sample, 6.3X; (b) Cross-section of the top printing layer of the etched BJP sample, 6.3X

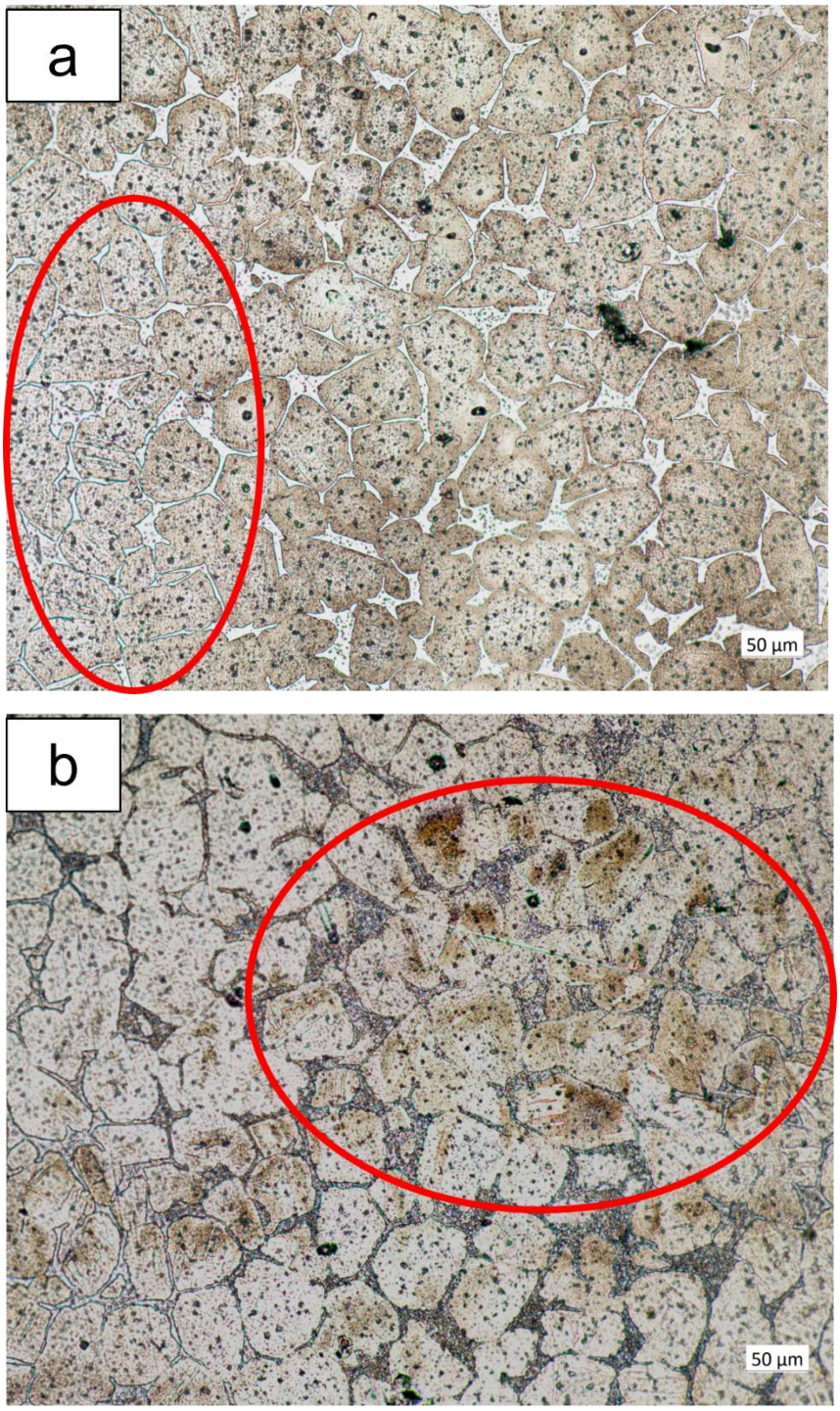

Figure 41 Twining observed at the bottom layers of the sintered sample (a) 12.6X; (b) 12.6X

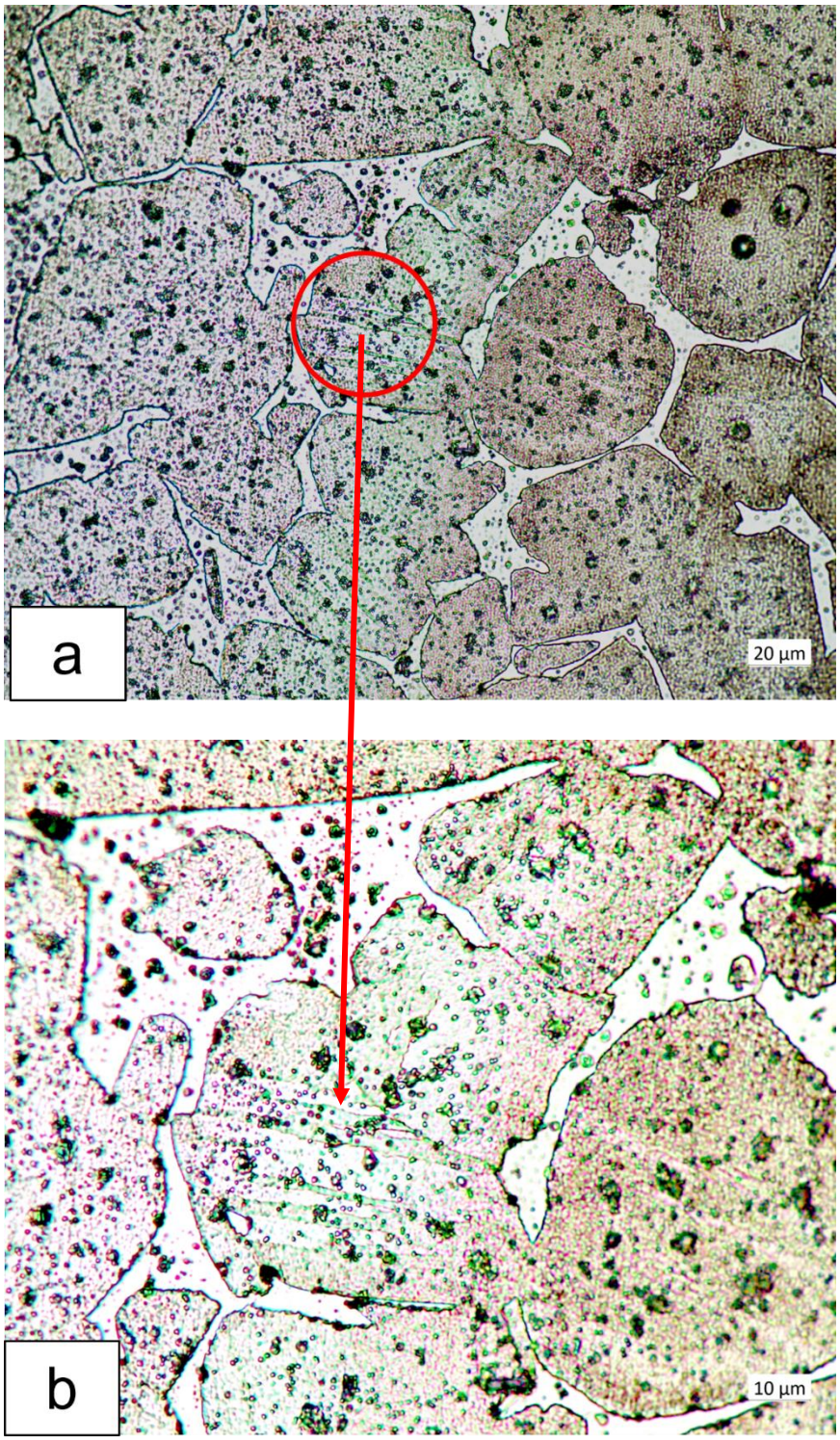

Figure 42 Twining at the bottom layers of the sintered sample (a) 31.5X; (b) 63X

CONCLUSION AND DISCUSSION

With the emergence of novel materials processing techniques and computation abilities, mathematical and simulative modelings have become an inseparable branch of materials science. In this dissertation, Related empirical and simulative modeling studies on RSW and BJP have been thoroughly reviewed. Rheological characterization has been implemented to analyze heat transfer, fluid flow, and geometric evolution of phase-changing binary alloy manufacturing processes. Mathematical models have been established to analyze the melting and solidification of metal processing techniques, resistance spot welding, and binder jet printing. The proposed model has been calculated and analyzed through COMSOL Multiphysics to evaluate the resistance spot welding geometric and thermal evolution and the green part sintering process from binder jet printing. The model can be implemented into RSW and BJP application on various alloys in order to monitor the melting and solidification process by the transient temperature profile based on the processing and thermal properties of the alloy to achieve the optimum production result, which offers an effective measure for lean manufacturing in the mass production automobile industries. Python case study and COMSOL dimensional analysis of the printed samples has confirmed the mathematical models.

Further experimental analysis of binder jet printed products also provided further verification on the densification rate of the sintering process of binder jet printed products. The metallurgical analysis also lends insights to the emerging manufacturing technique, reaffirming the validity of utilizing the process as an alternative to conventional metal processing methods.

The dissertation established an empirical-mathmatical-simulative system for analyzing alloy liquid-solid phase-changing processes. As industrial manufacturing progresses to a more intelligent and lean approach to production, comprehensive modelings will bound to be implemented for higher production efficiency and eco-friendliness.

APPENDIX I

Permission letters from prior publication journals:

1. Letter from JMEST regarding permission to publish the article:

SUN, R., Yu, W., Zhang, H. H., Das, M., & Han, Q. (2019). Mathematical Modeling of Resistance Spot Welding. Journal of Multidisciplinary Engineering Science and Technology (JMEST), 6(March), 2458–9403. Retrieved from www.jmest.org

From: JMEST JOURNAL <jmest.journal@gmail.com>
Sent: Wednesday, July 14, 2021 14:20
To: Ruiji Sun <sun613@purdue.edu>
Subject: Re

Dear Dr. Sun,

Thanks for contacting us.

In placing author's thesis please display the following message in a prominent place on the dissertation: In reference to JMEST copyrighted material which is used with permission in this thesis, the JMEST does not endorse any of [university/educational entity's name goes here]'s products or services. Internal or personal use of this material is permitted.

Hope this will help you.

Once you need anything else, please do not hesitate to contact us.

Kind Regards,
Editor-in-Chief, JMEST

2. Letter from COMSOL Inc regarding permission to publish the article:

SUN, R., LIU, H., & ZHANG, H. H. (2020). COMSOL Implementation of Binder Jet Printing Densification Model in Automatic Valve System. comsol.jp

From: Jessica Allendorf <Jessica.Allendorf@comsol.com>
Sent: Wednesday, July 14, 2021 14:32
To: Ruiji Sun <sun613@purdue.edu>
Cc: Dixita Patel <Dixita.Patel@comsol.com>
Subject: RE: Permission request to publish the journal in my PhD dissertation

Hi Ruiji,

COMSOL allows for your work to be published in other publications; we do not have any restrictions on this when presenting at the conference. Do you need us to remove your work from our website in order to publish in your dissertation? If so please let me know and we can certainly help out with that.

Best,
Jessica

Jessica Allendorf
COMSOL, Inc.
100 District Avenue
Burlington, MA 01803 USA
Phone: (781) 273-3322
Email: jessica.allendorf@comsol.com

APPENDIX II

Python modeling code on the solidification of resistance sport welding

```
# Import Modules
import math
import numpy
import matplotlib
from matplotlib import pyplot as plt
from matplotlib import animation
from scipy.optimize import fsolve
matplotlib.rcParams['agg.path.chunksize'] = 10000

# Greeting
print("Hello!")

# Material Inputs
Co=float(input("Nominal composition (mass %): "))
ml=float(input("Linear Liquidus slope (K/mass %): "))
ms=float(input("Linear Solidus slope (K/mass %): "))
cps=float(input("Specific Heat (J/(kgK)): "))
RhoS=float(input("Density (kg/(m^3)): "))
Lf=float(input("Specific Latent Heat of Fusion (J/kg): "))
Tf=float(input("Freezing Point of Solvent (Degrees Celsius): "))
ks=float(input("Thermal Conductivity of Solid (W/(mK)): "))
ko=float(input("Segregation Coefficient: "))
Le=float(input("Lewis Number (alpha/Dl): "))

#Initial Condition Data
Ti=float(input("Initial Superheat Temperature (Degrees Celsius): "))
To=float(input("Electrode Hold Temperature (Degress Celsisus): "))
```

```
#Geometric Inputs
L=float(input("Sheet Thickness (m): "))
rns=float(input("Relative Weld Nugget Size (0<=RNS<0.7): "))
print("\n")

#Thermodynamic Constants
alpha=ks/(RhoS*cps)
Ste=cps*(Ti-To)/Lf
Tl=(ml*Co)+Tf
Ts=(ms*Co)+Tf

#Lambda
sodd=cps*(Ti-Tf)/(Lf*math.sqrt(math.pi))
def f(lam):
   y=lam*math.erf(lam**2)*math.exp(lam)-sodd
   return y
lam=fsolve(f,1)
lam=lam[0]

#tweld
tweld=((rns*L/(lam))**2)*(1/alpha)
print("Welding Time (s): ",tweld)
print("\n")

#Phi
thetaf=(Tf-To)/(Ti-To)
def f(phi):
      A1=(thetaf-
(math.erf(phi)*(1+((math.sqrt(math.pi)/Ste)*phi*math.exp(phi**2)*math.erfc(phi)))))
      A2=1-(math.sqrt(math.pi*Le)*(1-
ko)*phi*math.exp(Le*phi**2)*math.erfc(phi*math.sqrt(Le)))
```

```
        y=(A1*A2)-(ml*Co/(To-Ti))
        return y
phi=fsolve(f,0)
phi=phi[0]

#Thetastar
thetastar=math.erf(phi)*(1+((math.sqrt(math.pi)/Ste)*phi*math.exp(phi**2)*math.erfc(phi)))
Tstar=(Ti-To)*thetastar+To

#Solidification time
tf=((L**2)/alpha)*(((1-((1-rns)))/(2*phi)))**2
print("Solidification Time (s): ",tf)
print("Total RSW time (s): ",tf+tweld)
print("\n")

#Time Array
time_step=0.001*tf
times=numpy.arange(time_step,tf+time_step,time_step)

#Plotting and Animation
"""
Matplotlib Animation Example

author: Jake Vanderplas
email: vanderplas@astro.washington.edu
website: http://jakevdp.github.com
license: BSD
Please feel free to use and modify this, but keep the above information. Thanks!
"""

# First set up the figure, the axis, and the plot element we want to animate
```

```
fig = plt.figure()
ax = plt.axes(xlim=(0, L), ylim=(To*0.95, 1.05*Ti))
ax.grid()
plt.xlabel('Distance From Workpiece Surface (m)')
plt.ylabel('Temperature (Degress Celsius)')
line, = ax.plot([], [], lw=2)


# initialization function: plot the background of each frame
def init():
    line.set_data([], [])
    return line,


# animation function.  This is called sequentially
def animate(i):
    x=numpy.linspace(0,L,1000)
    time=times[i]
    tau=alpha*time/(L**2)
    zetastar=(2*phi*math.sqrt(tau))+(1-rns)
    xstar=(zetastar*L)
    def fun(x):
        if (x>0 and x<=xstar):
            thetas=thetastar*math.erf((x/L)/((2*math.sqrt(tau))+((1-rns)/phi)))/math.erf(phi)
            return ((Ti-To)*thetas)+To
        elif (x>xstar):
            thetal=1-(((1-thetastar)/math.erfc(phi))*math.erfc((x/L)/((2*math.sqrt(tau))+((1-
rns)/phi))))
            return ((Ti-To)*thetal)+To
    vfun=numpy.vectorize(fun)
    y=vfun(x)
```

```
    line.set_data(x,y)
    return line,

# call the animator.  blit=True means only re-draw the parts that have changed.
anim = animation.FuncAnimation(fig, animate, init_func=init,
                               frames=len(times), interval=1, blit=True)

# save the animation as an mp4.  This requires ffmpeg or mencoder to be
# installed.  The extra_args ensure that the x264 codec is used, so that
# the video can be embedded in html5.  You may need to adjust this for
# your system: for more information, see
# http://matplotlib.sourceforge.net/api/animation_api.html
#anim.save('basic_animation.mp4', fps=30, extra_args=['-vcodec', 'libx264'])

plt.show()
```

REFERENCES

Barnes, H. A. (1989). *An introduction to rheology* (J. F. (John F. Hutton & K. Walters, Eds.) [Book]. Elsevier : Distributors for the U.S. and Canada, Elsevier Science Pub. Co.

Barnes, H. A., Hutton, J. F. (John F., & Walters, K. (1989). *An introduction to rheology*. Elsevier.

Cho, H., Journal, Y. C.-W., & 1989, undefined. (n.d.). A study of the thermal behavior in resistance spot welds. *Files.Aws.Org*. Retrieved July 17, 2021, from http://files.aws.org/wj/supplement/WJ_1989_06_s236.pdf

Coussot, P., Malkin, A. Y., & Ovarlez, G. (2017). Introduction: yield stress—or 100 years of rheology. *Rheologica Acta*, *56*(3), 161–162. https://doi.org/10.1007/S00397-017-1003-6

Dantzig, J. A., & Rappaz, M. (2016). *Solidification: -Revised & Expanded*. https://books.google.com/books?hl=zh-CN&lr=&id=k1Q-DgAAQBAJ&oi=fnd&pg=PR5&dq=solidification+dantzig&ots=8C3a2iQus9&sig=z5bR6pbWabuhcgpqjHMXgiDKqjE

Dickinson, D., Franklin, J., & Stanya, A. (1980). Characterization of spot welding behavior by dynamic electrical parameter monitoring. *Welding Research Supplement*, *6*(June), 170–176. http://aws.org/w/a/wj/supplement/WJ_1980_06_s170.pdf

Dickinson, E. J. F., Ekström, H., & Fontes, E. (2014). COMSOL Multiphysics®: Finite element software for electrochemical analysis. A mini-review. *Electrochemistry Communications*, *40*, 71–74. https://doi.org/10.1016/J.ELECOM.2013.12.020

Dini, F., Ghaffari, S. A., Jafar, J., Hamidreza, R., & Marjan, S. (2020). A review of binder jet process parameters; powder, binder, printing and sintering condition. *Metal Powder Report*, *75*(2), 95–100. https://doi.org/10.1016/J.MPRP.2019.05.001

Feulvarch, E., Rogeon, P., Carré, P., Robin, V., Sibilia, G., & Bergheau, J. M. (2006). Resistance spot welding process: Experimental and numerical modeling of the weld growth mechanisms with consideration of contact conditions. *Numerical Heat Transfer; Part A: Applications*, *49*(4), 345–367. https://doi.org/10.1080/10407780500359760

Fischer, P. (2019). Understanding Viscoelasticity - An Introduction to Rheology (Nhan Phan-Thien). *Applied Rheology*, *23*(6), 329–329. https://doi.org/10.1515/ARH-2013-0029/HTML

Freels, J., Conference, P. J.-C., Newton, Mass, (2011). Multiphysics Simulations of the Complex 3D Geometry of the High Flux Isotope Reactor Fuel Elements Using COMSOL. *Comsol.Jp*. Retrieved July 11, 2021, from https://www.comsol.jp/paper/download/83929/freels_paper.pdf

Han, Z., Orozco, J., Indacochea, J., journal, C. C.-W., & 1989, undefined. (n.d.). Resistance spot welding: a heat transfer study. *App.Aws.Org*. Retrieved July 17, 2021, from https://app.aws.org/wj/supplement/WJ_1989_09_s363.pdf

Hildebrand, J. H., & Lamoreaux, R. H. (1976). Viscosity of liquid metals: An interpretation. *Proceedings of the National Academy of Sciences*, *73*(4), 988–989. https://doi.org/10.1073/pnas.73.4.988

Jansson, A., & Edholm, O. (2016). *Scale factor and shrinkage in additive manufacturing using binder jetting*. https://www.diva-portal.org/smash/get/diva2:950841/FULLTEXT01.pdf

Jeyakumar, M., Hamed, M., & Shankar, S. (2011). Rheology of liquid metals and alloys. *Journal of Non-Newtonian Fluid Mechanics*, *166*(14–15), 831–838. https://doi.org/10.1016/j.jnnfm.2011.04.014

Jr, W. F. J., JE Hetzner - US Patent 7 141, 207, & undefined 2006. (n.d.). Aluminum/magnesium 3D-Printing rapid prototyping. *Google Patents*. https://patents.google.com/patent/US7141207B2/en

Kim, E. W. (1988). Parametric Analysis of Resistance Spot Welding Lobe Curve. *SAE Transactions*, *97*, 107–118.

Kimchi, M., & Phillips, D. H. (2017). Resistance Spot Welding: Fundamentals and Applications for the Automotive Industry. *Synthesis Lectures on Mechanical Engineering*, *1*(2), i–115. https://doi.org/10.2200/s00792ed1v01y201707mec005

Mayboudi, L. S. (2019). *COMSOL Heat Transfer Models*. 402.

Miller Welds Handbook. (2012). *HANDBOOK FOR Resistance Spot Welding*. 1–9. www.MillerWelds.com

Modigell, M., Pape, L., phenomena, H. M.-S. state, & 2006, undefined. (2006). Rheology of semi-solid steel alloys at temperatures up to 1500 C. *Trans Tech Publ*. https://doi.org/10.4028/www.scientific.net/SSP.116-117.606

Mostafaei, A., Elliott, A. M., Barnes, J. E., Li, F., Tan, W., Cramer, C. L., Nandwana, P., & Chmielus, M. (2021). Binder jet 3D printing—Process parameters, materials, properties,

modeling, and challenges. *Progress in Materials Science*, *119*. https://doi.org/10.1016/J.PMATSCI.2020.100707

Mostafaei, A., Stevens, E. L., Hughes, E. T., Biery, S. D., Hilla, C., & Chmielus, M. (2016). Powder bed binder jet printed alloy 625: Densification, microstructure and mechanical properties. *Materials & Design*, *108*, 126–135. https://doi.org/10.1016/J.MATDES.2016.06.067

Reid, R., Prausnitz, J., & Poling, B. (1987). *The properties of gases and liquids*. https://www.osti.gov/biblio/6504847

Rishmawi, I., Salarian, M., & Vlasea, M. (2018). Tailoring green and sintered density of pure iron parts using binder jetting additive manufacturing. *Additive Manufacturing*, *24*, 508–520. https://doi.org/10.1016/J.ADDMA.2018.10.015

Sheydaeian, E. (2017). *Systems, materials, and methodologies for multi-material hybrid additive manufacturing functionally graded structures*. https://uwspace.uwaterloo.ca/handle/10012/12556

Spencer, D. B., Mehrabian, R., & Flemings, M. C. (1972). Rheological behavior of Sn-15 pct Pb in the crystallization range. *Metallurgical Transactions*, *3*(7), 1925–1932. https://doi.org/10.1007/BF02642580

Stainless Steel - Grade 17-4 (UNS S17400). (n.d.). Retrieved July 19, 2021, from https://www.azom.com/article.aspx?ArticleID=6778

Sun, C., Geng, H., Ji, L., Wang, Y., & Wang, G. (2007). Rheological properties of Pb, Sb, Bi, and Sn melts. *Journal of Applied Physics*, *102*(3). https://doi.org/10.1063/1.2764023

Sun, R., Yu, W., Zhang, H. H., Das, M., & Han, Q. (2019). *Mathematical Modeling of Resistance Spot Welding*. *6*(March), 9469–9476.

Tan, W., Zhou, Y., Kerr, H. W., Lawson, S., Dickinson, D., Franklin, J., Stanya, A., Flow, U. E., Flow, B. E., Hildebrand, J. H., Lamoreaux, R. H., Adusei, P., Anyimadu-antwi, K., & Halm, N. (1976). A study of dynamic resistance during small scale resistance spot welding of thin Ni sheets. *Welding Research Supplement*, *73*(14), 170–176. https://doi.org/10.1007/b94608

Toyserkani, E., Khajepour, A., & Corbin, S. (2004). *Laser cladding*. https://books.google.com/books?hl=zh-CN&lr=&id=zfvbyCHzVqMC&oi=fnd&pg=PA1&dq=%5B11%5D+E.+Toyserkani,+A.+K

hajepour,+S.F.+Corbin,+Laser+Cladding,+CRC+Press,+2004.&ots=vwqKGZXuQe&sig=ZSTauo3QDzz1wDqXglAAdyqSNFY

Vanderplas, J. (2013). Animation in Python — AMath 483/583, Spring 2013. In *University of Washington AMath 483/583*. https://faculty.washington.edu/rjl/classes/am583s2014/notes/animation.html

Wang, Y., & Zhao, Y. F. (2017). *ScienceDirect Investigation of Sintering Shrinkage in Binder Jetting Additive Manufacturing Process*. https://doi.org/10.1016/j.promfg.2017.07.077

Way, C., Shaw, T., Wadhwa, P., & Busch, R. (2007). Shear rate dependence of viscosity and configurational entropy of the Zr41.2Ti13.8Cu12.5Ni10.0 Be22.5 metallic glass forming liquid. *Journal of Alloys and Compounds*, *434–435*(SPEC. ISS.), 88–91. https://doi.org/10.1016/J.JALLCOM.2006.08.116

Wheat, E., Vlasea, M., Hinebaugh, J., & Metcalfe, C. (2018). Sinter structure analysis of titanium structures fabricated via binder jetting additive manufacturing. *Materials & Design*, *156*, 167–183. https://doi.org/10.1016/J.MATDES.2018.06.038

Xie, J., physics, A. K.-J. of A. (1997). Mathematical modeling of melting during laser materials processing. *Aip.Scitation.Org*, *81*(7), 3015. https://doi.org/10.1063/1.364336

Zhang, W. (2003). Design and Implementation of Software for Resistance Welding Process Simulations. *SAE Technical Papers*. https://doi.org/10.4271/2003-01-0978

Zhou, K., & Cai, L. (2013). Online nugget diameter control system for resistance spot welding. *International Journal of Advanced Manufacturing Technology*, *68*(9–12), 2571–2588. https://doi.org/10.1007/s00170-013-4886-0

Zhou, K., & Cai, L. (2014). On the development of nugget growth model for resistance spot welding. *Journal of Applied Physics*, *115*(16). https://doi.org/10.1063/1.4872247

PUBLICATIONS

SUN, R., HIGGINS, M., & ZHANG, H. H. (2021). Mathematical And Computational Modeling Of Resistance Spot Welding Solidification Process. The ASME 2021 International Design Engineering Technical Conferences & Computers and Information in Engineering Conference, IDETC/CIE 2020, Aug 2021

SUN, R., LIU, H., & ZHANG, H. H. (2020). COMSOL Implementation of Binder Jet Printing Densification Model in Automatic Valve System. comsol.jp.

SUN, R., Yu, W., Zhang, H. H., Das, M., & Han, Q. (2019). Mathematical Modeling of Resistance Spot Welding. Journal of Multidisciplinary Engineering Science and Technology (JMEST), 6(March), 2458–9403. Retrieved from www.jmest.org

SUN, R., SUN, Q., XIE, Y., DONG, P., CHEN, Q., & CHEN, K. (2016). Enhancing corrosion resistance of 7150 Al alloy using novel three-step aging process. Transactions of Nonferrous Metals Society of China (English Edition), 26(5), 1201–1210.

SUN, Q., SUN, R., CHEN, S., CHEN, Q., CHEN, K. (2015). Effect of atmospheric pollutants on electrochemical corrosion behavior of 7B50 aluminum alloy. The Chinese Journal of Nonferrous Metals, 25(3), 575-581.

SUN, Q., DONG, P., SUN, R., CHEN, Q., CHEN, K. (2015). Effect of ageing process on electrochemical corrosion property of extruded Al-6.2Zn-2.3Mg-2.3Cu aluminum alloy. The Chinese Journal of Nonferrous Metals, 25(4), 866-874.

YANG, B., SUN, Q., SUN, R., SHAO, S., LIU, Y., CHEN, K. (2015). Effect of inhibition properties of several amino acids on corrosion property of 7B50 aluminum alloy in 1mol/L NaCl+0.1mol/L HCl. The Chinese Journal of Nonferrous Metals, 25(11), 2990-2999.